STARS

Electronic Theses and Dissertations, 2004-2019

2014

Development of Full Surface Transient Thermochromic Liquid Crystal Technique for Internal Cooling Channels

Lucky Tran
University of Central Florida

Part of the Mechanical Engineering Commons

Find similar works at: https://stars.library.ucf.edu/etd

University of Central Florida Libraries http://library.ucf.edu

University of Central Florida

STARS
Showcase of Text, Archives, Research & Scholarship

DEVELOPMENT OF FULL SURFACE TRANSIENT THERMOCHROMIC LIQUID CRYSTAL TECHNIQUE FOR INTERNAL COOLING CHANNELS

by

LUCKY VO TRAN
B.S. University of Central Florida, 2012

A thesis submitted in partial fulfillment of the requirements
for the degree of Master of Science
in the Department of Mechanical and Aerospace Engineering
in the College of Engineering and Computer Science
at the University of Central Florida
Orlando, Florida

Summer Term
2014

Major Professor: Jayanta S. Kapat

ABSTRACT

Proper design of high performance industrial heat transfer equipment relies on accurate knowledge and prediction of the thermal boundary conditions. In order to enhance the overall gas turbine efficiency, advancements in cooling technology for gas turbines and related applications are continuously investigated to increase the turbine inlet temperature without compromising the durability of the materials used.

For detailed design, local distributions are needed in addition to bulk quantities. Detailed local distributions require advanced experimental techniques whereas they are readily available using numerical tools. Numerical predictions using a computational fluid dynamics approach with popular turbulence models are benchmarked against a semi-empirical correlation for the friction in a circular channel with repeated-rib roughness to demonstrate some shortcomings of the models used. Numerical predictions varied widely depending on the turbulence modelling approach used. The need for a compatible experimental dataset to accompany numerical simulations was discussed.

An exact, closed-form analytical solution to the enhanced lumped capacitance model is derived. The temperature evolution in a representative 2D turbulated surface is simulated using Fluent to validate the model and its exact solution. A case including an interface contact resistance was included as well as various rib sizes to test the validity of the model over a range of conditions. The analysis was extended to the inter-rib region to investigate the extent and magnitude of the influence of the metallic rib features on the apparent heat transfer coefficients

in the inter-rib region. It was found that the thermal contamination is limited only to the regions closest to the base of the rib feature.

An experimental setup was developed, capable of measuring the local heat transfer distributions on all four channel walls of a rectangular channel (with aspect ratios between 1 and 5) at Reynolds numbers up to 150,000. The setup utilizes a transient thermochromic liquid crystals technique using narrow band crystals and a four camera setup. The setup is used to test a square channel with ribs applied to one wall. Using the transient thermochromic liquid crystals technique and applying it underneath high conductivity, metallic surface features, it is possible to calculate the heat transfer coefficient using a lumped heat capacitance approach. The enhanced lumped capacitance model is used to account for heat conduction into the substrate material. Rohacell and aluminum ribs adhered to the surface were used to tandem to validate the hybrid technique against the standard technique. Local data was also used to investigate the effect of thermal contamination. Thermal contamination observed empirically was more optimistic than numerical predictions.

Traditional transient thermochromic liquid crystals technique utilizes the time-to-arrival of the peak intensity of the green color signal. The technique has been extended to utilize both the red and green color signals, increasing the throughput by recovering unused data while also allowing for a reduction in the experimental uncertainty of the calculated heat transfer coefficient. The over-determined system was solved using an un-weighted least squares approach. Uncertainty analysis of the multi-color technique demonstrated its superior performance over the single-color technique. The multi-color technique has the advantage of improved experimental uncertainty while being easy to implement.

To all of mankind who were raised on Earth

ACKNOWLEDGMENTS

My residency throughout this thesis was under the support of the Research and Mentoring Program, a graduate fellowship program at the University of Central Florida. It is a pleasure to acknowledge the assistance of Dr. Michael Aldarondo-Jeffries, the program director.

Finally, my acknowledgment is not complete without a mention of the love and support of my family members, especially my many younger siblings.

TABLE OF CONTENTS

LIST OF FIGURES

LIST OF TABLES

NOMENCLATURE

Roman Symbols

A_c	=	cross-sectional area
A_s	=	convective surface area
A_p	=	projected smooth wall area
A_{actual}	=	total convective surface area of ribbed wall
A_{sw}	=	projected smooth wall area of ribbed wall, equivalent area of un-ribbed wall
Bi	=	Biot number
c	=	solid specific heat
c_p	=	constant pressure specific heat
c_v	=	constant voume specific heat
C_f	=	skin friction coefficient
D	=	diameter
D_h	=	hydraulic diameter
e	=	roughness, rib height
e^+	=	roughness Reynolds number
f	=	Darcy friction factor
f_0	=	baseline friction factor
Fo	=	Fourier number
g^+	=	heat transfer roughness function
h	=	surface heat transfer coefficient
h	=	enthalpy
h_s	=	heat transfer coefficient based on convective area
h_p	=	heat transfer coefficient based on projected area
H	=	Channel height

L	=	periodic length
L_c	=	characteristic length
k	=	turbulent kinetic energy
k	=	thermal conductivity
k	=	ratio of specific heats
k_s	=	thermal conductivity of substrate
k_f	=	fluid thermal conductivity
$\dot{m}$	=	mass flow rate
M_w	=	molecular weight
Nu	=	Nusselt number
Nu_0	=	baseline Nusselt number
q"	=	wall normal heat flux
q_{in}	=	heat input
Q	=	total heat rate
Q	=	volumetric flow rate
P	=	Rib pitch
P	=	static pressure
P_{wet}	=	wetted perimeter
Pr	=	Prandtl number
r_p	=	pressure ratio
R	=	gas constant
R_u	=	universal gas constant
R+	=	friction roughness function
Re	=	Reynolds number
s	=	entropy
St	=	Stanton number

t	=	time variable
T	=	temperature
T_s	=	surface temperature
$\bar{T}_{base}$	=	average base temperature
$\bar{T}_{vol}$	=	volume average temperature
T_f	=	Film temperature
T_f	=	final temperature
T_L	=	temperature at low temperature reservoir
T_H	=	temperature at high temperature reservoir
T_1	=	compressor inlet temperature
T_2	=	compressor exit, combustor inlet temperature
T_3	=	turbine inlet temperature
T_4	=	turbine exit temperature
T_b	=	bulk temperature
T_i	=	initial temperature
T_g	=	TLC temperature at maximum green intensity
T_r	=	TLC temperature at maximum red intensity
T_w	=	wall temperature
T_∞	=	convective temperature
u	=	streamwise velocity component
u	=	fluid velocity
u^+	=	non-dimensional velocity
u_e^+	=	friction similarity parameter
u_τ	=	friction velocity
U	=	streamwise velocity
U_b	=	bulk velocity

V	=	normal velocity component
V	=	volume
w	=	rib width
w	=	spanwise velocity component
w_{net}	=	net work
W	=	Channel width
W_p	=	Pumping power
X	=	spatial variable
x	=	depth into solid substrate
X	=	streamwise coordinate
y^+	=	non-dimensional wall distance
Y	=	normal coordinate
Z	=	spanwise coordinate

Greek Symbols

α	=	thermal diffusivity
α	=	rib angle of attack, orientation angle
β	=	linear pressure coefficient
δ	=	Kronecker delta
Δ	=	difference
ϵ	=	turbulent dissipation rate
η_{th}	=	thermal efficiency
$\eta_{th,pp}$	=	thermal performance, pumping power consideration
η	=	group variable
θ	=	scaled, normalized temperature
κ	=	von Karman constant

μ	=	dynamic, absolute viscosity
μ_t	=	turbulent viscosity
ν	=	kinematic viscosity, momentum diffusivity
ρ	=	density
σ	=	periodic temperature gradient
τ	=	shear stress
τ	=	dummy integration variable
τ_w	=	wall shear stress

Subscripts

$_0$	=	baseline
$_{app}$	=	apparent quantity
$_b$	=	bulk
$_{cr}$	=	critical
$_{cu}$	=	copper
$_i$	=	initial
$_f$	=	film
$_f$	=	final
$_p$	=	pumping
$_p$	=	projected
$_s$	=	substrate
$_{sw}$	=	smooth wall
$_t$	=	apparent, turbulent
$_\tau$	=	friction
$_w$	=	wall

Superscripts

‾	=	Averaged
′	=	Fluctuating quantity
+	=	non-dimensional, inner coordinate
~	=	variational parameter
→	=	vector

Abbreviations

AR	=	Aspect ratio
CAD	=	Computed Aided Design
CAR	=	Channel aspect ratio (W/H)
CCD	=	Charge-coupled Device
CFD	=	Computational fluid dynamics
CLC	=	Classical Lumped Capacitance
CMOS	=	Complementary Metal-Oxide-Semiconductor
DNS	=	Direct Numerical Simulation
ELC	=	Enhanced Lumped Capacitance
FD	=	Fully Developed
FEM	=	Finite Element Method
FSR	=	Full Scale Range
FVM	=	Finite Volume Method
HD	=	High definition
HD	=	hard disk, hard drive
LED	=	Light-emitting diode
LES	=	Large Eddy Simulation
PC	=	Personal Computer

PKN	=	Prandtl-von Kármán-Nikuradse
PMMA	=	Poly(methyl methacrylate)
RAM	=	Random Access Memory
RANS	=	Reynolds-averaged Navier-Stokes
RAR	=	Rib aaspect ratio (w/e)
RSM	=	Reynolds Stress Modeling
SW	=	Smooth wall
TLC	=	thermochromic, thermochromatic liquid crystal
UHD	=	Ultra high definition

INTRODUCTION

In order to interact with the environment that we inhabit, various machines are typically employed to convert energy from one form to another and perhaps in the process also produce some usable amount of work. If the work produced is mechanical, the device is referred to as an engine such as those used in automobiles and airplanes. Depending on the particular need, the definition of useful work can be different for different machines. These machines, in obeying the operating principles dictated by the laws of physics, are limited in the manner in which they can operate.

The desire for a sustainable energy society has spawned a number of technological issues that are challenging today's engineers. These issues and developments include: the introduction of renewable energy sources; increasing efficiency in energy production, use, storage, and transportation; as well a reduction of emissions of greenhouse gases and the development of carbon capture and storage technologies.

Although the ideal efficiency and performance of any energy systems can be described by an overall thermodynamic analysis, there will always exist irreversible losses (production of entropy) in the system associated with the diffusion and transport various potentials such as temperature differences, species concentration, and possibly electrochemical potentials. To enhance, reduce, and suppress these irreversible losses can potentially lead to enormous benefits for the human society. In particular, the enhancement of the heat transfer in heat exchangers and components used in power production plants can have a tremendous impact on energy production, the environment, as well as the world economy.

The interfaces, where the previously mentioned transport processes occur, play a central role in determining the efficiency of the device, equipment, and plant used and will be crucial in shaping the future technology used in energy production, utilization, and storage. The turbulent convective heat transfer occurring at the interfaces is the focus of the current study, as it is applicable to a wider range of applications involving the transport of heat than laminar flows and also because of the inherent difficulty in controlling turbulence.

Turbomachinery

Turbomachineries in some shape or form are responsible for virtually all of commercial power and electricity production in the United States and as well as commercial and military air transport. Turbomachineries are essentially rotating devices (using blades and impellers) that either consume power, e.g. fans, compressors, and pumps, or extract power, e.g. a turbine by exchanging energy with a flowing fluid. Turbomachinery can be classified based on the primary flow path. When the flow direction of the working fluid is mostly parallel with the rotation axis, it is considered an axial flow device. When the flow direction is normal to the rotating axis (either inward or outward), it is a radial flow device. Mixed flow devices having portions of axial flow and portions of radial flow are also in use. The main turbomachines employed in electricity production are typically the steam or gas turbine engine, where fuel is burned to produce the mechanical work to run a generator, which in turns converts the mechanical work into electricity. For aircraft, gas turbine engines are used to produce thrust and auxiliary power. Because of the widespread use of turbomachineries, the slightest improvement in the operating efficiency of these devices can potentially have enormous benefits, such as a global reduction of the current greenhouse gas emissions and reduced energy prices.

The Gas Turbine Engine

Gas turbines are the workhorse for propulsion and power systems. Gas turbine engines can be grouped into three broad categories based on their application: 1) aircraft propulsion turbines, 2) electric power generation turbines, and 3) marine turbines and industrial turbines. The third category includes gas turbines that are usually derived from the first aircraft-based group but modified and adapted for land-use to suit their specific purpose. Marine turbines are typically aero-derivatives in a shipboard package and used to provide ship propulsion or generate electricity. The majority of modern Naval fleets are powered by gas turbine engines of the third category.

Figure 1 is a schematic of a simple, open Brayton cycle based turboshaft. A turboshaft is a form of a gas turbine engine that is designed to produce shaft power or mechanical work. Gas turbine engines used for running electrical generators are examples of turboshafts. Gas turbine engines that do not produce shaft work, may be used to generate jet thrust, such as turbojet engines. More complicated gas turbine configurations such as turbofans and turboprops are also common, where the gas turbine engine produces a combination of both jet thrust and shaft work to operate the fan or propeller.

The important stations of the gas turbine engine are the marked on the diagram.

1. Inlet to the compressor

2. Compressor exit and inlet to the combustor

3. Combustor exit and inlet to turbine

4. Turbine exhaust
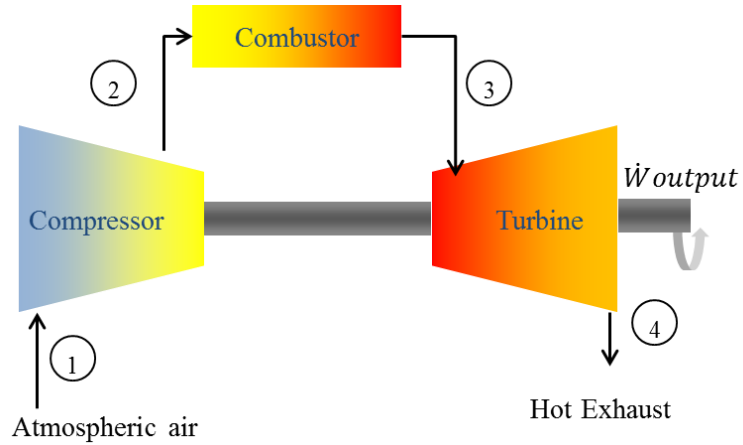
Figure 1: Brayton cycle schematic

The simple Brayton cycle efficiency can be expressed as Equation (1) in terms of enthalpies at each section.

$$\eta_{th,Brayton} = 1 - \frac{w_{net}}{q_{in}} = \frac{(h_3 - h_4) - (h_2 - h_1)}{(h_3 - h_2)} \qquad (1)$$

For an ideal gas, the enthalpies may be evaluated in terms of the specific heats at constant pressure (the enthalpies and specific heats of an ideal gas depend only on temperature). In general, the change in enthalpy of an ideal gas between initial and final states must be computed by the integral, Eq.(2).

$$\Delta h = h_f - h_i = \int_i^f c_p(T)dT \qquad (2)$$

If the specific heats vary linearly over a small temperature range, then the change in enthalpy can be calculated using an average specific heat, Eq.(3), where the specific heat is computed as the average specific heat between the initial and final states.

$$\Delta h = h_f - h_i = c_{p,avg}\left(T_f - T_i\right) \tag{3}$$

Using the average specific heat method, the simple Brayton cycle efficiency is then given

by Eq. (4).

$$\eta_{th,Brayton} = \frac{c_{p,turbine}(T_3 - T_4) - c_{p,compressor}(T_2 - T_1)}{c_{p,combustor}(T_3 - T_2)} \tag{4}$$

For a calorically perfect gas, a special idea gas where the specific heats are constants

(independent of temperature) the Brayton cycle efficiency can be further simplified to Eq. (5).

$$\eta_{th,Brayton} = 1 - \frac{(T_4 - T_1)}{(T_3 - T_2)} \tag{5}$$

Equation (5) is valid for a calorically perfect gas and may be used for a real cycle, not

necessarily an idealized Brayton cycle. If on the other hand, the processes from 1 to 2 and 3 to 4

are isentropic, the isentropic relations for these processes are governed by Eq. (6) from 1 to 2

and Eq. (7) from 3 to 4. These equations are the isentropic flow relations for a calorically

perfect gas. The ratio of specific heats, k, is defined in Eq. (8).

$$\frac{T_2}{T_1} = \left(\frac{P_2}{P_1}\right)^{k-1/k} \tag{6}$$

$$\frac{T_3}{T_4} = \left(\frac{P_3}{P_4}\right)^{k-1/k} \tag{7}$$

$$k = \frac{c_p}{c_v} \tag{8}$$

Equation (9) relates the ideal gas specific heats at constant pressure and volume to the gas constant and may be a useful relation for determining the ratio of specific heats if either the specific heat at constant pressure or constant volume are known. Note that the gas constant, R, depends on the substance and is related to the universal gas constant, R_u, by the molecular weight, M_w, of the substance.

$$c_p = c_v + R \qquad (9)$$

If pressures at 2 and 3 are equal ($P_2 = P_3$) as well as the pressures at 4 and 1 ($P_4 = P_1$), then the temperature ratios are equal, Eq. (10)

$$\frac{T_2}{T_1} = \frac{T_3}{T_4} \qquad (10)$$

The pressure ratio of the gas turbine engine is defined by Eq. (10). In general, unique pressure ratios may be computed separately for the compressor and turbine depending, including pressure ratios for individual stages.

$$r_p = \frac{P_2}{P_1} \qquad (11)$$

The Brayton cycle efficiency in terms of the pressure ratio is given by Eq. (12).

$$\eta_{th,Brayton} = 1 - \frac{T_1\left(\frac{T_4}{T_1} - 1\right)}{T_2\left(\frac{T_3}{T_2} - 1\right)} = 1 - \frac{1}{r_p^{(k-1)/k}} \qquad (12)$$

In an ideal, simple Brayton cycle, the working fluid is compressed in the compressor using an isentropic compression process, heat (fuel) is added, in the combustor or mixing chamber, in an isobaric (constant pressure) process, the mechanical work is extracted, by the turbine, in an isentropic expansion process, and the heat rejection process is also isobaric. If the working fluid is drawn into and exhausted out of the system as depicted in Figure 1, the cycle is an open cycle. If the working fluid is recycled, the system may be operating in a closed cycle. Because of inefficiencies in the compressor and turbine components, the compression and expansion (work extraction) processed are closer to adiabatic processes than isentropic In the case of active or passive cooling in the compressor and turbine components, these processes are neither isentropic nor adiabatic. Likewise, combustion inefficiencies results in significant pressure losses and the heat addition process is not truly an isobaric process. Mixing and frictional losses at the exhaust section and ducting of the turbine outlet also contribute to pressure losses. Nonetheless, the ideal Brayton cycle is a useful thermodynamic model of the actual device, which may never achieve the ideal Brayton cycle efficiency because of inefficiencies generated in the fluid dynamics and heat transfer processes involved.

Carnot Cycle

It is helpful to discuss the efficiency of the Carnot heat engine. The Carnot heat engine is a reversible engine and has the highest efficiency that is attainable by any heat engine. The Carnot cycle is characterized by: a reversible adiabatic compression, where the working fluid is compressed; a reversible isothermal expansion, where heat is exchanged with the hot reservoir; a reversible adiabatic expansion, where the working fluid performs work; and a reversible isothermal compression, where heat is rejected to the cold reservoir. The efficiency of a Carnot heat engine is given by Eq. (13).

$$\eta_{th,Carnot} = 1 - \frac{T_L}{T_H} = 1 - \frac{T_1}{T_3} \qquad (13)$$

Increasing Cycle Efficiency

It is desirable to push the cycle efficiency of the gas turbine as high as possible. By examination of Eq. (5) and Eq. (13), one method to increase the cycle efficiency is to increase the gas temperature at the turbine inlet (T_3). An alternative method is to increase the efficiencies of the components involved in the cycle, i.e. increasing the compressor, turbine, and combustion efficiency. Early turbines suffered from low cycle efficiencies cause by low operating temperatures and inefficiencies in the compressors and turbines. The turbine inlet temperature has steadily rose over the years, simultaneously compressors and turbines have designed and built with increased inefficiencies. Yet another approach to increase the efficiency of gas turbine engine is to modify the basic cycle by incorporating intercooling, intra-cooling, recuperation, regeneration, or reheating. Modifications to the basic cycle in industrial installations involves tremendous capital costs for the extra equipment (due to the large size of heat exchangers

needed). For gas turbine engines that are already highly efficiency (such as the large utility scale gas turbines used in electricity generation), the increased capital cost of adding these modifications may not outweigh the benefit obtained by the greater efficiencies. These turbines will have much longer payback periods in order to reach the break-even point. However, for an inefficient turbine, modifications to the basic cycle may be a cost effective. The improvement in efficiency and fuel savings is competitive with the cost of the modifications. Small utility turbines, or microturbines, are often associated with low simple cycle efficiencies. Microturbines are constructed or inferior metals to save cost and hence must operate at much lower maximum temperatures, lowering their thermal efficiency. In order to improve their performance, microturbines often modified with compact, high effectiveness recuperators.

The increase in turbine inlet temperature is limited in practice by the capability of the metal alloys used to make the turbine components (combustion liners, vanes, and blades). The component operating temperature must be maintained well below the material melting temperature. Gas temperatures throughout the turbine are also restricted in order to reduce NO_x emissions to comply with local regulatory standards.

Increasing the turbine inlet temperature also requires an increases of pressure ratio, recall Eq. (12). A higher pressure ratio requires the compressor to do more work. At high pressure ratios, the temperature of the gas may also exceed the material limit. Compressor blades are often manufactured from lower cost stainless steels and have much lower material limits compared to turbine blades, which are manufactured using nickel-based superalloys and coated with thermal barrier coatings. However, if the pressure ratio is expected to increase further then the compressor would need to be fabricated from more exotic materials or cooling must be

9

implemented in the compressor. Increasing the pressure ratio of a given compressor is also an aeromechanical design challenge. A higher pressure ratio can be obtained by adding an additional stage to the compressor, which significantly increases the cost of the turbine. To achieve a higher pressure ratio without adding an additional stage means that the pressure ratio across existing stages is increased; the compressor blades must also be designed to handle the increased mechanical loading. Compressors operating at high pressure ratios are also susceptible to stall and surge, a disruption of the local flow inside the compressor, and have smaller stability margins for stable operation at higher pressure ratios.

Figure 2 describes the historical advances in the increase in turbine inlet temperatures made possible by the introduction of various cooling technologies. The turbine inlet temperature employed in modern gas turbine engines is well above the allowable material temperature. The higher than allowable gas temperature is only possible by using advanced cooling schemes to cool the parts and maintain their temperature below the allowable temperature. Advancements in materials have led to an increase in the allowable metal temperature, allowing for an increase in the turbine entry temperature. However, advances in cooling technology were responsible for the most significant increases in the turbine entry temperature. The introduction of thermal barrier coatings, a ceramic coating placed over hot surfaces, also contributed to a significant increase the turbine inlet temperature.
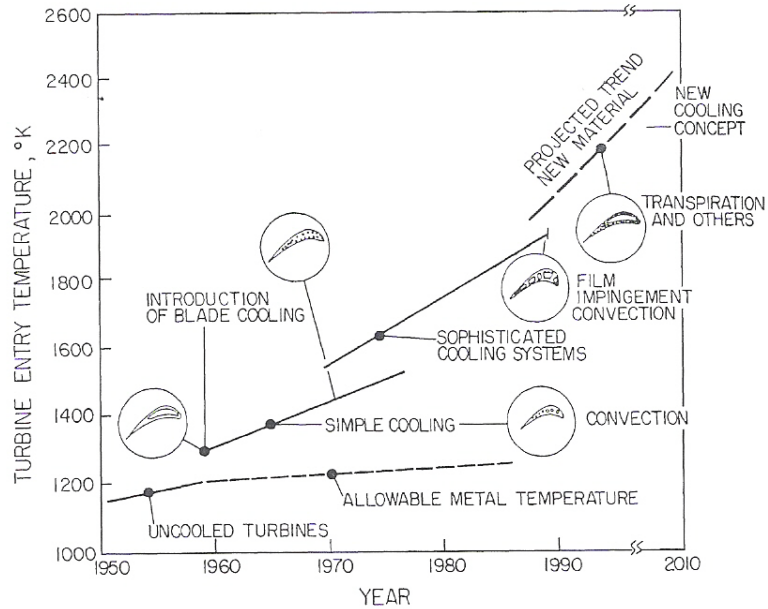
Figure 2: Advances in turbine entry temperature from new cooling schemes[1]

Because the turbine inlet temperature is directly related to the overall cycle efficiency of the gas turbine engine, the actual turbine inlet temperature attainable in an operating engine is a considered a technological standard for the engine. Engines operating at a higher turbine inlet temperature are considered to be more advanced. The turbine inlet temperature in the near future is expected to be as high as 1700 °C for power generation turbines and 1900 °C for advanced military engines [2].

One of the parts in the gas turbine engine that needs considerable attention is the gas turbine blade. Figure 3 depicts a turbine blade for aero-type engines; the three major cooling regimes are all labeled on the figure. Serpentine channels, often lined with rib and also pin-fin turbulators, are run through the interior of the turbine blade. Coolant bled from the compressor stage passes through the internal passages of the turbine and cools the inner surface.

11

Impingement cooling is also sometimes employed, near the leading edge to remove a large

amount of heat closer to its source. The coolant is then bled from the internal passages through

discrete holes on the blade surface. The coolant exiting the blade through these film cooling

holes forms a protective blanket over the surface and effectively shields the blade surface from

the high temperature gas.
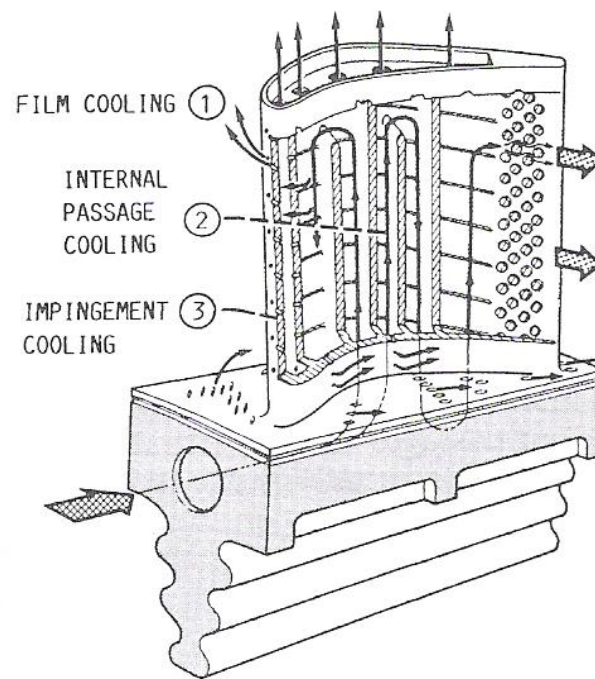
Figure 3: Typical cooled aircraft turbine blade [3]

Combustion

The efficiency of the gas turbine engine is not limited only by metallurgical constraints and limitations in effective cooling schemes. Heat addition to the working fluid in a gas turbine engine traditionally involves the burning of a fossil fuel (such as natural gas) and the highest temperatures in the gas turbine engine occur at the end of the combustion process. Even if the inefficiencies of the compressor and turbine components could somehow be eliminated and extraordinary techniques to infinitely cool the components implemented, the chemistry of the fuel actually places an upper limit on the highest attainable temperature anywhere in the cycle. The equivalence ratio is the ratio of the actual fuel-oxidizer ratio to the stoichiometric ratio. At the stoichiometric limit, the equivalence ratio is unity. The adiabatic flame temperature is a property of the thermochemistry of a given combustion process (constant volume or constant pressure) and combustion reactants (fuel-oxidizer combination and equivalence ratio). The adiabatic flame temperature is a maximum at the stoichiometric limit, when the fuel-oxidizer ratio is such that all proportions are consumed.

Current state of the art machines have turbine inlet temperatures approaching the stoichiometric limit of the fuels used. Once the stoichiometric limit is attained, further increases in efficiency can only be obtained by switching chemistry and using fuels with higher adiabatic flame temperatures. Unfortunately, few fuels can make economically viable choices for further improvements.

Generators

Although the components of the generators employed in electricity production are not exposed to the high temperature environment found in gas turbine engines, the cooling of the generator rotor and stators in land-based power generation equipment is no less a daunting task. Despite the high efficiency of modern generators, which can exceed 98%, an enormous amount of heat must be removed from the generator. One of the mechanisms through which the heat is generated is through Joule heating because of resistance of the conductors used in the generator windings. The maximum generator size is also limited by the total amount of cooling available.

The three main components that need cooling are the stator core, stator winding, and rotor winding. The windings in the generator must be maintained below a certain temperature at all times in order to not burn the insulation and cause a short in the generator circuit. When air cooling is insufficient, hydrogen gas is used as the cooling fluid because of the lower viscosity and better thermal transport properties of hydrogen compared to air. A cross section of three hydrogen-cooled turbogenerator rotor concepts is given in Figure 4. All three cooling concepts require a fairly complicated manufacturing process; it is also necessary to build the generators as pressure vessels in order to contain the hydrogen gas. External systems to supply and control the hydrogen are also needed.
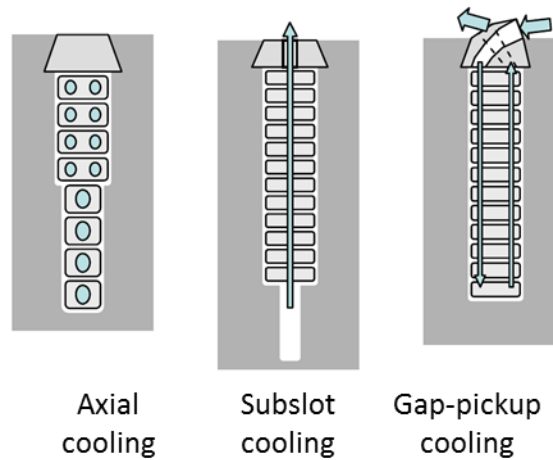
Figure 4: Cross section of hydrogen-cooled turbogenerator rotor slots [4]

For the most demanding cooling requirements, water cooling may be used. Water has a much greater heat capacity and density than air or hydrogen and can remove greater amounts of heat for the same flow rate. Water cooling allows for the generator to be lighter, compact, and potentially more cost effective because of the better cooling. The greater heat removal rate allows for a greater power density (greater power output for an equivalently sized generator, or an equivalent power in a smaller sized generator). The drawback towater cooling is the complication of circulating water through the windings and other parts of the generator. The aerodynamic losses of water in the rotor have considerable pumping requirements. Water cooling is often employed only when necessary, for very large machines, and is used typically only for the non-rotating stator components with hydrogen cooling used in the rotating parts.

Generators employing both water-cooled stators and rotors are scarce, the Swedish manufacturing company Asea produces and operates a number of units of this class [4]. A major road block to the use of water-cooled rotors in the next generation of power generation equipment by the leading manufacturers is the cost needed to develop the new technology and obtain an operating record to demonstrate its reliability and robustness. Asea, in the early 1960s decided to avoid hydrogen cooling and chose to develop completely water-cooled machines, skipping the development of hydrogen cooling.

Because of the already high efficiency of the state-of-the-art generators, a further increase in efficiency is not only difficult and costly to develop but also would not lead to as much benefit as an increase in efficiency in other components in the power plant. Hence, the research and development of more optimum cooling channel designs for use in generator rotor and stator cooling has not received as much attention as in gas turbine cooling. However, the operation of electrical generators and the generator cooling challenges are just as vital to the overall plant performance; these challenges will continue to persist for as long as a device is necessary to turn mechanical work into electricity.

More Heat, Less Friction

Improvements in cooling technology can have direct benefits for both the gas turbine engine and the generator. In principle, introducing a new cooling scheme that transfers more heat with less pumping power required tends to increase the overall efficiency of the device.

In general, the heat transfer enhancement of fluid flow in pipes involves complicated geometrical configurations. However, the analogy can always be made by considering the canonical configuration, the fluid flow and heat transfer in a constant area smooth pipe. The

essential aspects of heat transfer are all present in this configuration. A certain pumping power is necessary to drive the fluid flow in the pipe in order to oppose the friction in the pipe, Eq. (14), which is manifested as a shear stress to the fluid near the walls of the pipe.

$$W_p = \Delta P \cdot Q \qquad (14)$$

For fully developed flow, the pumping power is exactly the product of the channel pressure drop and the volumetric flow rate of the fluid. Hence, in fully developed flows, the pumping power is converted entirely, directly, and irreversibly into heat through viscous dissipation. This thermodynamic process therefore has an unavoidable entropy generation associated with it and can be written as:

$$\Delta s = \Delta s_f + \Delta s_h = \frac{W_p}{T_f} + q'' \left(\frac{1}{T_f} - \frac{1}{T_w} \right) = \frac{\tau_w U_b}{T_f} + \frac{h(T_w - T_f)^2}{T_f T_w} \qquad (15)$$

where U is the bulk mean velocity, h is the heat transfer coefficient based on the temperature difference between the wall and the fluid, $\Delta T = T_w - T_f$. A detailed discussion of the use of Equation (15) and its consequences can be found in works by Adrian Bejan [5] or his textbook on Advanced Engineering Thermodynamics[6]. For fully developed flows, the pumping power is the product of the channel pressure drop and the volumetric flow rate of the fluid. Equation (15) suggests that the ultimate heat transfer technology is to achieve either complete thermal insulation or infinite heat transfer rate, while minimizing losses caused by friction. The frictional losses also need to be reduced to minimize the work required to drive the flow, since the pumping power is always irreversibly dissipated into heat.

Momentum transport and heat transport are proportional in most engineering flows, a behavior well-known to fluids engineers as the Reynolds analogy. Increasing heat transfer in a fluid flow process is usually accompanied by additional momentum transport. The Reynolds analogy claims that the process of heat transport away from the wall is analogous to the momentum transport process, corresponding to the effect of wall friction and shear stress in slowing the fluid which must be overcome by the work used to drive the fluid flow. The Reynolds analogy implies that the occurrence of more heat transfer also implies more friction. Although the Reynolds analogy is strictly applicable to pipes and flow over flat plats, its implications are nonetheless applicable to other flows, at least qualitatively. It is important to note that more complicated analogies of heat, mass, and momentum have been derived for other flow configurations, such as the Chilton-Colbourn analogy.

The fundamental question remains as to whether the heat transfer can be further enhanced while reducing the pumping power. The Reynolds analogy claims that the heat, mass, and momentum transport processes are mathematically the same and seems to suggest that more friction is expected if more heat transfer is to occur whereas Eq. (15) demands that a search be made for a channel that can promote more heat transfer but without added friction in order to minimize the irreversible losses. The answer is non-trivial but is of profound influence to further advancements in cooling technology. The difference in how the local turbulent transport of momentum and that of heat contribute to the friction and heat transfer coefficients is a key to the answer of whether the dissimilar control is possible.

Recent progress in analyzing turbulence mechanics and designing turbulence control offers a chance to develop a scheme for dissimilar momentum and heat transport, how to obtain

18

more heat transfer with less friction. A detailed discussion of recent progress in methods of turbulent flow control is given by Kasagi et al. [7] discussed the mathematical formulations of the contribution of turbulent transport to wall friction and heat transfer. By reexamining the governing equations and boundary conditions for convective heat transfer, the possibility of achieving dissimilar control in turbulent flow is revived. The Reynolds analogy and such equivalent analogies fail to acknowledge an inherent difference in the fact that velocity is divergence free whereas temperature is a conservative scalar. By exploiting the inherent difference, the dissimilar control can be achieved even in flows where the averaged momentum and heat transport equations have the same form [7].

<div align="center">Internal Cooling</div>

Optimization of internal cooling channels has been the subject of a great deal of study in past years for thermal management of hot-gas-path-components in turbomachines. To improve the efficiency of these cooling channels, one must optimize the various aspects of the channel to remove the maximum amount of heat for a given amount of coolant. A variety of techniques are employed to accomplish this task. The most common method is to apply some form of transport enhancing geometry to the walls of the channel which acts to increase secondary flows and turbulence within the channel resulting in improved mixing and more effective heat transfer. These geometries break up the viscous sub-layer and, in some cases, promote the formation of vortices and improve the advection of heat from the hot surfaces. The penalty for the addition of these geometries is usually an increase in pressure drop over the length of the channel. Different components are designed with different cooling schemes based on the specific design requirements. For example, dimples are typically applied in areas where a low pressure drop is

desired to allow more favorable pressure margins for other regions of the cooling design because of their notably low pressure drop characteristics. Therefore it is important to find a configuration that provides the best balance between heat transfer and friction augmentation for the specific channel configuration. For this reason, wall surface geometries found in literature are vast and diverse in nature; including dimples, pin fins, ribs, and numerous derivatives of these designs.

These surface enhancements improve the heat transfer capabilities of the cooling channels by two mechanisms. The first is through an increase in the available surface area through which the heat transfer takes place; under similar flow conditions, an increase in the available area for heat exchange is directly proportional to the heat. The other mechanism is by changing the flow field in such a way as to improve the mixing of the fluid in the channel and convection of heat away from the channel walls. Large surface features can potentially influence the bulk flow in the channel and promote better mixing in the bulk flow, and mix the relatively colder fluid near the center of the channel with the relatively hot fluid closer to the channel walls. Smaller surface features, that might not influence the bulk flow, can trip the boundary layer, disrupting the viscous sub-layer near the channel walls, which is occupied by slow moving fluid, and to bring the colder fluid from the mainstream directly into contact with the hot walls of the cooling channel. A number of cooling channel geometries has been investigated by utilizing one or more of these phenomena.

Ribs are positive features that act to trip the flow, disrupting the viscous sub-layer formation and causing the formation of complex vortices. Ribs cause separation and reattachment as well as induce secondary flows depending on their size, configuration, and

alignment. The increased turbulence leads to a greater mixing of the flow and improvement in the advection of heat away from the channel walls. Typically, rib turbulators are rectangular in cross-section. Many other parameters such as rib aspect ratio, channel blockage ratio, rib orientation to the flow direction, and rib spacing (pitch) can be varied such that an optimal design is achieved. A great deal of studies has been devoted to the application of these features to internal cooling channel designs, for gas turbine vanes and blades.

Rib-Shaped Turbulators

One of the earliest studies of the application of rib turbulators to channel walls was performed on single-pass, stationary channels. Han et al. studied the effects of rib orientation, rib shape, and rib pitch-to-rib-height ratio (P/e) on the overall heat transfer performance of the channel [8]. This study concluded that, for the same pumping power, ribs with a 45° orientation with respect to the flow yield better results than those oriented orthogonal to the flow direction. Han et al. investigated the effects of channel aspect ratio on the heat transfer characteristics of the channel with angled ribs [9]. It was concluded that the cooling channels perform best with a channel aspect ratio of 1 and a rib-orientation angle (α) in the range of 30-45°. It was also found that the same range of angles is also optimal for rectangular channels; and square channels surpassed rectangular channels in overall performance.

Han et al. provided Nusselt number augmentation and friction factor augmentation data for wedge-shaped and delta-shaped transport promoters in a square channel [10]. The authors compared the performance of broken-wedge and delta configurations to the full-length configurations. It was found that the broken arrangements perform better than the full-length case. Chandra et al. studied the heat transfer and friction in a rectangular channel with transverse

ribs on one, two, and four walls and was the first study performed on the application of ribs to four channel walls [11]. Taslim et al. studied twelve different rib geometries, with square as well as trapezoidal cross-section, applied to all four walls of a channel [12]. This work characterized the heat transfer and flow characteristics of each geometry. Casarsa et al. characterized the hydrodynamic and heat transfer performance of square ribs oriented perpendicular to the flow in a rectangular cooling channel [13]. The ribs studied were comparatively very large, creating a 30% blockage ratio. Reported results included time-averaged distributions of mean velocity components, and Nusselt number values.

Mahmood et al. presented spatially resolved Nusselt numbers and friction factors for a channel with an aspect ratio of four and 45° angled ribs[14]. The ribs were arranged such that they were oriented perpendicular to each other on opposite walls. The rib-height to hydraulic diameter was 0.078, rib pitch-to-height was 10, and blockage ratio is 25%. This work concluded that the highest spatially resolved Nusselt numbers are present on the top surface of the rib with the lowest values being found on the flat surfaces in between the ribs where flow separation and shear layer reattachment have a pronounced effect. Ribs oriented at 45° were also studied by Wang et al.[15]. Cho et al. investigated a combination of continuous and discrete, parallel and cross arrays of ribs in a single pass square channel [16].

Because the driving force behind these advancements has been the gas turbine industry, these studies have been primarily limited to channel aspect ratios of one to four, which represent those found in the gas turbine engine. Although high aspect ratio channels (CAR > 8) and high aspect ratio ribs (RAR > 1) do exist in industrial applications, the literature on their performance is found to be quite limited.

Some previous works in high aspect ratio cooling channels include Bunker et al., Zhang et al., and Sparrow and Cur. In these studies, the channel aspect ratios are kept at 14:1, 10:1, and 18:1, respectively. Bunker et al. tested a channel that combined the trailing edge and the adjacent rib channel of an aero engine airfoil [17]. Zhang et al. utilized ribbed and grooved walls on the same surface in search for the optimum thermal performance [18]. Sparrow and Cur used mass transfer to study smooth rectangular channels and the effect of symmetric heating versus asymmetric heating [19]. They reported that heat transfer augmentation between the difference boundary conditions deviated less than seven percent in the fully developed portion of the channel.

Liu et al. applied 45° rib turbulators to two sides of a two-pass channel in a rotating rig. The rib pitch was varied to obtain rib pitch-to-height (P/e) ratios of 10, 7.5, 5, and 3 [20]. The rib cross section was square. The rib with the closest rib spacing of P/e = 3 had the best performance in both rotating and nonrotating channels. The rib layouts studied by Liu et al. are shown in Figure 5.
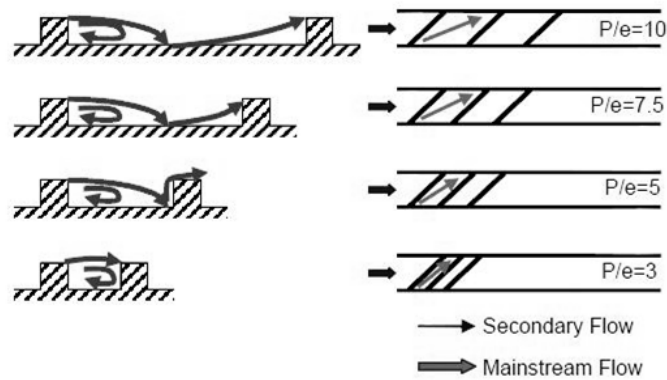
Figure 5: Rib spacing effect studied by [20]

Because of the secondary flows induced by the skewed ribs, as the number of ribs increased the strength of the secondary flows also increased and resulted in a continued increased in the heat transfer enhancement. This increase in heat transfer is not expected to occur for channels with orthogonal ribs, where the flow is trapped between the ribs and is not forced to circulate by the secondary flows. In their argument of the increased heat transfer with decreasing rib pitch, Liu et al. used the heat transfer enhancement of their ribbed channel based on the projected smooth channel area. However, by increasing the number of ribs in the channel and decreasing rib spacing, the total surface area of the channel was also increased. When taking into account the additional surface area with the addition of ribs, the heat transfer enhancement was eliminated. Friction results also indicated that the channel friction increased with decreasing rib pitch until 5. Less than 5, the friction factor decreased.

A number of studies have considered the effect of rib spacing but predominately for square ribs. Few studies have varied the rib width systematically. Wright & Gohardani studied the thermal performance (heat transfer and friction) of rib turbulators in a 3:1 aspect ratio rectangular channel at a Reynolds number range of 10,000–70,000 .[21]. The ribs studied were oriented 45° to the mainstream flow. Ribs were placed only on the two wide walls. Wright & Gohardani considered rib aspect ratios of 1, 2, 3, and 4 as well as the distance between ribs in order to investigate the combined effect of rib width and rib spacing on the thermal performance of the channel. The rib aspect ratio was varied by changing the rib width (w) while keeping the rib height (e) constant. The rib configurations studied by Wright & Gohardani are shown in Figure 6. Results from the study by Wright & Gohardani indicate that heat transfer enhancement decreases as the rib width increases and decreases when the rib spacing increases; increasing the

rib width is effective in increasing the thermal performance of the passage only when the rib width and spacing are varied in conjunction with one another.
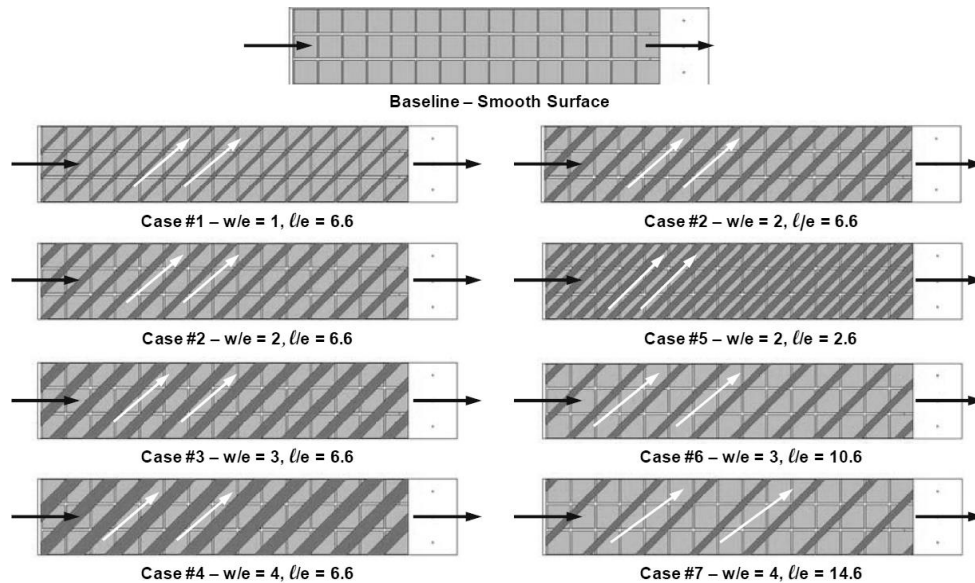
Figure 6: Angled rib configurations studied by [21]

The previous studies mentioned made use of altering the spacing between two consecutive ribs. In some cooling applications, such as in generator rotor cooling, the spacing between any two consecutive features is fixed. To reduce the cost of manufacturing the cooling channels in the rotors, each of the straps that form the generator rotor typically has identical features applied. The drawback of the reduced manufacturing cost and complexity is that the relative locations of each feature are also the same for each strap. Hence, the varying rib pitch or spacing between ribs is sometimes not permitted for rotor cooling applications. Other means of varying the rib shape and parameters must be used that does not require varying the parameters that are fixed by the rotor configuration. An optimum cooling channel design is not achieved

from just considering the thermal performance characteristics, although the aerothermal performance is an integral part of the process. In practice, manufacturing capabilities and cost considerations also play an important role. The effects of spatially non-uniform cooling are also important in considering the thermal stresses induced by the non-uniform cooling which can lead to component failure. A specific cooling arrangement with a higher rate of heat transfer and a greater degree of non-uniformity in the cooling can actually lead to component failure, the local part temperature may exceed the allowable material temperature in regions of low heat transfer. These types of cooling configurations are either eliminated in designs in favor of more uniform cooling concepts or the parts must be operated more conservatively to not risk damaging the part. Operation at suboptimal conditions causes the a detriment to the cooling performance, losing some of the benefit obtained by greater cooling capacity.

More complex rib configurations have also been studied. Kuntsmann et al. studied the performance of W-shaped, 2W-shaped and 4W-shaped ribs in a rectangular channel for channel aspect ratios of 2:1, 4:1 and 8:1 [22] for a combustor liner cooling application. The Reynolds numbers were considerably high (Re > 90000). Heat transfer measurements were conducted with the transient TLC technique. The results from this study found that with increasing order of the W-shape (W, 2W, 4W) the number of pairs of counter rotating vortices also increased. The W-shaped ribs produce two counter rotating vortices in each channel half. The 2W-shaped ribs produced four counter rotating vortices and 4W-shaped ribs produced eight counter rotating vortices.

The optimization of a cooling channel design to progress towards an ideal cooling requires much more than just the thermo-aero-mechanical considerations; in practice it is a multidisciplinary study where economic considerations also come into play (and even aesthetics). A building block approach to turbine aerothermal research is shown in Figure 7. Both experimental and analytical (or numerical) techniques are often used in conjunction with one another in order to reduce the total time of development.
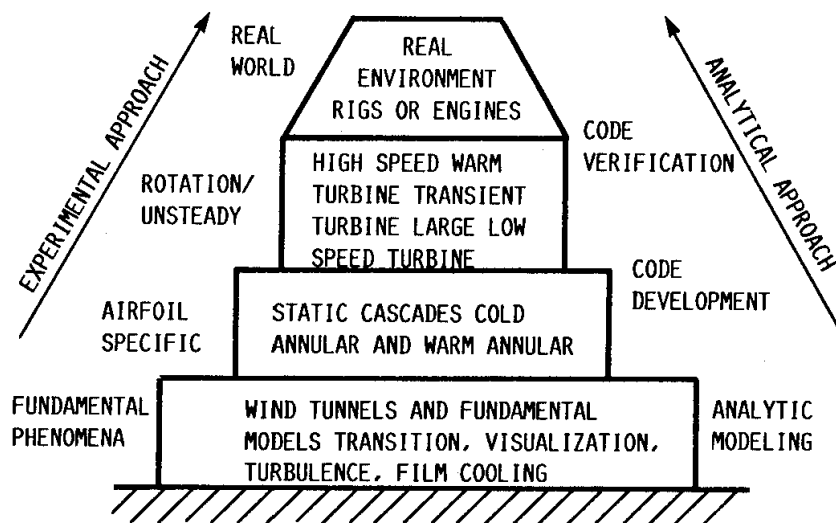
Figure 7: Building block approach to turbine aerothermal research [3]

At the lowest level of development, the fundamental and basic phenomena occurring are the primary interest. Testing is performed on very basic configurations or specific sections of interest in a simplified and well controlled environment. The experiments are designed to assess certain phenomena, and analytical and numerical approaches are designed in order to accurately model or reproduce the same phenomena. For experimental testing of cooling channel

performance, the performance tests are done on channels that may not be entirely representative of the actual implementation in the final product. Straight rectangular channels may be used to mimic the actual channels in the gas turbine blade. These channels may be tested on stationary experimental setups without any rotation, scaled-up in dimensions in order to improve the experimental accuracy of the results, use different materials (such as copper) for the cooling channel walls to reduce experimental uncertainties. Similarly, the analytical approach will attempt to model the most fundamental features. At progressively higher levels of development, the testing is performed in more realistic environments to take into account more effects that might be expected or experienced by the part in operation until the actual engine environment or actual engine performance is tested at the highest level.

The building block approach is not strictly linear. Development of a component can start at any level and is not restricted to progress strictly upward to higher levels. Past experience can allow for many of the lowest levels to be skipped if only minor changes are made. Drastic changes to the engine design however, may require a complete ground-up development process. Newer issues encountered at higher levels of development or that was not expected beforehand might call for a recess to a lower level of development to retest or improve the understanding of the basic phenomena. In the worst scenario, an unexpected failure caused by damage of an operating engine will launch investigations into the cause of the accident.

Key Data Reduction Parameters

Relevant parameters commonly encountered in internal cooling are presented in this section. The section starts with basic parameters from geometry and introduces useful engineering, non-dimensional parameters. Fundamental parameters are also introduced at the end of this subsection. Figure 8 is a sketch of a channel with square cross section.
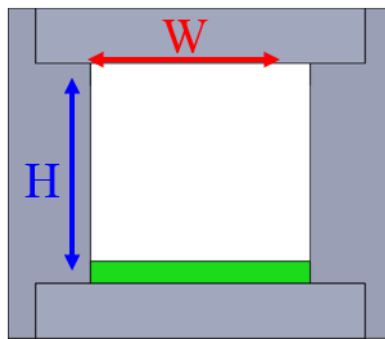
Figure 8: Sketch of channel cross section

The channel aspect ratio, Eq. (16), is usually defined as the channel width to channel height ratio.

$$\text{AR} = \frac{W}{H} \tag{16}$$

The wetted perimeter is given by Eq. (17) and flow cross sectional area by (18)

$$\text{P}_{wet} = 2W + 2H = 2H(1 + AR) \tag{17}$$

$$\text{A}_c = HW = H^2 AR \tag{18}$$

The hydraulic diameter, Eq. (19), is often used for channels of non-circular cross section.

$$D_h = \frac{4A_c}{P_{wet}} = \frac{4H^2 AR}{2H(1 + AR)} \quad (19)$$

The relative pitch, Eq. (20), describes the relative spacing of the surface features along with the relative roughness, Eq. (21), which describes the protrusion height.

$$\text{relative pitch} = \frac{P}{e} \quad (20)$$

$$\text{relative roughness} = \frac{e}{D_h} = \frac{e}{H} \frac{1 + AR}{2AR} \quad (21)$$

For internal flows the bulk velocity can be conveniently calculated from the mass flowrate, Eq. (22). The channel Reynolds number for internal flows may also be computed in terms of the channel flow rate, Eq. (23).

$$U_b = \frac{\dot{m}}{\rho A_c} \quad (22)$$

$$Re = \frac{\rho U_b D_h}{\mu} = \frac{4\dot{m}}{\mu P_{wet}} \quad (23)$$

The Darcy friction factor is defined as, Eq. (24).

$$f = \frac{\frac{\partial P}{\partial x} D_h}{\frac{1}{2} \rho U_b^2} \qquad (24)$$

The Nusselt number, Eq. (25), is a non-dimensional heat transfer and sometimes interpreted as the rate of heat convection in the fluid to the rate of heat conduction. The Stanton number for internal flows is given by Eq. (26)

$$Nu = \frac{h D_h}{k_{fluid}} \qquad (25)$$

$$St = \frac{h A_c}{\dot{m} c_p} \qquad (26)$$

Performance Metric

The friction augmentation, Eq. (27), is the friction factor for the channel with enhancement features normalized by its smooth counterpart (no enhancement) under identical operating conditions (same Reynolds number). The heat transfer augmentation, Eq. (28), is the of the heat transfer obtained with the surface enhancements normalized by the original smooth channel. A higher heat transfer augmentation is usually desirable, since more heat can be removed for the same flowrate, whereas a lower friction augmentation is preferred, least pumping requirements. For smooth channels, the friction factor tends to decrease with increasing Reynolds number whereas the Nusselt number generally increases with increasing Reynolds

31

number. For rib turbulated channels, the friction factor is usually a constant with Reynolds number, after a high enough Reynolds number is achieved. Hence, the friction augmentation for turbulated channels tends to increase with increasing Reynolds number whereas the heat transfer augmentation tends to decrease with increasing number. At high Reynolds numbers such as those encountered in industrial gas turbine blade cooling circuits, the Reynolds number can be quite large (on the order of 1 million). At these high Reynolds numbers, the heat transfer augmentation can be less than unity whereas the friction augmentation is much greater than unity (by more than 10x). The baseline friction and Nusselt number correlations may be taken from experiment measurements or estimated by using a friction and Nusselt number correlation for smooth channels.

$$friction\ augmentation = \frac{f}{f_0} \tag{27}$$

$$heat\ transfer\ augmentation = \frac{h}{h_0} \approx \frac{Nu}{Nu_0} \tag{28}$$

The thermal performance, Eq. (29), is defined as the ratio of the heat transfer enhancement to the ratio to the pumping power ratio. The thermal performance highlights the relative benefit of the increased heat transfer performance by applying surface enhancements to the increase in pumping requirement, or work consumed to supply the coolant flow.

$$\eta_{th,pp} = \frac{\dfrac{Nu}{Nu_0}}{\sqrt[3]{\dfrac{f}{f_0}}} \tag{29}$$

For very high Reynolds numbers, the heat transfer augmentation (the numerator of the thermal performance) can be less than unity whereas the friction augmentation is generally greater than unity. Hence, for very high Reynolds numbers, the thermal performance can be less than unity. In this regime, the goal is to achieve a thermal performance as close to unity as possible. A discussion of various performance evaluation criteria for enhanced heat transfer surfaces was done by Webb [23], who also provided a derivation for the thermal performance for pumping power ratio.

Friction Factor Correlations

The Blasius correlation, proposed in 1913, is one of simplest and well-known correlations for computing the turbulent friction factor in a smooth circular tube, Eq. (30). However, the Blasius correlation is limited to lower Reynolds numbers (no greater than 100k). The Blasius correlation is also less accurate compared to numerous other available alternatives. The Blasius correlation continues to remain popular because it is an explicit equation and simple to compute arithmetically. A back-of-the-envelope type calculation can easily be performed with the Blasius correlation to provide a rough and quick estimate.

$$f_0 = \frac{0.3164}{Re^{0.25}} \tag{30}$$

One of the most accurate correlations for the pipe friction factor is the so called Prandtl equation, Eq. (31).

$$\frac{1}{\sqrt{f}} = 2\log_{10}\left(Re\sqrt{f}\right) - 0.8 \tag{31}$$

Equation (31) has a theoretical basis and is valid for arbitrarily large Reynolds number, but is implicit in friction factor. It was based on previous work by Nikuradse and von Kármán. Equation (31) is therefore sometimes referred to as the Prandtl-von Kármán-Nikuradse relation. Despite the theoretical basis used to arrive at the PKN relation, it is not as popular as other correlations. One of the reasons is that the friction factor appears implicitly in the equation. The calculation of the friction factor using Eq. (31), may require an iterative solution. However, a simple arithmetic manipulation can convert Eq. (31) into a fixed-point form which is straightforward to solve and has a quadratic rate of convergence.

Li, Seem, and Li proposed a new explicit equation for computing the friction factor [24] ad-hoc as an explicit equation to closely approximate the classical PKN smooth-pipe correlations.

$$\frac{f}{4} = \frac{-0.0015702}{ln(Re)} + \frac{0.3942031}{ln(Re)^2} + \frac{2.5341533}{ln(Re)^3} \tag{32}$$

Nusselt Number Correlations

A well-known Nusselt number correlation for fully developed turbulent flow in circular tubes is the Dittus-Boelter equation, Eq. (33), which is valid for Prandtl numbers in the range of 0.6 to 160 and Reynolds numbers greater than 10,000.

$$Nu_{DB} = 0.023Re^{0.8}Pr^n \qquad\qquad (33)$$

The Prandtl number exponent is taken to be 0.3 when the fluid is being cooled and 0.4 when the fluid is being heated. The different exponents are to take into account the variation of fluid properties as it is being cooled or heated. Alternatively the Kays-Crawford correlation [25] may be used, Eq. (34). Other forms of the Kays-Crawford correlation available, Eq. (34) is given for fully developed flow in a circular tube with constant heat rate. It is valid for Prandtl numbers between 0.6-6.0.

$$Nu_{KC} = \frac{0.023Re^{0.8}Pr}{0.88 + 2.03\left(Pr^{2/3} - 0.78\right)Re^{-0.1}} \qquad\qquad (34)$$

Friction Velocity

The friction velocity is defined by Eq. (35). The friction velocity is a fundamental velocity scaled based on inner variables of the boundary (in the viscous sublayer). The local velocity normalized by the friction velocity is defined by Eq. (36). The normalized velocity is often referred to as a velocity based on inner variables. For fully developed internal flows, the friction velocity (an inner velocity), the bulk velocity, the wall shear stress, and pressure drop are all related to one another.

$$u_\tau = \sqrt{\frac{\tau_w}{\rho}}$$

(35)

$$u^+ = \frac{u}{u_\tau}$$

(36)

Because of mass continuity, a force balance on the flow in a constant area duct relates the driving pressure gradient to the wall shear stress by Eq. (38). By substituting Eq. (38) into the definition of the friction velocity, we can re-write it in terms of the pressure gradient Eq. (38). The pressure gradient is related to the friction factor, which when substituted becomes Eq. (39). Thus the friction velocity and bulk velocity are related by the friction factor Eq. (40).

$$\frac{\partial P}{\partial x} = \frac{\tau_w P_{wet}}{A_c}$$

(37)

$$u_\tau^2 = \frac{\tau_w}{\rho} = \frac{1}{\rho}\frac{\partial P}{\partial x}\frac{1}{4}\frac{4A_c}{P_{wet}} = \frac{1}{\rho}\frac{1}{4}\frac{\partial P}{\partial x}D_h \qquad (38)$$

$$\frac{1}{\rho}\frac{1}{4}\frac{\partial P}{\partial x}D_h = \frac{1}{\rho}\frac{1}{4}f\frac{1}{2}\rho U_b^2 = \frac{f}{8}U_b^2 \qquad (39)$$

$$u_\tau^2 = \frac{f}{8}U_b^2 \qquad (40)$$

Equation (40) is a rather unique property of fully developed internal flows (in constant area ducts). Flow continuity guarantees that the bulk velocity is constant (assuming constant fluid properties and constant duct area). The fully developed condition is that streamwise changes in velocity components no longer occur. As a result, the only forces acting in the streamwise direction are the pressure gradient and wall shear stress caused by friction; these two forces must then be equal by Newton's second law.

Similarity Function Approach

Semi-empirical correlations for the pressure drop and heat transfer for internal cooling channels have been developed based on the law of the wall similarity developed by Niuradse who correlated the friction data of the turbulent flow in circular pipes with added sand grain roughness [26]. Dipprey and Sabersky then developed the heat transfer similarity wall for fully developed turbulent flow in circular pipes with sand roughness [27].Webb et al. extended the friction and heat transfer roughness functions to circular pipes with repeated ribs [28]. In 1984

Han outlined a methodology for computing the four-sided ribbed duct friction factor for two-sided ribbed channels and extended the roughness functions concept to non-circular ducts with repeated ribs [29].Han proposed that the equivalent wall shear stress of the two ribbed walls be isolated by subtracting the contribution of the two smooth walls and then computing the equivalent wall shear stress and friction factor for the four-sided ribbed duct in order to compute the friction roughness function.

The roughness Reynolds number, or Reynolds number based on roughness height is given by Eq. (41). Equation (41) can be derived by computing the Reynolds number based on the roughness height and friction velocity and then using Eq. (38).

$$e^+ = \frac{e}{D} Re \sqrt{\frac{f}{8}}$$
(41)

For sand-grain roughness in circular pipes, Nikuradse [26] derived the friction similarity function, Eq. (42). In the fully rough condition ($e^+ > 70$), Nikuradse found that u_e^+=8.48.

$$u_e^+ = \sqrt{\frac{8}{f}} + 2.5 \, ln\left(2\frac{e}{D}\right) + 3.75$$
(42)

Han later derived Eq. (43) for rectangular channels by integrating the logarithmic law of the wall over the channel cross section [29] and called it the friction roughness function.

Essentially the friction roughness function is equivalent to the friction similarity function except that it was derived for a rectangular ducts.

$$R(e^+) = \sqrt{\frac{f}{8}} + 2.5\,ln\left(\frac{2e}{D_h}\frac{2W}{W+H}\right) + 2.5 \qquad (43)$$

Dipprey & Sabersky in 1963 [27] assumed that the law of the wall similarity also applies to the temperature profile. They developed a heat-momentum analogy, Eq. (44), for flow in a sand-grain roughened tube (they calculated e^+ using u_e^+=8.48 found by Nikuradse). Han derived the same formula for a rectangular duct [29] and referred to it as a heat transfer roughness function. Based on the law of the wall similarity, the concept proposed by Dipprey & Sabersky is expected to hold for any roughness where the law of the wall applies and is a fairly universal concept. However, the value of e+ and u will be different for different roughness and needs to be determined empirically. The heat transfer similarity function is related to the flow Stanton number, Eq. (45).

$$g^+ = \frac{\frac{f}{8St} - 1}{\sqrt{\frac{8}{f}}} + u_e^+ \qquad (44)$$

$$St = \frac{\frac{f}{8}}{1 + \sqrt{\frac{f}{8}}(g^+ - u_e^+)} \qquad (45)$$

Unlike the friction factor and heat transfer coefficient, which are essentially proportionality constants for the Darcy Weisbach equation and Newton's law of cooling, the roughness Reynolds number (e^+), friction roughness function (u_e^+,R), and heat transfer roughness function (g^+) are fundamental quantities based on the law of the wall similarity. These quantities are unique for a given roughness type.

Channels with Unequal Number of Ribbed Surfaces

Chandra, Alexander, & Han directly performed measurements on channels with different numbers of ribbed walls (1-sided, 2-sided, 3-sided, & 4-sided) in order to determine whether the results from channels with less than 4 ribbed walls could be used to correlate the roughness functions [30].Chandra et al. noted that additional relationships are needed between the four-sided ribbed channels Stanton number and three-sided, two-sided, or one-sided ribbed channels and that this relationship must be determined experimentally [30].

In the absence of results for channels with four-sided ribs (when measurements are performed on channels with turbulators less than four walls) the method of computing the roughness functions for equivalent four-sided ribbed channels using results from two-sided ribbed channels proposed in the 1984 by Han may be used.

Consider the friction factor of a rectangular duct with turbulators on all four walls. The friction factor for this scenario is f_{4r}. Likewise, consider the friction factor in ducts with 3, 2, or 1 turbulated walls as f_{4r}, f_{2r}, and f_{1r}. Han proposed that the friction factor of a duct with ribs on all four walls may be decomposed into an area weighted average of the contributions of individual walls. For example, Han proposed that the friction factor in a duct with one ribbed wall may be

estimated from the friction factors of a four-ribbed wall duct and the friction factor of the smooth duct, Eq. (46). Conversely, if the experiment was conducted on a channel with only one ribbed wall, the friction factor of a channel with the same ribs applied to all four walls can be estimated according to Eq. (47).

$$f_{1r} \approx \frac{W}{2(H+W)}f_{4r} + \frac{2H+W}{2(H+W)}f_0 \qquad (46)$$

$$f_{4r} \approx \frac{2(H+W)}{W}f_{1r} - \frac{2H+W}{W}f_0 \qquad (47)$$

Similarly, the friction factor for a two ribbed walled channel can be estimated from four ribbed wall performance using Eq. (48). The two ribbed wall performance is the known variable, then the four ribbed wall friction factor can be estimated two ribbed wall channel data using Eq. (49).

$$f_{2r} \approx \frac{2W}{2(H+W)}f_{4r} + \frac{2H}{2(H+W)}f_0 \qquad (48)$$

$$f_{4r} \approx \frac{H+W}{W}f_{2r} - \frac{H}{W}f_0 \qquad (49)$$

The friction and heat transfer similarity functions (sometimes referred to as roughness functions instead of similarity functions) are functions of only the roughness Reynolds number (e+) and the roughness geometry (e/D_h, P/e, α°). Webb et al. defined a family of ribs to be geometrically similar if P/e = constant and the rib shape is not varied [28]. Webb et al. did not

test ribs of other shapes but their principle can be extended to define ribs of similar geometry as having the same e/Dh, P/e, and α°, since the principle is based on the law of the wall similarity. Ribs of the same family should have the same value of the friction similarity function (u_e^+)and heat transfer similarity function (g^+) at the same roughness Reynolds number (e^+). By correlating R and G from empirical results, the friction factor and Stanton number (which is also related to the Nusselt number and heat transfer coefficient) can be obtained at other operating conditions (other e^+) or for ribs of similar shape in other configurations. If the correlations for u_e^+ and g^+ known, then all a designer must do is to specify the roughness geometry (rib shape, size, angle of attack, pitch) and choose an operating condition (e^+), the friction similarity function (u_e^+) can be obtained from the correlation. From there, the channel friction factor and can be computed from R value as well as the heat transfer roughness (g^+). The Reynolds number can be computed after e^+ and f have been obtained. Finally the Stanton number is computed after both u_e^+ and g^+ have been obtained. By repeating these calculations for all values of e^+ over the desired operating range, the designer may then draw curves for St vs Re and f vs Re to perform their analysis.

Computational Fluid Dynamics

This section provides a brief introduction to the field of computational fluid dynamics (CFD). In short, computational fluid dynamics is a branch of fluid mechanics that seeks to solve fluid flow problems numerically (nowadays on computers).

The basic procedure for performing a CFD simulation is to first define the computational domain, or its geometry. The geometry may be defined with the use of computer aided design (CAD) software packages such as SolidWorks or Pro/ENGINEER. The domain is then divided into discrete cells, the computational grid or mesh. The size of the cells in the mesh may be evenly or unevenly distributed. The cells may also have various shapes such as triangles and quadrilaterals in 2D simulations or tetrahedrals, quadrahedrals, or polyhedrals in 3D simulations. Physical modelling then takes place, where the governing equations and other relevant physical equations are specified such as the equations of motion, energy conservation, and species conservation. Finally the boundary conditions are specified; if the problem is a transient simulation, the initial conditions must also be specified.

While other techniques such as the finite difference method of finite element method may also be used for solving partial differential equations, the most popular computational fluid dynamics software packages utilize the finite volume method. The advantage of the finite volume method is that it is easier to construct the system of equations that must be solved for unstructured grids, requires less storage memory, and is faster to solve.

In the finite volume method, the governing equations (momentum and transport equations) are integrated over the control volume (otherwise written in conservative form) and then solved over the discrete volumes of the computational grid. The divergence theorem is used

to convert terms involving the divergence into surface integrals or fluxes on the faces of the control volume. Values at the cell faces must be interpolated or constructed from values of nearby cells using a numerical scheme. A set of algebraic equations are formed from the discretized equations over each cell which are then solved

The commercial software Fluent as implemented in ANSYS, Release 15.0 by ANSYS, Inc. is used as the solver in this thesis. Fluent utilizes the finite volume method approach by solving the governing equations of fluid flow over discrete control volumes defined by the computational grid or mesh and then iterating the solution repeatedly. In the next section, the problem of closure in turbulence is introduced in order to establish the background for utilizing turbulence models when attempting to solve the Navier-Stokes equations numerically.

The Problem of Turbulence

In the absence of sources and sinks, the time dependent, incompressible continuity, momentum, and energy equations are given by Eqns. (50), (51), and (52) respectively in Einstein notation. Equation (51) is the Navier-Stokes equation for an incompressible Newtonian fluid:

$$\frac{\partial \rho}{\partial t} + \frac{\partial u_i}{\partial x_i} = 0 \tag{50}$$

$$\frac{\partial u_i}{\partial t} + u_j \frac{\partial u_i}{\partial x_j} + \frac{1}{\rho}\frac{\partial P}{\partial x_i} = \nu \frac{\partial^2 u_i}{\partial x_j \partial x_j} \tag{51}$$

$$\frac{\partial \theta}{\partial t} + u_j \frac{\partial \theta}{\partial x_j} = \alpha \frac{\partial^2 \theta}{\partial x_j \partial x_j} \tag{52}$$

where $i = 1, 2, 3$, corresponds to $x(u)$, $y(v)$, and $z(w)$ coordinates (velocities) in the three dimensions, respectively. P is the hydrodynamic pressure, ρ is the fluid density, θ is the temperature, α is the thermal diffusivity, and ν is the momentum diffusivity or kinematic viscosity.

Equation (50) is a mathematical statement of the local conservation of mass principle. Equation (51) is derived by Newton's second law to a fluid volume and is a statement of the local conservation of momentum. Equation (52) is obtained by applying an energy balance to a fluid volume and is a statement of the local conservation of internal energy. Equation (52) is a simple advection-diffusion equation; in general, the energy conservation equation is more complicated and contains many physical processes distinct from advection and diffusion. For example the bulk kinetic energy and gravitational potential energy of the working fluid are omitted. When changes in elevation are small, the change in gravitational potential energy (or gravity work) may be negligible. Likewise, a change in the internal energy of the fluid as a result of changes in kinetic energy may also be negligible depending on the velocity scale and fluid properties. The heat generation as a result of viscous dissipation (fluid friction) may also be important in flows where viscous effects are dominant (which can occur in both low and high speed flows). Hydrodynamic lubrication is one application where the fluid temperature can be strongly affected by the fluid viscosity.

In principle, Eqns. (50),(51), and (52) can be solved to provide a complete description of any Newtonian fluid flow at all given points in space and time; there are 5 independent equations and 5 unknowns that need to be solved for (pressure, the three velocity components, and temperature).

Unfortunately, because of the ability of fluids to flow (either freely or against friction resistances), the advection of momentum and energy causes the Navier-Stokes equation and energy equation to be non-linear partial-differential equations. Analytical techniques for solving linear partial differential equations rely on reducing the partial differential equation to a system of ordinary differential equations. These techniques include separation of variables, method of characteristics, integral transform techniques (such as Fourier and Laplace transforms), or a clever change of variables (preferably using a similarity variable). On the other hand, there are no generalized techniques to reduce non-linear partial differential equations into ordinary equations.

An alternative approach is to solve the equations numerically, by discretizing the equations onto a computational grid or mesh. Numerical strategies for discretizing the governing equations include the finite differencing technique, finite element technique, and finite volume method. Different strategies are used depending on the application for their various advantages, such as numerical stability, computational and storage costs, or adaptability to irregular grids. The discretization reduces the partial differential equation into a system of algebraic equations which can then be solved (with the assistance of computers). However, a brute force numerical approach (called Direct Numerical Simulation) is not practical for turbulent flows because of the size of the smallest scales of turbulent motions that must be resolved, the dissipative or Kolmogorov scale. Direct Numerical Simulations (DNS) of turbulent flows are currently only feasible for simple flows at low Reynolds number because the decreased in size of the dissipative scale decreases with increasing Reynolds number. For complex flows and high Reynolds numbers, most engineering flows, immense computational resources are necessary to resolve the

dissipative eddies. Many advances will have to be made to current computational technology, equipment, and methods before direct numerical simulations are practical.

An even greater problem is that there is yet to be a guarantee that solutions to the Navier-Stokes equations even exist, or even when they do, that they are bounded. The lack of this basic property is one of the greatest unsolved problems in physics; a proof (or counterproof) for the guaranteed existence of smooth solutions to the Navier-Stokes equations was listed as one of the seven Millennium Prize Problems by the Clay Mathematics Institute in 2000 [31].

<center>The Reynolds-averaged Navier-Stokes equations</center>

Until the nature of fluid flow and turbulence is better understood, and until direct solutions to the Navier-Stokes equations are practical, engineers must continue to work with other tools that are available. One approach is to instead seek solutions to the simpler mean flow, or time average flow. When Reynolds averaging is used to time average the Navier-Stokes equation, the Reynolds-averaged Navier-Stokes equations (RANS equations) can be arrived at by decomposing the flow into a mean portion and fluctuating portion and then simplifying the resultant equation, Eqn. (53):

$$\rho \overline{u}_j \frac{\partial \overline{u}_i}{\partial x_j} = \frac{\partial}{\partial x_i}\left[-\overline{P}\delta_{ij} + \mu\left(\frac{\partial \overline{u}_i}{\partial x_j} + \frac{\partial \overline{u}_j}{\partial x_i}\right) - \rho\overline{u_i' u_j'} \right] \qquad (53)$$

The last terms on the right hand side are called the Reynolds stresses, and assigned their own tensor and symbol, Eqn. (54):

$$\tau_{ij} = \rho\overline{u_i' u_j'} \qquad (54)$$

The Reynolds stress captures the contribution exerted onto the mean motion by the turbulent velocity fluctuations. The Reynolds stress tensor has additional properties, it is symmetric. The diagonal terms in the Reynolds stress tensor are the turbulent normal stresses and the off-diagonal terms are the turbulent shear stresses. In most flows, the off-diagonal shear stress terms dominate the momentum transfer caused by the turbulent motions of the flow. The symmetric property of the Reynolds stress limits the actual independent variables in the Reynolds stress to six terms instead of nine.

In performing the Reynolds-averaging operation, six additional unknowns were introduced into the governing equations in the form of the Reynolds stresses. The appearance of the Reynolds stress makes the governing equations difficult to solve because the RANS equations are not closed, there are more unknowns than there are equations to solve. It is known from experience that turbulent flows do exist, that the governing equations are not inconsistent, and that there must be solutions to them because turbulent flows are also flows. In order for the RANS equations to be solvable, there must be additional relationships that somehow bring closure to the governing equations and relate the six Reynolds stresses (the turbulent velocity fluctuations) back to the mean flow motions. Unfortunately, all known physical principles (mass conservation, momentum conservation, and energy conservation) have been exhausted and no new equations can be derived. The lack of the needed equations is often called the closure problem of turbulence[32]. So long as a brute force direct numerical simulation is not being performed, and until the nature of turbulence is fully understood, additional turbulence models must be introduced to bring closure to the RANS equations.

Although an undesirable result, the need for turbulence models is not an indicator that the RANS equations are not suitable for describing practical problems. Many industrial devices utilize steady flow processes. For these statistically stationary flows, only the time-independent velocities and pressure variables are of interest to the designer and operator of the equipment. In these situations the RANS equations (which are Reynolds averaged in time) are the preferred equations, with an added inconvenience of requiring additional turbulence models. The ensemble averaging process eliminates the temporal dimension from the governing equations, significantly reducing the complexity of the equations as well as the computational waste. In the RANS framework, the time-averaged quantities are solved for directly without the need to solve for the instantaneous quantities followed by an averaging operation. For practical problems, seeking a time-accurate solution to the complete Navier-Stokes equation is akin to using a sledgehammer to drive a nail.

Turbulence modeling

The basis of most turbulence models makes use of the Boussinesq hypothesis or approximation, which states that the Reynolds stress is proportional to the mean strain rate tensor by the relation given in (55):

$$\tau_{ij} = \mu_t \left(\frac{\partial \overline{u}_i}{\partial x_j} + \frac{\partial \overline{u}_j}{\partial x_i} \right) - \frac{2}{3} \rho k \delta_{ij} \qquad (55)$$

where μ_t is the eddy viscosity, δ_{ij} is the Kronecker delta, and k is defined as the turbulence kinetic energy, (56):

$$k = \frac{\overline{u_i' u_i'}}{2} \qquad\qquad (\,56\,)$$

The Boussinesq approximation allows a simplification to be made by treating the effect of turbulence similar to an effect caused by molecular viscosity, hence the name eddy viscosity for μ_t. The Boussinesq approximation is not true for all flows, it holds only for simple flows. Complex flows, such as flows with strong streamline curvature, strong acceleration and deceleration (rapid contraction and expansion) do not satisfy well the Boussinesq approximation. Models that rely on the Boussinesq approximation therefore have inherent difficulty in correctly predicting flows that do not strictly satisfy the Boussinesq approximation.

The realizable-k-ε model

The realizable k- ε (rkε) was developed by Shih et al. [33] to address shortcomings to the standard k- ε model. The eddy viscosity or turbulent viscosity is updated to satisfy realizable conditions and a new model equation was developed for the dissipation (ε) equation based of the mean-square vorticity fluctuation. A modified transport equation for the dissipation rate is used in the inner region. The modified transport equation is an exact equation for the transport of the mean-square vorticity fluctuation.

Two equations models are one of the most common types of turbulence models. Models such as the k-ε and k-ω models are two popular models that are commonly used to solve engineering flows. The turbulence model used in the numerical portion of the current study includes the two equation realizable-k-ε model, an improvement of the standard k-ε model, developed by Shih et al.[33]. Two equations because are so-called because they introduce two transport equations to account for the turbulence effects of the flow in order to bring closure to

the RANS equations. The first transported variable is the turbulent kinetic energy, k. The second transported variable (in the k-ε model) is the turbulent dissipation, ϵ. The turbulent dissipation determines the scale of the turbulence motions in the flow whereas the turbulent kinetic energy determines the energy within the turbulence. Details of the implementation of the realizable-k-ε model in Fluent can be found in the Fluent Theory Guide as well as supported documentation by ANSYS.

Shear-Stress Transport k-ω Model

The Shear-Stress Transport (SST) model is a hybrid model that combines the standard k-ω mode with the standard k-ε model. In the inner region of the boundary layer near walls, the standard k-w model is used. In the outer part of the boundary layer the high Reynolds number version of the k-ε model is used. Rather than an abrupt change, the change between model formulations is done gradually through the use of hyperbolic tangent blending functions on the turbulent viscosity, production term and dissipation of ω. The formulation of the SST model by Menter [34] is used in Fluent.

v2f Model

The velocity variance model is similar to the standard k-epsilon model but incorporates some near-wall turbulence anisotropy and non-local pressure strain effects. It is a low Reynolds-number model that does not use wall functions and is valid up to the walls (similar to ω). The v2f model uses the variance of velocity to compute the eddy viscosity instead of the turbulent kinetic energy. The anisotropic effects near walls are modelled using an elliptic relaxation function (f).

Reynolds Stress Model

The Reynolds Stress model (RSM) approach does not make use of the eddy viscosity concept (does not assume that the turbulence is isotropic). For closure of the RANS equations, the RSM approach uses individual transport equations for the Reynolds stresses and an additional transport equation for the dissipation rate. The RSM approach is the most sophisticated in the RANS framework, since all six of the Reynolds stresses are directly computed and fewer assumptions are much concerning the nature of turbulence. However, the transport equations contain several terms that must be modeled. Although the RSM approach has potential to give the most physically realistic results, the modeled terms in the transport equations are not well carried out. It is possible for results computed using the RSM approach to be less accurate than the interfior two-equation models, the models used in the two-equation models have undergone much more development than the ones used in the RSM approach.

The boundary layer and near-wall treatments

The structure of the turbulent boundary layer contains large gradients of velocity and turbulence characteristics. For wall-bounded flows, the maximum shear stress occurs just off the wall. The grid resolution must be sufficient in these rapidly changing regions in order to resolve the changes.

In the outer layer, the turbulence is rapidly augmented and replenished by the production of turbulent kinetic energy generated by the large velocity gradients. Very close to the wall, viscous damping reduces the tangential velocity fluctuations whereas kinematic blocking limits the normal velocity fluctuations. Most turbulence modeling approaches are primarily valid for the turbulent core of the flow (away from the walls). Additional steps must be taken in order to

couple the turbulence models away from the wall to the near wall region dominated by viscous affects.

The non-dimensional wall distance y^+ defined in Eq. (57) is commonly used to determine the location of the first grid point with respect to the law of the wall. The friction velocity, u_τ, is defined in (58), the local flow velocity can be normalized by the friction velocity Eq. (59).

$$y^+ = \frac{y u_\tau}{\nu} \tag{57}$$

$$u_\tau = \sqrt{\frac{\tau_w}{\rho}} \tag{58}$$

$$u^+ = \frac{u}{u_\tau} \tag{59}$$

The viscosity affected region, or inner layer, of the boundary layer is typically further divided into the three regions, Table 1. In these inner coordinates expressed in terms of y^+, the linear region of the viscous sublayer extends to $0 < y^+ < 5$, the buffer layer occupies $5 < y^+ < 30$, and the logarithmic layer occupies $y^+ > 30$.

Table 1: Regions within the inner layer

linear sublayer	$y^+ < 5$
Buffer layer	$5 < y^+ < 30$
log-law region	$y^+ > 30$

In the log-law region, the non-dimensional velocity profile obeys the semi-logarithmic relationship, Eq. (60).

$$u^+ = \frac{1}{\kappa}\ln(y^+) + C^+$$

(60)

The dimensionless von Kármán constant, κ, is usually taken to be equal to 0.41; C^+ is also taken as a constant (with typically values of approximately 0.50). It is believed by many that the von Kármán constant and additive constant are universal for all boundary layers and independent of Reynolds number. George [35] reviewed the universality of the log law and pointed out that the von Kármán and additive constant are only asymptomptically constant (the case of infinite Reynolds number). George used the method of matched asymptotic matching on the inner and outer velocity scaling and proposed a new logarithmic law of the wall valid for finite Reynolds numbers. This development is important since the values for the von Kármán constant and additive constant are empirically derived from boundary layer data, where it is questionable if the tests are conducted at high enough Reynolds numbers to be in the asymptotically constant range. More recently, Hultmark et al. [36, 37] proposed a theory for the streamwise turbulent fluctuations in fully developed pipe flow based on the theoretical developments by George and others.

Very close to the wall, within the linear sublayer, the velocity profile obeys the linear relation:

$$u^+ = y^+$$

(61)

With either approach, a sufficient number of grid points must be available in the near wall region in order to resolve the gradients there. Salim & Cheah described a strategy for dealing with the wall y^+ in wall-bounded flows for different approaches [38]. The value of y^+ for the first grid point is a very important parameter since it dictates the wall layer regime of the first gird point. For meshes that have gradual changes in cell size away from the wall, the y^+ of the first grid point is a good indicator of the grid resolution and quality in the near wall region. However, the actual y^+ value depends on the solution obtained and can only be calculated after the momentum equation has already been solved. Hence it is very important to check the values of y^+ for all the grid cells near the wall bounded regions *a posteriori* in order to verify that the mesh used is adequate for the near wall modeling approach. To accurately predict the grid spacing needed to achieve a certain y^+ criteria is difficult unless the expected friction velocity is already known beforehand. For internal flows, the friction velocity is related to the friction factor. If the friction factor is known beforehand from a previous experiment, then the wall shear stress can be estimated beforehand and the grid spacing needed to achieve the desired y^+ can be selected more easily.

Two-Layer Model for Enhanced Wall Treatment

The enhanced wall treatment is a near-wall modelling method that combines a two-layer model with enhanced wall functions. The two-layer approach is needed to specify ε and the turbulent viscosity in the near-wall cells (to compute the boundary conditions for these two quantities). In the two-layer approach, the flow domain is divided into a viscosity-affected region and fully turbulent region. The division is performed by computing a turbulent Reynolds number. In the viscosity-affected near wall region, the one equation model of Wolfshtein [39] is

used to compute the turbulent viscosity. In the fully turbulent region, the k-ε or the Reynolds

Stress Model are used. The enhanced wall treatment smoothly blends the turbulent viscosity of

the inner region with the outer region using a blending function. For the momentum and energy

equation, the enhanced wall treatment also uses smooth blending functions to blend the linear

and logarithmic law-of-the-wall so that the enhanced wall treatment approach can be applied

throughout the entire near-wall region. The enhanced wall treatment is the name for this

approach implemented in Fluent. Other commercial solvers may have similar two-layer

approaches using blending functions but may not refer to the approach as enhanced wall

treatment.

Periodic Pressure Drop

The numerical simulation of periodically fully developed flows using classical treatment of the boundary conditions (pressure & velocity inlets and outlets) is an undesirable approach. With this approach, the inlet boundary condition must be known a priori. Often the inlet conditions are not well determined, since they are of little important to the experimenter who is only interested in the flow far downstream of the inlet. Additionally, the computational domain must be long enough in the streamwise extent so that the fluid flow can attain its periodically fully developed state. The extra length of the computational domain is wasted, since the variables of interest are in the region not influenced by the entrance conditions. The computational expense of simulations of periodically fully developed flows can be reduced significantly by modifying the original Navier-Stokes equations and replacing the local pressure with a periodic pressure drop. The properties of the periodic pressure drop was originally derived by Patankar, Lu, & Sparrow in 1977 [40].

The condition for regular fully developed flows is for all velocity components to remain constant with streamwise position. Regular fully developed flows are encountered only in smooth pipes or channel flows of constant area where no disturbances disrupt the fluid flow motion. The condition for periodically fully developed flows is weaker than regular fully developed flows. Periodically fully developed flows are characterized by the velocity components repeating themselves every period. The periodic velocity components are expressed in Eqns. (62),(63), &(64) for an arbitrary position (x,y) and translational period L:

$$u(\vec{r}) = u(\vec{r} + \vec{L}) = u(\vec{r} + 2\vec{L}) = \cdots \qquad (62)$$

$$v(\vec{r}) = v(\vec{r} + \vec{L}) = v(\vec{r} + 2\vec{L}) = \cdots \qquad (63)$$

$$w(\vec{r}) = w(\vec{r} + \vec{L}) = w(\vec{r} + 2\vec{L}) = \cdots \qquad (64)$$

For viscous fluid flows there is a decrease in the fluid pressure in the direction of the flow, which is needed to overcome to effects of friction at the walls. Hence the pressure field is in general not periodic. However, the pressure drop in the stream-wise direction of the flow is constant over any period, Eq. (65).

$$p(x,y) - p(x + L, y) = p(x + L, y) - p(x + 2L, y) = \cdots \qquad (65)$$

We can define a constant β to represent the pressure drop over one period, Eq. (66).

$$\frac{p(x,y) - p(x + L, y)}{L} = \beta \qquad (66)$$

The local pressure can then be decomposed into the bulk component and local components, Eq. (67).

$$p(x,y) = -\beta x + \tilde{p}(x,y) \qquad (67)$$

It turns out that the variational pressure is also periodic, Eq. (68).

$$\tilde{p}(x,y) = \tilde{p}(x + L, y) = \tilde{p}(x + 2L, y) = \cdots \qquad (68)$$

Equation (67) can then be substituted into the Navier-Stokes equations. The constant β behaves like a body force term (similar to the role played by gravity) in the momentum equation. β may be provided beforehand as a parameter, which is equivalent to specifying a particular pressure drop. If on the other hand, the control variable is a particular Reynolds number, then β may be iterated in the outer iterations until the desired flow rate is achieved. In Fluent, β is updated during the pressure correction step of the SIMPLE algorithm used in Fluent based on the difference between the actual and desired mass flow rate of the flow.

For flows with a constant heat input (uniform heat flux) the periodic temperature gradient, like the pressure drop, is also constant, Eq. (69), where the temperature drop can be determined based on the total heat addition, Q, using Eq. (70).

$$\frac{T(x+L,y) - T(x,y)}{L} = \frac{T(x+2L,y) - T(x+L,y)}{L} = \sigma \tag{69}$$

$$\sigma = \frac{T_{b,exit} - T_{b,inlet}}{L} = \frac{Q}{\dot{m}c_p L} \tag{70}$$

where the total heat rate is known if a uniform specified heat flux condition is used. The specified heat flux approach is used in this study. The value of the heat flux applied used is different for each Reynolds number. The necessary heat flux to obtain a bulk temperature increase of 10 K over the periodic domain is calculated beforehand from the mass flow rate at each channel Reynolds number.

The periodic flow conditions are not easy to manipulate for complicated flow physics. A discussion of their suitability to different flow configurations and their limitations can be found in the Fluent Theory Guide.

CFD BENCHMARK

Commercially available and in-house computational fluid dynamics software packages are a popular tool for investigative research and engineering design. Changes to a component design can be rapidly modified in a numerical simulation, whereas the time taken to construct a new experiment is much longer. The cost of running a numerical simulation is often less than the cost to carry out a sufficiently detailed experiment.

An extensive set of numerical simulations are performed using Fluent to compare the results of the CFD based predictions against an empirical correlation given by Webb et al. [28]. The goal is to ascertain what level of accuracy can be expected from a numerical simulation.

Reference Dataset

Webb et al. [28] performed a number of measurements on the pressure drop and heat transfer in circular tubes with repeated-rib roughness. A diagram of the tube with the installed rib-roughness tested by Webb et al. is shown in Figure 9. The ribs are orthogonal to the stream-wise flow direction and applied around the entire pipe. Figure 10 is a sketch of the instrumentation used by Webb et al. to perform their measurements.
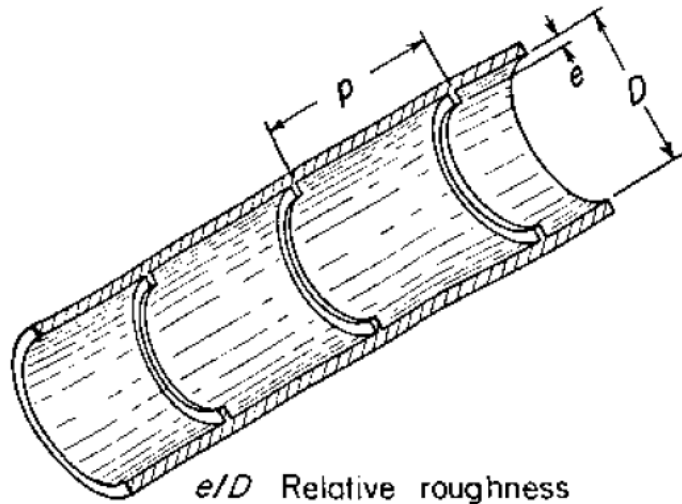
e/D Relative roughness

p/e Relative rib spacing

Figure 9:Characteristic dimensions of repeated rib-roughness [28]

RT − Resistance thermometer   ΔP −Pressure drop

T − Thermocouple   V −Test section voltage
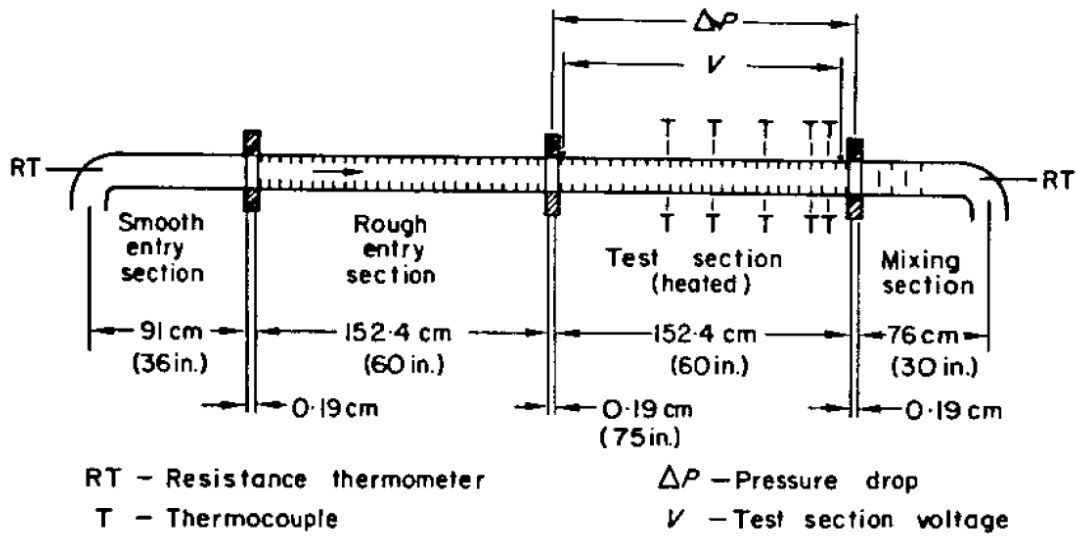
Figure 10: Sketch of experimental setup used by Webb et al. [28]

The test matrix of experiments conducted by Webb et al. is summarized in Table 2. Three difference sized rib roughness were tested, at relative pitches of 10, 20, and 40. Webb et al. also used different working fluids to capture the influence of the fluid Prandtl number.

Table 2: Test matrix for [28]

Tube	$\dfrac{e}{D}$	$\dfrac{P}{e}$
01/10	0.01	10
02/10	0.02	10
04/10	0.04	10
02/20	0.02	20
02/40	0.02	40

Webb et al. computed friction factors from the measured pressure drop and used these to compute the friction similarity function, shown in Figure 11. The g^+ parameters are shown in Figure 12.
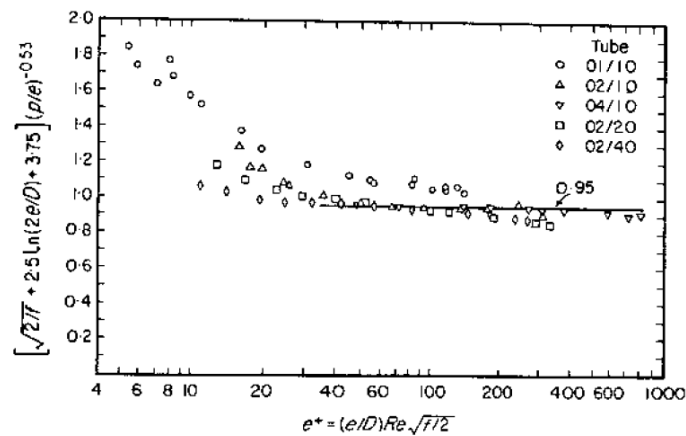
Figure 11: Friction correlation for repeated-rib tubes [28]
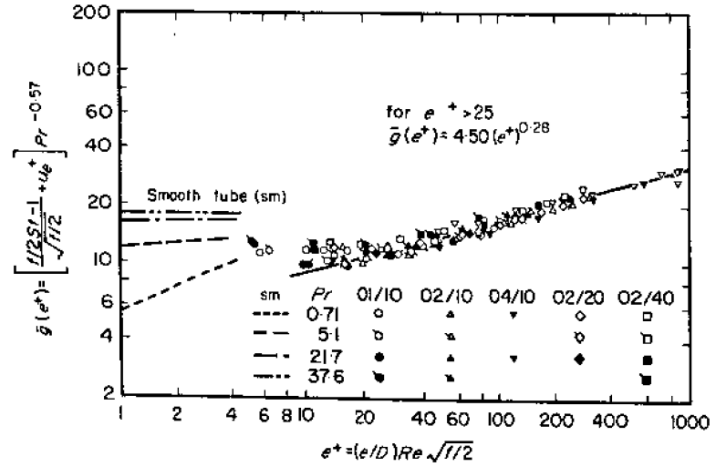
Figure 12: Heat transfer correlation for repeated-rib tubes [28]

As shown in Figure 11 and Figure 12, Webb et al. were able to correlated their experimental data with Eq. (71) and Eq. (72). The correlation is valid over the range of $0.01 <$ e/D < 0.04, 10 < P/e < 40, 0.71 < Pr < 37.6. Webb et al. were the first investigators to correlate the friction and heat transfer roughness parameters for a tube with repeated rib-roughness (essentially a rib-turbulated channel).

$$u_e^+ = 0.95 \left(\frac{P}{e}\right)^{0.53} \qquad\qquad (\,71\,)$$

$$g^+ = 4.5 e^{+0.28} Pr^{0.57} \qquad\qquad (\,72\,)$$

Webb et al. later generalized their correlation and extended it further [41].

<u>Problem Setup</u>

The computational domain, Figure 13, is the ¼ sector of a pipe of nearly identical

geometry as the 02/10 used by Webb et al. The choice of the 02/10 tube was to minimum the

overall computational cost of the all the simulations being performed. The computational cost is

lowest for the smallest domains. The 01/10 tube, which had the smallest rib height and would

have resulted in the lowest computational cost, was avoided because the experimental results for

that particular tube had the greatest deviation from the empirical correlation. Hence the 02/10

tube was chosen, since it was the smallest rib height and shortest pitch of the remaining cases.
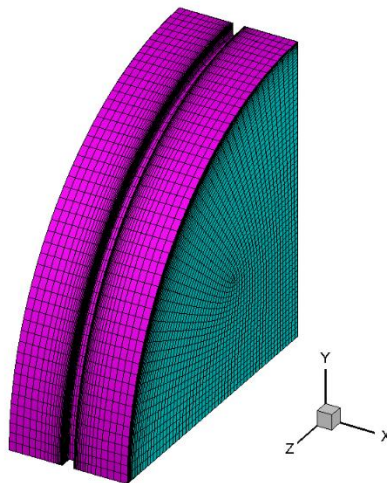
Figure 13: Computational domain

The pipe diameter used in the numerical simulation is 2 inches in diameter (50.8 mm). The dimensions of the rib-roughness are scaled accordingly to achieve the relative roughness of 0.02. The stream-wise extent of the computational domain is a single rib pitch. Symmetry boundary conditions are applied to the Y=0 and Z=0 surfaces. No-slip walls are applied accordingly to all surfaces of the pipe wall. Periodic boundary conditions are applied to the inlet and exit faces.

The simulation is performed under steady state conditions using the pressure based Navier-Stokes solver. Air is used as the working fluid. All fluid properties are taken to be constants. The thermodynamic properties of air were computed from REFPROP v9.1 at an operating temperature of 300 K and operating pressure of 101325 Pa.

The 2nd order upwind scheme is used for the spatial discretization of the all the advection terms, the 2nd order central scheme is always used for the diffusive terms. The SIMPLE scheme is used for the pressure-velocity coupling. The multidimensional gradient limiting scheme was used, the multidimensional scheme is less restrictive than the default standard limiting scheme.

The computational mesh is generated by the mesh generating utility GridPro. A grid refinement study was also performed to compute the grid convergence index. Grid refinement is performed systematically by halving the grid spacing uniformly in all directions, an 8x increase in cell count for each refinement. Table 3 lists the total cell count (number of control volumes) for each grid.

Table 3: Mesh summary for grid refinement study

	Cell Count
N1	2,800,896
N2	404,736
N3	59,328

Various views of the computational grid are shown in Figure 14 for N3, the coarsest grid.

N2, the medium grid is shown in Figure 15 and N3, the fine grid is shown in Figure 16. The

coarse and medium grids were needed to compute the grid convergence index. Results presented

are taken from the simulations obtained from N1, the fine grid.
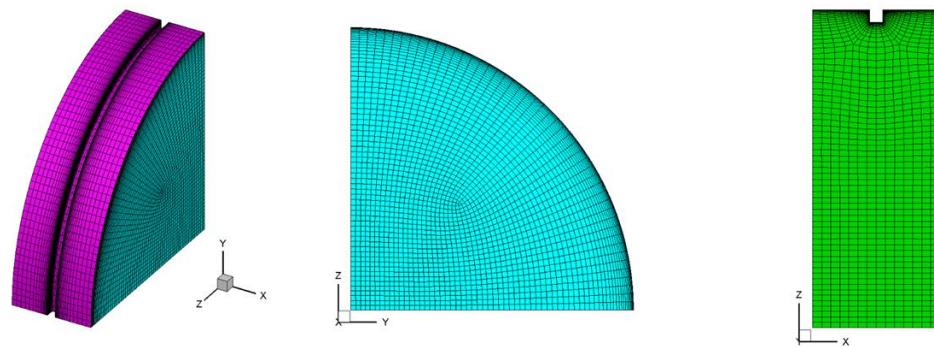
Figure 14: Projective view (left), at inlet (center), on symmetry plane (right) of N3 grid
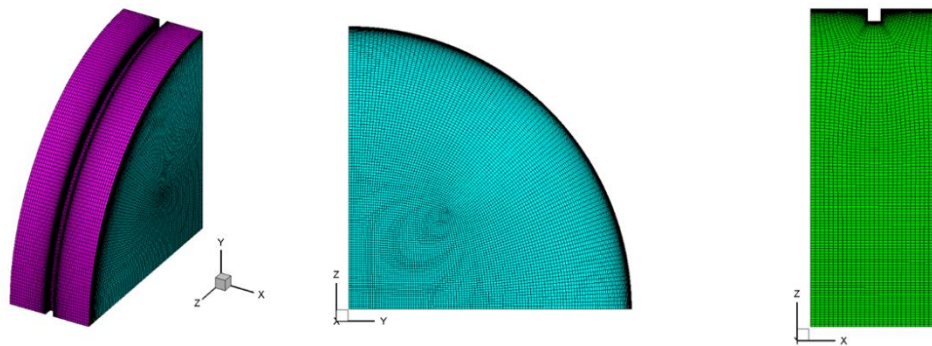
Figure 15: Projective view (left), at inlet (center), on symmetry plane (right) of N2 grid
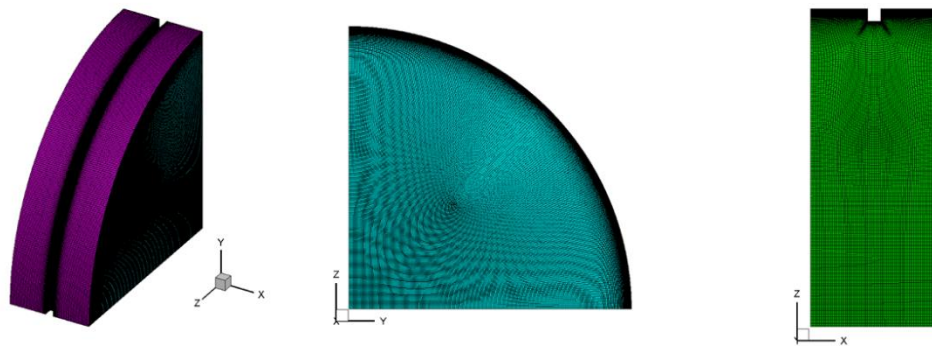
Figure 16: Projective view (left), at inlet (center), on symmetry plane (right) of N1 grid

Ten Reynolds number conditions are simulated, equally distributed over the range of the empirical correlation (10,000 to 100,000). Four turbulence models are used, the realizable k-epsilon model (with enhanced wall treatment), the k-omega SST model, the velocity-variance (v2f) model, and a linear pressure strain k-epsilon based Reynolds Stress Model (with enhanced wall treatment). A total of 120 numerical simulations were computed.

67

Figure 17 is a contour plot of the wall y^+ values taken from the 100k Reynolds number simulation using the RSM model. The maximum y^+ encountered was approximately 1.4, with the average of all the surface nodes of about 0.2. The maximum y^+ value is sufficiently low (less than 5); the near wall modelling approach is equivalent to a low-Reynolds number approach when the y^+ is globally in the linear regime. Because of the increased pressure drop and wall shear stress at higher Reynolds numbers, the y^+ values tend to be highest at the highest Reynolds numbers. Since the y^+ values for the 100k Re simulation were adequate, the y^+ for lower Reynolds will also be adequate.
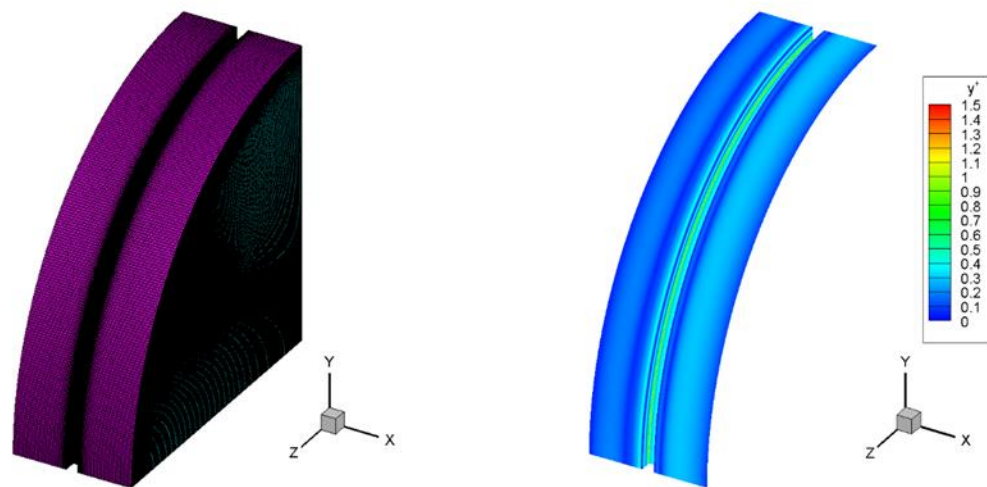
Figure 17:Contours of wall y^+

Results

The bulk channel pressure gradient was extracted from each simulation and used to compute the channel friction factor. The friction factors for all the cases simulated are shown in Figure 18. The friction factor was subsequently used to compute the roughness Reynolds number

and friction similarity function, which is plotted in Figure 19. The values predicted by the Webb et al. correlation are also plotted in the figures. Vertical bars are also plotted on each symbol, these bars correspond to the computed grid convergence index by comparing the solution of the fine grid with the medium and coarse grid. For most of the numerical test points, the value of the grid convergence index is rather negligible, less than 1%. Some of the test points with more visible error bars have a GCI on the order of 2-5%.
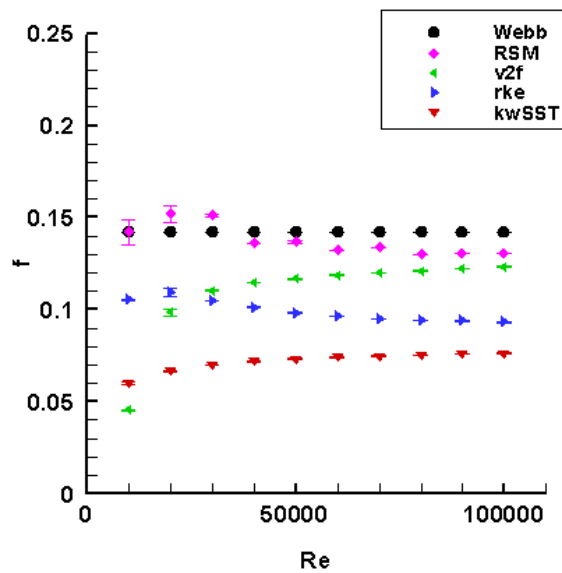
Figure 18: Friction factor of 02/10 tube predicted by CFD

The friction factors obtained using the RSM turbulence model has the best agreement with the correlation (~10%). The results from other turbulence models are not as optimistic. Other than the RSM model, the remaining models had difficulty predicting a constant friction factor, with the SST and v2f models predicting increasing friction factor and realizable k-ε predicted a slightly decreasing friction factor. If the availability of the correlation by Webb et al. is set aside, the lack of agreement between the numerical predictions using various turbulence

models can have disturbing consequences. Based on the numerical simulations alone it would be difficult to determine the true value of the friction factor from the remaining information. One might guess that since the RSM model is the most sophisticated, that it provides the most accurate results, which is the case for this particular configuration. In the absence of external data to verify the results, this approach might be justifiable.
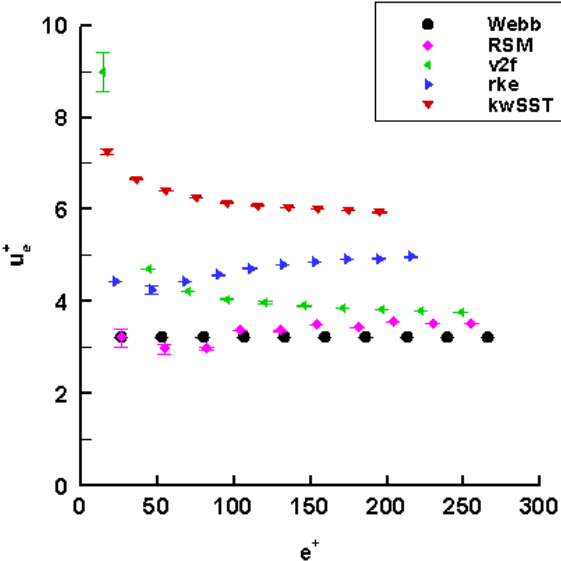
Figure 19: u_e^+ for 02/10 tube predicted by CFD

Because of the large number of simulations that had to be performed in order to generate the results plotted in Figure 18 and Figure 19, the 02/10 tube tested by Webb et al. had been selected because it afforded the smallest computational domain. Even with the smaller tube dimensions, the domain had been reduced to a ¼ sector and periodic conditions used to simulate only a single rib pitch which still resulted in a grid consisting of 2.8 million cells. Industrial simulations are characterized by much larger problem geometries and more complex physical modeling. A three-pass serpentine channel such as those found in turbine rotor blades can have

in excess of 20-30 rib turbulators. The grid size to simulate that type of channel would require on the order of 200 to 300 million cells if a similar spatial resolution is used. We also performed the simulation using constant fluid properties. Industrial simulations often have to compute an equation of state, such as the ideal gas equation of state, in order to compute other fluid properties that can change significantly with temperature and pressure (viscosity, conductivity, etc). The computational demands of industrial problems are massive compared to this academic study. For these reasons, industrial simulations are most commonly performed with the two equation k-ε or k-ω models.

Suppose then that the investigator is such an individual who does not have the capacity to perform a simulation with the v2f or RSM models, leaving only information from the SST k-ω and k-ε models. In this situation, the investigator would not have the means to conclude that the predictions from the SST k-ω and k-ε models are far from the actual performance of the ribbed cooling circuit. The investigator would perceive that there is a 20% between the predictions of the SST k-ω and k-ε models and might even estimate that the actual performance of the cooling circuit is in-between the predictions of the two models (by taking an average).

Consider yet another situation where a component designer had performed their CFD simulations using the SST k-ω and k-ε models to design their part. An external team of researchers was also able to fabricate an experimental setup to measure the performance. The results from this hypothetical experiment yielded anyway the results obtained by Webb et al. Under this circumstance, the designer would see that there is up to a 50% discrepancy between their CFD predictions and the experimental results submitted by the team of researchers. Depending on external factors (the level of mutual trust between the designer and

experimenters), one of the groups might dismiss the results obtained by the other group. The

experimenters might claim that the CFD simulation is not accurate. Simultaneously the designer

might claim that predictions from different turbulence models both yielded results outside the

neighborhood of the experiment and therefore the experimental technique must be flawed.

However, both groups will agree that the 50% deviation is ridiculous.

Sufficient understanding, knowledge, and virtue amongst both parties is needed to defuse

this situation. A thorough understanding of the limitations of the experimental techniques

involved as well as the limitations of CFD-based predictions are needed for both parties to accept

the results as is.

The discrepancy of the friction factor prediction from the CFD simulation compared with

the correlation by Webb et al. is plotted in Figure 20, expressed as a percentage (the difference is

divided by the value taken from the correlation). A similar plot of the discrepancy for the friction

similarity parameter is given in Figure 21. The percentage discrepancy between the friction

factor and friction similarity function for each turbulence model is listed in Table 4, the

discrepancies at each Reynolds number is combined by taking the root-mean-square of the

differences.
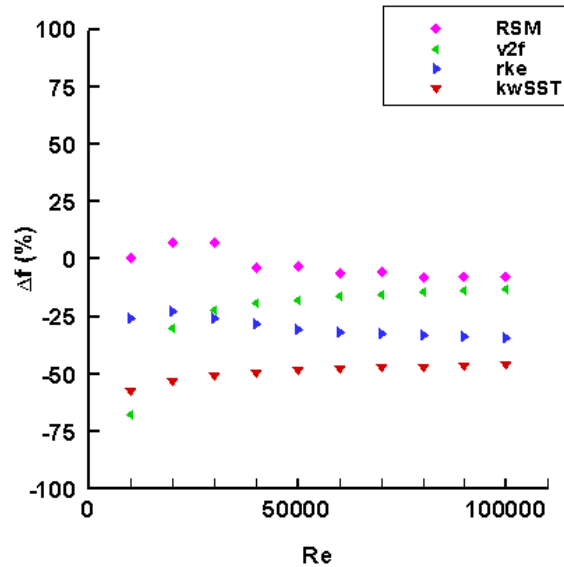
Figure 20: Discrepancy of friction factor between CFD and correlation

The RSM model performed the best, within 7% of the friction factor results of Webb et al. The v2f and realizable k-ε on the average under-predicted the friction factor by nearly 30%. The v2f model was extremely inaccurate at the lowest Reynolds numbers (~60%) but performed much better with higher Reynolds numbers (10-20%). The realizable k- ε under-predicted the friction factor by 25-35% but was more consistent with its predictions than the SST k- ω and v2f models. The SST k-ω consistently had the worst predictions, with deviations 45-60%.
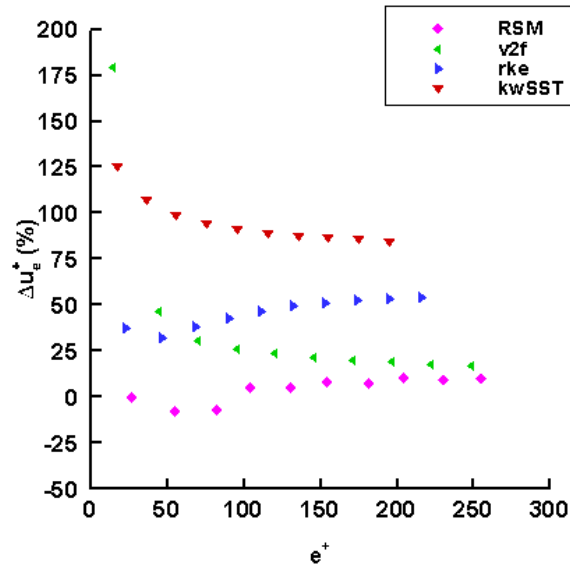
Figure 21: Discrepancy of u+ between CFD and correlation

Because the friction factor appears in the denominator and inside a square root operator, the errors in the friction factor are amplified when the friction similarity parameter is calculated (because the friction factor is typically less than 1). The same trends observed for the friction factor are repeated for the friction similarity function, but with increased magnitudes. Correlations for the friction performance of various turbulators are best performed using the fundamental friction similarity parameter because of its theoretical basis and universal nature. Unfortunately, the similarity parameter more sensitive than the friction factor, making correlations of the friction similar parameter more difficult without the availability of accurate measurements.

Table 4: root-mean-square deviation of friction factor and friction similarity parameter

Turbulence Model	Δf	Δu_e^+
k-ω SST	49%	96%
rkε	30%	46%
v2f	27%	62%
RSM	7%	8%

The numerical benchmark performed attempted to be an exhaustive approach, by using all four of the most popular turbulence models accompanied by a grid refinement study for each model and Reynolds number tested in order to clear any immediate concerns. The deviation between the predictions using CFD are, frankly, unpredictable. A variety of friction factors was predicted depending on the turbulence model used. It is acceptable for CFD simulations to predict results that may not be numerically exact as long as designers that use CFD are able to determine where their predictions are good and where they are not so good. Hence, the best use of CFD as an engineering tool occurs when it is complemented with appropriate experimental results.

THERMOCHROMIC LIQUID CRYSTALS

Introduction to TLC

Thermochromatic Liquid Crystals, also known as thermochromic liquid crystals, are color changing crystals whose color depends on temperature. TLCs are derived from optically-active mixtures of organic compounds and have a chiral (twisted) molecular structure. The use of TLC is widespread; a good example is in the medical industry where TLC is commonly employed as a disposable thermometer for accurately measuring the human body temperature. The liquid crystals' ability to modify incident white light is attributable to a combination of certain optical phenomena: birefringence, circular dichroism, and Bragg diffraction. An in-depth explanation of the specific tunable properties of thermochromic liquid crystals can be found in the Handbook of Thermochromic Liquid Crystal Technology [42].
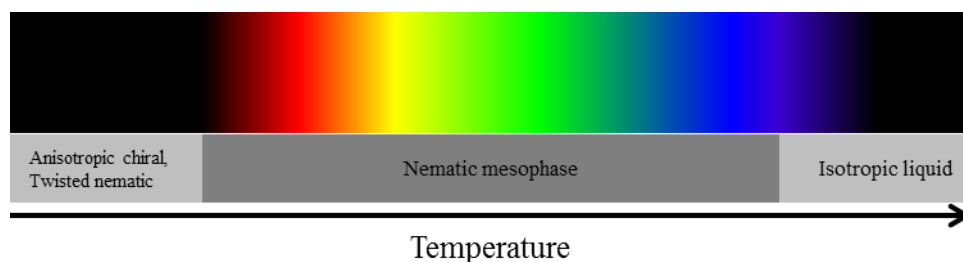
Figure 22: TLC bandwidth and crystallic phases

The color play is the temperature range over which the liquid crystal mixture exhibits changes in temperature. The crystal mixture is colorless below the color play, becomes red when a characteristic temperature is reached (the red start) and then transitions through the entire visible light spectrum until it exceeds the color play bandwidth and turns colorless again.

Although often referred to as colorless, the bare TLC mixture color when outside the bandwidth is cloudy and still visible to the naked eye. Typically, the red color appears at the lower operating temperature and blue or violet appears at the higher operating temperature, although specialized liquid crystal mixtures are capable of the opposite. Temperature-insensitive formulations of TLC mixtures are also available, this formulation is sensitive to shear and is used to measure the wall shear stress in aerodynamic research. Temperature insensitive formulations reflect only a single color below the transition temperature and change to colorless above it [42].

A black backing is typically employed to absorb any light not reflected by the liquid crystals in order to improve color contrast. The black backing is not required for the TLC to change color with temperatures but is so easy to implement that it is nearly always applied. The liquid crystal mixture can be systematically varied to change the temperature at which the red or green start appears or to achieve a certain color play bandwidth. The selective reflection of certain wavelengths by the crystal structure of the mixture as it changes crystallic phases can be obtained by tuning the individual components of the liquid crystal mixture. TLC manufacturers can produce mixtures with a bandwidth as low as 1 K and can control the red or green start temperature occurrences to less than 1 K. The sprayable form of TLC based paint is used in the current study.

TLC mixtures may be unsealed or microencapsulated. Generally the unsealed mixtures are highly susceptible to degradation and must be well protected to be used successfully. The microencapsulation process packages small droplets of the TLC mixture with a polymer coating. The size of the microcapsules is on the order of a few microns to a few millimeters [42]. The polymer coating protects the TLC mixture trapped inside and also inhibits further degradation.

77

As a result of the microencapsulation process, different microcapsules can be freely mixed together to produce TLC mixtures with multiple color plays [42].

<u>From Color to Temperature</u>

The typical color response of a TLC mixture is demonstrated in Figure 23. One approach to obtaining the temperature from the color of the TLC mixture is to quantize color using a hue which maps a cylindrical coordinate to the color and is inspired by the color wheel. Two popular hue based representations of the RGB color model are the HSL (Hue-Saturation-Lightness) and HSV (Hue-Saturation-Value) methods.
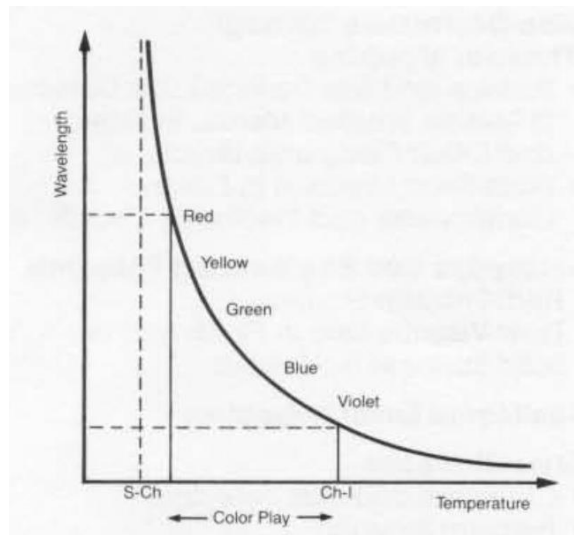
Figure 23: Typical TLC response [42]

The RGB color model on the other hand is an additive or mixing model of the three primary colors (red, green, and blue). Various amounts of red, green, and blue are added or mixed together to reproduce the color spectrum. The corresponding RGB coordinates for hue (for colors taken at their maximum saturation) is shown in Figure 24 .
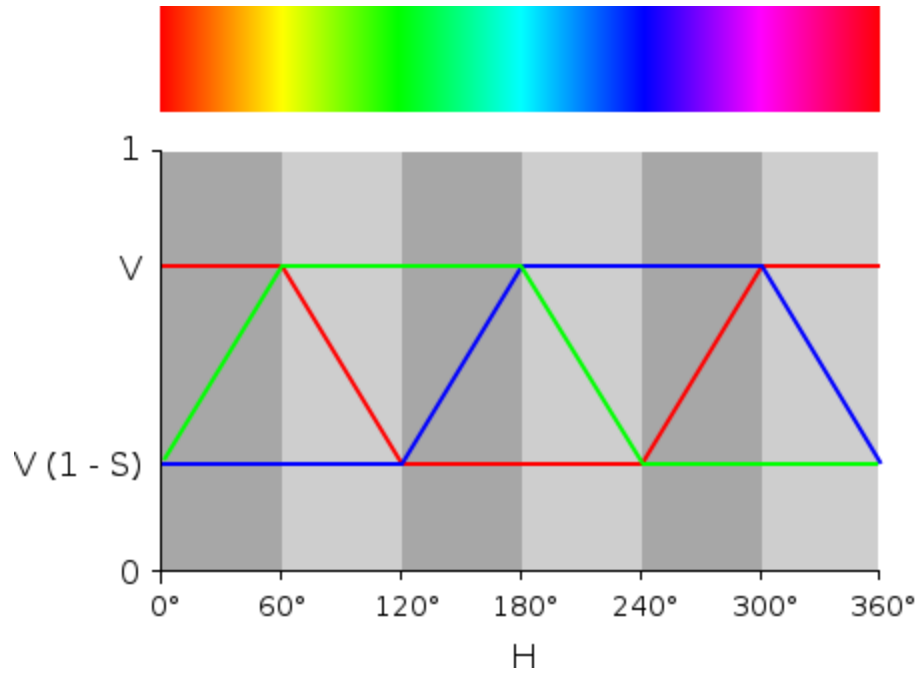
Figure 24: HSV, HSL, RGB comparison

One technique for utilizing TLC in a transient heat transfer experiment utilizes the RGB color model. Figure 25 is an example of the calibrated RGB response of a TLC mixture, showing how the intensity of the RGB components change with temperature. The temperature at which the peak intensity occurs, is a unique property of the TLC mixture. This characteristic may be utilized in a transient heat transfer experiment by scanning the time-history of the RGB signal for the peak intensity. Figure 26 is the RGB response at a single pixel taken from the recorded video of a transient TLC experiment.
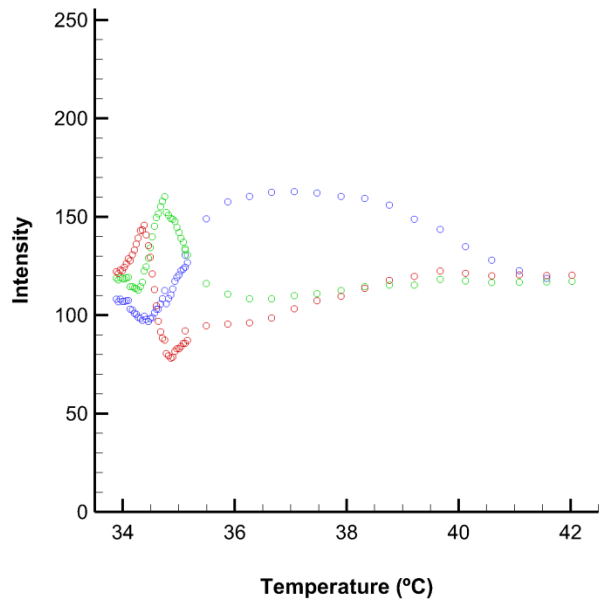
Figure 25: RGB response of TLC from calibration
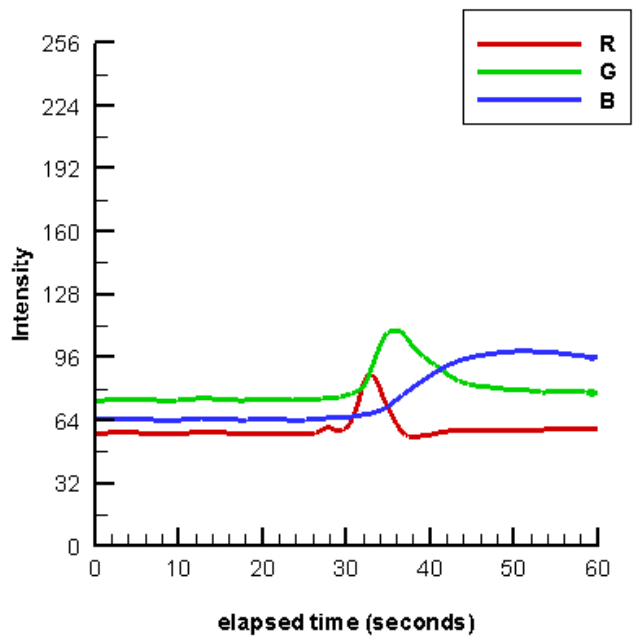
Figure 26: RGB response of TLC during experiment

80

At the peak intensity or maximum, of the R, G, or B signals the temperature of the crystals is known. This temperature, which needs to be determined by calibration beforehand, along with the time at which the peak intensity occurs is provided as inputs to the heat conduction model. The red and blue color signals are often neglected in RGB-based techniques because the green signal is the most distinct and accurate. However, the red signal has been observed to have similar characteristics as the green signal in narrow band TLCs, although no investigators have attempted to exploit it until now. While doable, the determination of the peak blue intensity temperature during both calibrations and during the experiment are less accurate than the red and green signals because of the broader curves.

Color-temperature profiles supplied by manufacturers at the point of origin may differ from the ones in the laboratory. Hence, calibration is essential procedure that needs to be performed in order to obtain a relation between the peak intensities and temperatures so that the crystals can be used as temperature indicators during the transient heat transfer experiment. Abdullah et al. .[43] discussed liquid crystal calibration methods in great depth. Because of the numerous influences that can affect the perceived peak color intensity, calibration of the TLC response should be performed under similar environmental conditions representative of their intended use. Kakade et al. [44] studied the influence of viewing angles (20°, 28°, 34°, and 45°) on the calibration of narrow-band and wide-band crystals. However, Kakade et al. focused primarily on the hue rather than the raw RGB signals.

Characterization of TLC

This section focuses on the calibration of narrowband thermochromic liquid crystals using the RGB method. The TLC was calibrated on a copper block with thermistors and recorded with 3CCD cameras placed at 0°, 15°, 30°, and 45° incidence angles. The influence of the viewing angle on the perceived peak temperature is investigated as well as the stability of TLC characteristics after long periods. Previous investigators have focused on only the green color peak. In this section, it will be demonstrated that the calibration of TLC yielding two distinct color peaks (for the red and green signal) are feasible and can be accurately obtained.

Calibration Apparatus

The calibration procedure involved measuring the RGB intensity of a TLC coated surface as a function of temperature. The calibration was carried out using a copper-block apparatus. The copper block had dimensions of (9 in x 9 in x 3/8 in). Blind holes were drilled into the backside of the block to the half-depth at the centers of the four quadrants marked in Figure 27. Thermistors were placed into the drilled holes and packed with thermal paste. Q-Foil graphite based heaters from EGC Enterprises were attached to the back of the coper block and covered the thermistors (PR302J2 with a nominal resistance of 50,000 Ω at 25°C).

The front side of the copper block, opposite the foil heater, was the base for the black backing (SPB100) and TLC. The black backing was used to enhanced the color contrast of the TLC and eliminate the color of the copper surface underneath. The TLC mixture (SPN100G35C1W) was used without further modification as purchased from LCR Hallcrest and was airbrushed evenly on top of the black backing. The setup was then encased in ½ inch thickness PMMA as shown in the left of Figure 27.
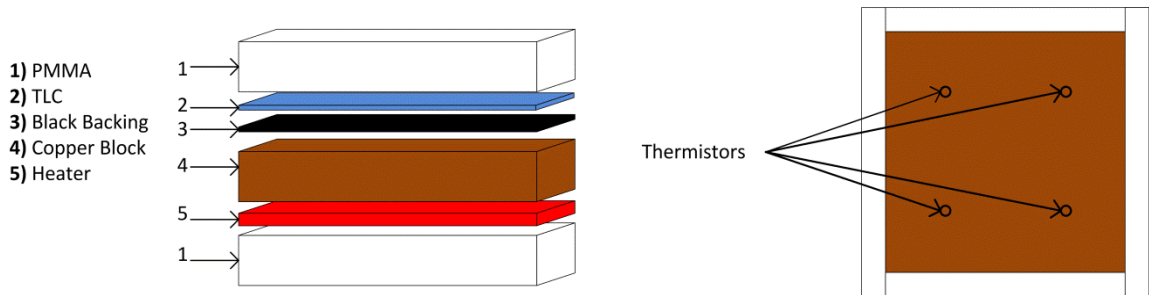
Figure 27: Calibration apparatus (left), Thermistor layout (right)

The copper block was laid horizontally on an aluminum extrusion frame with anti-vibration mounts the TLC surface facing downwards. The heaters were powered with a single-phase 120 Volt autotransformer. The thermistor resistances were measured by a 6½-digit multimeter (Keithley 2000). The multimeter was not multiplexed; only the resistance of a single thermistor was used to determine the block temperature. The measured resistance from the redundant (the other three) thermistors was used to check for any spatial variation in the block temperature. The measured variation was found to be marginal (less than the accuracy of the temperature measurement).

Four 3CCD cameras (Panasonic PV-GS180) with a resolution of 720 px x 480 px and T-12 fluorescent lights (97 CRI 5000 K, bulb temperature) were placed on the bottom of the setup, facing the copper block. The cameras were position to achieve an angle of incidence of 0°, 15°, 30°, and 45°. The setup was then covered Roc-lon Blackout fabric to eliminate ambient lightning. The calibration setup used is sketched in Figure 28.
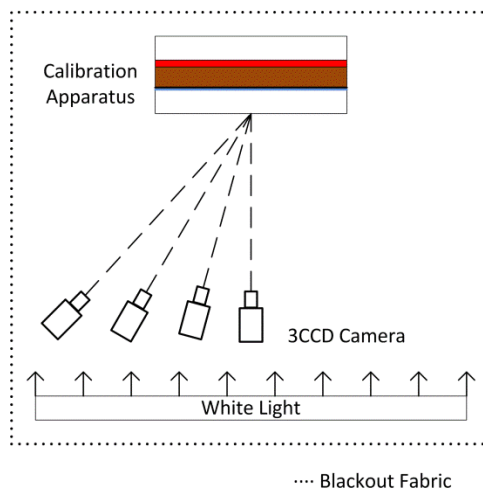
Figure 28: Calibration Setup

Calibration Procedure

The calibration was performed in a sequential heating followed by a cooling experiment. The lights in the facility were turned off and the T-12 fluorescent lights and Panasonic cameras were turned on. The Variac transformer was slowly turned on and adjusted until a base temperature of near 32 °C, just before the appearance of red. The resistance of the thermistor was recorded once the reading on became steady. 30 images were collected at a frame rate of 30 fps simultaneously on all four cameras. This process was repeated for multiple temperatures by carefully controlling the heater voltage until just beyond the blue clearing point, which occurred at approximately 42 °C,. The temperature was carefully monitored to not exceed 45 °C in order to avoid exceeding the color bandwidth, which has been reported to cause permanent damage to the TLC. A similar cooling experiment was performed by slowly decreasing the heater voltage. With the current setup, a temperature resolution of 0.001 °C was achieved, although the actual step between temperature measurements performed was greater. Larger temperature increments

of 0.4 °C were used in non-interesting regions and temperature steps of 0.04°C were clustered around the regions of peak intensity. The resistance readings, manually recorded, were precise to within 5 Ω. The resistance measurements of the thermistors are converted to temperature using the Steinhart-Hart relation with the appropriate coefficients for the thermistors used.

Post-Processing was performed using an in-house MATLAB code. The average pixel intensity of the 30 images was taken to be the intensity reading of the pixel for the given temperature. For each pixel, the peak intensity occurrence for each signal (R, G, and B) is determined and the temperature of that particular test is used as the peak color temperature for the particular pixel. The average peak temperature of all the available pixels is taken to be the temperature corresponding to the maximum intensity; the deviation of individual pixels from the calculated average was less than ±0.15 °C but is influenced by the temperature resolution of the calibration experiment. Because of the viewing angle, lower spatial resolution is available for the cameras mounted at the greater angle of incidence. For the camera mounted at 0° incidence, typically 160,000 pixels were available for averaging.

Calibration Uncertainty

The calculated uncertainty for the final results was performed using the procedures described by Kline and McClintock, Moffat, and PTC 19.16 for a 95% confidence level. Because of the large sample size (number of pixels) in the average temperature of each maximum intensity, the precision error in the determined temperatures is negligible compared to the uncertainty of the copper block temperature itself. The temperature change over the interval that the images are being recorded were found to be less than ±0.0015°C. The base thermistor accuracy was ±0.05°C. The typical uncertainty in a given resistance measurement was ±6 Ω

(precision of the reading plus accuracy of multimeter). The error propagation of the resistance

measurement to the temperature amounted to ±0.046 °C. The overall uncertainty in the copper

block temperature was therefore ±0.07 °C, it was assumed that the spatial temperature variation

was negligible. Additional analysis is needed to quantify the spatial temperature variation in the

copper block (temperature gradient across the block thickness and laterally on the block surface).

Calibration Results

Figure 29 plots the RGB signal intensity for each of the cameras (at 0º, 15º, 30º, & 45º) at

a single pixel. The relative pixel location is at the center of the block. The physical location may

be different for the different cameras. Data points from the slow heating experiment are plotted

using their respective colored symbols. Corresponding black symbols are the data for the cooling

experiment. To determine the characteristic temperatures, the RGB curves in Figure 29 are

scanned for the peak intensity (a maximum value search). The corresponding temperature at this

intensity is the characteristic TLC temperature for the color signal. Table 1 lists the characteristic

peak intensity temperatures corresponding to the pixel shown in Figure 29.

Table 5: Characteristic temperature for individual pixel

Angle of Incidence	Heating Experiment			Cooling Experiment		
	Red (ºC)	Green (ºC)	Blue (ºC)	Red (ºC)	Green (ºC)	Blue (ºC)
0°	34.40	34.75	35.78	34.37	34.73	35.79
15°	34.37	34.71	35.70	34.34	34.69	35.72
30°	34.34	34.68	35.57	34.31	34.63	35.63
45°	34.30	34.61	35.35	34.26	34.57	35.35

0°   15°

30°   45°
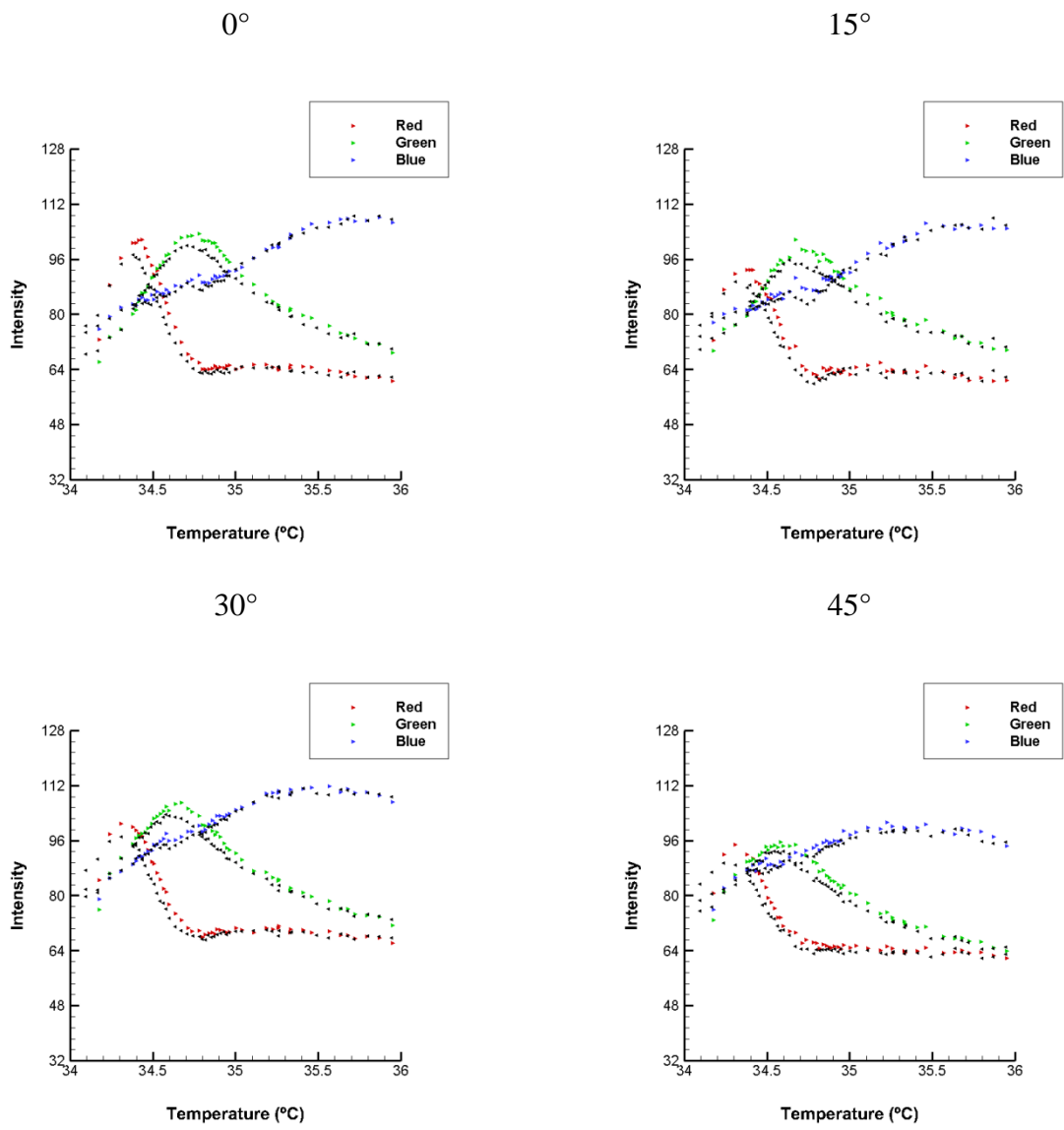
Figure 29: RGB response for 0° (top-left), 15° (top-right), 30° (bottom-left), and 45° (bottom-right)

The intensity of the green peak was the strongest but the red peak had the same quality. The red signal distribution is narrower than the green distribution as is commonly understood; hence, the greater difficulty of calibrating the red signal and past-justification for discarding the red signal in previous single-color TLC experiments. However, the temperature resolution of the current setup is able to resolve the peak intensity of the red signal to acceptable levels. At the normal angle of incidence the blue intensity distribution was too broad and the blue peak intensity could not be determined to a desirable accuracy. Unlike the red and green signals which have a distribution around the mean of ~1 °C, the blue signal is sparser and is distributed across 5 °C. Even if the blue peak intensity could be determined accurately in the calibration experiment, there is still the difficulty of determining the occurrence of the blue peak intensity during a transient TLC experiment which negates the usefulness of calibrating the blue peak.

An initial concern may be that the curves for the heating experiment and cooling experiment do not fall completely on top of one another; the Intensity vs Temperature curves for the heating experiment are different than the cooling experiment. This behavior was observed for all four viewing angles and also found on other selected pixels. In general, it should not be expected that the same Intensity vs Temperature mapping be exactly reversible under heating or cooling conditions.

Although the intensity levels for heating and cooling experiments are not repeated exactly, the influence of this effect on the characteristic temperatures is minor. A comparison of the characteristic temperatures for the heating and cooling experiment shows that the worst different is 0.05 °C for the red and green signals, and up to 0.08 °C for the blue signal (which is on the order of the temperature resolution of the calibration). At this point, the physical

mechanism for the different response of the TLC during a slow heating event and slow cooling event are not clear. Kakade et al. [44] documented a similar effect in their calibration, where the hue was also found to be different for heating and cooling cycles. Unfortunately, the only known calibration apparatus comparable to our setup in terms of accuracy and methodology is the setup used by Kakade et al. The limited number of instances where these results have been documented makes it difficult to make inferences about their general nature.

The results in Figure 29 and Table 5 utilized the RGB response of an individual pixel. The characteristic temperatures determined from a single pixel can be considered a single sample of a many sample experiment. The true characteristic temperatures can be estimated from the mean of all observations (average of all pixels).

Heating vs Cooling Experiment

In the earliest calibration experiments, only two cameras were utilized (0° & 15°); the first experiments were performed to characterize whether the heating or cooling process had a significant influence on the outcome. Table 6 contains the characteristic TLC temperatures obtained by averaging of all the observed pixels.

Table 6: Peak intensity temperatures on first day

Angle of Incidence	Heating Experiment			Cooling Experiment		
	Red (ºC)	Green (ºC)	Blue (ºC)	Red (ºC)	Green (ºC)	Blue (ºC)
0°	34.34	34.64	35.90	34.29	34.64	35.96
15°	34.31	34.61	35.73	34.27	34.61	35.76

The temperatures at peak intensities of Test 1, for the experiment heating experiment and the cooling experiment in Table 6, had a maximum difference between a heating and cooling processes for the red, green, and blue signals of 0.05 ºC, 0 ºC, and 0.06 ºC respectively. The blue signal, whose profile has the broadest width, had the greatest deviation between the process types.

Replicability

The calibration experiment was repeated on the next consecutive day. However, on the second day of calibration experiments, the remaining two cameras were installed (at 30° and 45°). The results for calibration conducted on the second day with all four cameras installed are contained in Table 7.

Table 7: Peak intensity temperatures on second day

Angle of Incidence	Heating Experiment			Cooling Experiment		
	Red (ºC)	Green (ºC)	Blue (ºC)	Red (ºC)	Green (ºC)	Blue (ºC)
0°	34.36	34.69	36.01	34.31	34.66	36.12
15°	34.35	34.66	35.85	34.29	34.63	36.06
30°	34.32	34.61	35.61	34.26	34.57	35.61
45°	34.28	34.54	35.34	34.20	34.48	35.14

The results from the second day of calibration are similar to the results from the first day. Similar characteristic temperatures were found on the second day. Like the first calibration, the second calibration also found differences in the indication temperature for heating and cooling processes. For the second day calibration the heating and cooling process differed for the red,

green, and blue signals by up to 0.08 ºC, 0.06 ºC, and 0.21 ºC respectively. It appears that the difference is not associated with the viewing angle; for a given signal (red, green, or blue) the magnitude of the shift in temperature of the peak intensities was fairly consistent.

The maximum difference in peak intensity temperatures (when comparing differences between equivalent incidence angles) for each day is 0.04 ºC, 0.05 ºC, and 0.30 ºC respectively for the red, green, and blue signals. The blue signal also had the highest difference in peak intensity temperature between the calibration conducted on the first day and second day. This comparison only included the cameras mounted at 0° and 15°, since the other two cameras were not installed on the first day of calibration.

The calibration experiment was repeated yet again on the third day. No modifications to the setup were performed after the second day. The results for calibration conducted on the third day are contained in Table 7 with similar trends to the first and second day tests.

Table 8: Peak intensity temperatures on third day

Angle of Incidence	Heating Experiment			Cooling Experiment		
	Red (ºC)	Green (ºC)	Blue (ºC)	Red (ºC)	Green (ºC)	Blue (ºC)
0°	34.38	34.68	35.88	34.36	34.66	36.10
15°	34.38	34.65	35.70	34.35	34.63	35.87
30°	34.34	34.57	35.53	34.29	34.54	35.49
45°	34.30	34.46	35.34	34.25	-	35.50

When considering all possible variations, the difference between the maximum and minimum reported temperatures across all three days, all four cameras, and heating and cooling experiments, is 0.18 °C, 0.23 °C, and 0.98 °C for the red, green, and blue signals respectively. The differences are less when considering sub categories. When separated by viewing angles, results compared from all three days and heating and cooling have a difference of 0.11 °C, 0.08 °C, and 0.36 °C for the red, green, and blue signals respectively (differences were computed for individual incidence angles and the maximum difference was taken).

Since the cameras are setup orthogonal to the test section during the transient TLC setup, the most relevant comparison is to compare only the calibrated temperatures for the 0° incidence angle. The difference between calibrations over three days for only 0° incidence is 0.09°C for the red signal and 0.05 °C for the green signal.

The most selective category is to compare only the differences for the heating experiments, which is equivalent to how the transient TLC experiment is conducted. During the color change event, the TLC surfaces increased in temperature to match the driving bulk temperature induced by the inlet air heater. When the comparison is restricted to the 0° incidence and heating process only, the maximum difference over three days is found to be 0.05 °C for the red signal and 0.05°C for the green signal. If both 0° and 15° incidence angles are considered, then the difference is 0.07 °C for the red signal and 0.05 °C for the green signal. These latter values are the most relevant to practical experiments and are recommended to be used as estimates for the replicability of the TLC indication temperature. Depending on the optical arrangement the maximum viewing angle observed by the CCD camera during a transient TLC experiment may be restricted to less than ±15°.

<u>Influence of Viewing Angle</u>

It was noticed that the peak intensity temperatures for higher incidence angle cameras was consistently lower; the indication temperatures were highest for 0° and lowest for 45°. This trend was observed for both heating and cooling processes and all calibrated data sets. The shift in indication temperature to lower temperatures with increasing incidence angle appears to be systematic and not a result of random error. Additional analysis of the optical path experienced by the light as it is modified by the liquid crystals is needed to determine the mechanism for this result. Unfortunately, this analysis of the optical path was beyond the scope of this thesis.

The maximum peak intensity temperature difference when comparing incidence angles for each signal and not differentiating between a cooling experiment or a heating experiment, over all three calibrated test runs, for the red, green, and blue signal is 0.18 ºC, 0.23 ºC, and 0.98 ºC respectively. Red and green signals have the lowest sensitivity to viewing angle effects, whereas the blue signal was most affected by different angles of incidence. For a given signal, the difference in the signal's peak intensity temperatures between incidence angles of 0º and 15º is less than that between incidence angles of 30º and 45º; the difference between 0º and 15º was less than 0.03 ºC for red and green signals. In other words, while the overall shift between 0 ° and 45 ° was 0.18 ºC for the red signal, most of the shift occurred at higher viewing angles, since the shift from 0º to15º was less than 0.03 ºC.

The dependence of the TLC indication temperature on the viewing angle may be negligible in a transient TLC setup, it depends on the particular optical arrangement. The viewing angle depends on the types of lens used and distance from the camera to the test section. Usually the CCD cameras are mounted orthogonal with respect to the test section (0°) in order to

minimize the spatial distortion caused by projective viewing of the work piece. The viewing area can be minimized by placing the cameras sufficiently far away from the test section. Although this distance is dependent on the particular focal length of the lens system, with commercially available off-the-shelf CCD equipment, a distance of less than 1 meter is often enough such that all pixels within the camera image frame are no more than ± 15 ° from the optical axis of the camera. This separation distance is highly practical and can help ensure that there are not large errors in the surface temperature measurement during a heat transfer experiment as a result of viewing angle effects.

Long Term Stability

Since thermochromic liquid crystal mixtures are used only for a few tests before being replaced, the most critical property that determines the stability of the crystals (in the context of transient heat transfer measurements) is whether a specific TLC batch can maintain its unique peak intensity temperature characteristics over long periods of time in storage. Previous work by Kakade et al. [44] has discussed some of the long term characteristics of encapsulated liquid crystal mixtures.

After the initial calibration was performed as discussed previously, TLC samples taken from the same batch were separated and stored in separate refrigerated conditions and room temperature conditions to investigate the effects of storage conditions on the liquid crystal characteristics over long periods of time. After a period of 6 months, both samples were calibrated again using the same procedures and under the same conditions.

Table 9 contains data for the batch that was refrigerated for 6 months, while Table 10 contains similar data for the sample that was stored at room temperature for 6 months.

Table 9: Refrigerated stock tested after 6 months

Angle of Incidence	Heating Experiment			Cooling Experiment		
	Red (°C)	Green (°C)	Blue (°C)	Red (°C)	Green (°C)	Blue (°C)
0°	34.42	34.72	35.94	34.42	34.72	-
15°	34.65	34.67	35.77	34.41	34.70	36.23
30°	34.36	34.60	34.72	34.37	34.68	35.78
45°	34.32	34.51	35.31	34.29	34.58	35.79

Table 10: Room temperature stock tested after 6 months

Angle of Incidence	Heating Experiment			Cooling Experiment		
	Red (°C)	Green (°C)	Blue (°C)	Red (°C)	Green (°C)	Blue (°C)
0°	34.73	35.15	35.95	34.70	35.15	35.94
15°	34.70	35.11	35.94	34.67	35.09	35.94
30°	34.67	35.05	35.94	34.64	35.04	35.94
45°	34.63	34.97	35.91	34.59	34.98	35.90

Compared to the initial calibration results from, a skew towards a higher peak intensity temperature was observed after 6 months of storage for both refrigerated and room temperature stock, though the skew was much more enhanced for the room temperature stock than the refrigerated stock.

When the liquid crystals were refrigerated, the different in temperature characteristics after 6 months are minimal; the difference is of the same magnitude as the difference resulting from calibration experiments performed on separate days. Additional experiments are needed to determine whether the liquid crystal mixtures are still stable for longer storage periods.

When the liquid crystals were stored at room temperature, accelerated changes in properties were found. Peak temperatures are still observed to be at higher temperatures (similar to the refrigerated sample), but further from initial conditions from the first day experiments than the stock that had been kept refrigerated.

Based on these results, refrigeration is recommended for storage to reduce effects of degradation. Although accelerated degradation occurs when the liquid crystals are not refrigerated, the thermal response is not dramatically altered. From practical considerations the TLC mixtures can still be used. With a new calibration, the temperature characteristics of the degraded non-refrigerated samples can also be determined and used for experiments.

<u>Summary of Calibration</u>

A narrow bandwidth TLC was calibrated using the slowly heated copper block setup. Various angles of incidence were calibrated simultaneously and found to be a minor concern. These findings suggest that the red peak intensity can also be utilized in transient TLC experiments. Characterization of the blue signal requires further investigation in future work, and might prove to be as equally useful as the red and green signals, through the use of more advanced filters, more intelligent peak finding algorithms, and better characterization from additional calibrations. If only small viewing angles are encountered in the experiment, a nominal ±0.05 °C may be used for the precision of the TLC indication. If viewing angles up to 15° are expected, then a greater ±0.07 °C and ±0.05 °C for the red and green signals may be used. When combined with the uncertainty of the temperature measurement of the copper block, the corresponding uncertainties are ±0.086 °C for 0° incidence and ±0.099 °C & ±0.086 °C for 15° incidence. If the pooled uncertainties for the red and green temperatures is desired, then the pooled result is ±0.086 °C for 0° and ±0.093 °C for 15°. These uncertainties are summarized in Table 11.

Table 11: Recommended values for TLC uncertainty

Angle of Incidence	Red (°C)	Green (°C)	Pooled (°C)
0°	0.086	0.086	0.086
45°	0.099	0.086	0.093

TRANSIENT THERMOCHROMIC LIQUID CRYSTALS TECHNIQUE

In the study of heat transfer and friction performance of various internal cooling configurations, the continuous need for more detailed information has driven numerous developments in measurement techniques. The use of liquid crystals has become one popular technique for the measurement of the local distribution of surface heat transfer. Ireland & Jones [45] discussed various ways to apply liquid crystals for heat transfer and aerodynamics research.

The standard transient technique is based on the inverse solution of the heat diffusion equation of a 1D semi-infinite solid at an initial uniform temperature suddenly exposed to a convective boundary condition. The success of the transient heat transfer technique relies on known exact and closed-form analytical solutions for the temperature evolution of the solid (at least in the forward sense). Knowledge of these analytical solutions allows the inverse calculation to be performed on short algebraic expressions, rather than solving truncated infinite series solutions or solving ordinary and partial differential equations numerically. The inverse solution of these more complicated problems is less accurate than working with closed-form solutions and also computationally expensive (by orders of magnitude). The closed-form solution of semi-infinite solids with convective boundary conditions are known for only a few cases, mainly the 1D flat plate [46-48]. The accuracy of these experimental techniques depends not only on the experimental capabilities to perform accurate measurements but also on the underlying analytical tools used to deduce the results.

The assumption of a 1D semi-infinite solid is not applicable for added surface features, such as ribs or protrusions, and is a drawback to the standard transient technique. A full 3D (or possibly only 2D) inverse method must be used in order to back-calculate the heat transfer boundary condition for these complicated features. Even though the inverse calculation may be possible in principle, in practice there are limitations to how these measurements can be performed.

The left drawing of Figure 30 depicts a test surface of an internal cooling configuration with ribs applied to only one wall. In order to measure the surface heat transfer on all surfaces of the bottom wall containing the ribs, cameras would have to be mounted at each of the observer locations depicted. The camera sensor plane and image plane are parallel for the top center and bottom observation locations but these locations are only able to capture the color response of crystals of the space in-between ribs and the top surface of the rib. The top left and top right observation locations are needed in order to capture the color response of crystals applied to the left and right surfaces of the rib. At these observation locations however, the camera sensor plane is not parallel to the image plane; in addition to correcting for the spatial distortion, a Scheimflug-type lens may also be required if the depth of field is insufficient to bring the entire rib subject into focus. Specialized lens configurations are seldom available on consumer grade cameras. Hence, to measure the color response of a single rib would already require complex setup in addition to having to solve a multi-dimensional heat conduction problem. This type of measurement is not feasible for multi-pass serpentine channels where a multitude of ribs are applied.
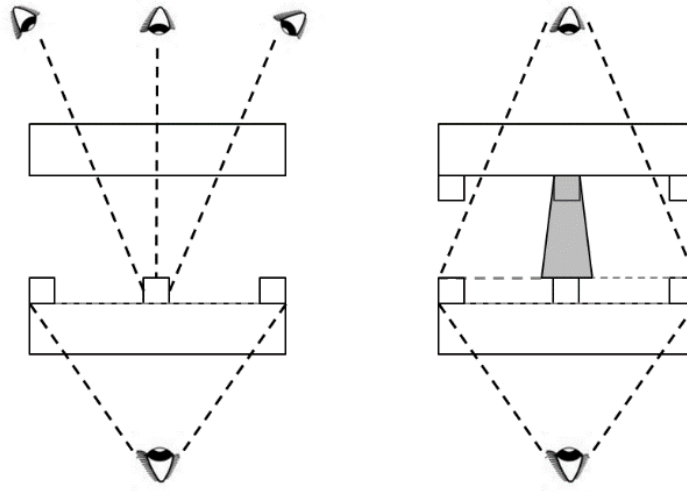
Figure 30: Observation Points in Standard Technique

Internal cooling configurations with ribs applied to only one wall can be found in gas turbine combustor liners. However, gas turbine blade internal cooling channels often have ribs on both the top and bottom walls as depicted in the right drawing of Figure 30. The presence of ribs (or possibly other features) on the top wall would distort the light rays in the shaded region and makes this measurement less feasible. The case considered so far assumes that the top surfaces are transparent. Detailed and advanced measurements of internal cooling channels often have all four channel walls coated with liquid crystals and their black backing in order to measure the heat transfer on all four walls. A cross-sectional view of such a setup used by the author is provided in Figure 31. In these channels with liquid crystals applied to all four walls, viewing from the opposite side is not possible. Because all four channel walls are coated with

TLC, the only possible arrangement for recording the color change is by viewing through the backside of the channel walls.
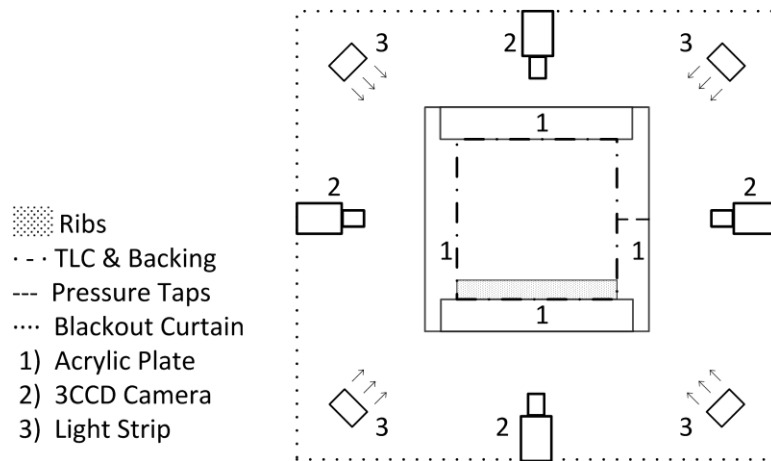
Figure 31: Cross Sectional Arrangement of Equipment

It may be argued that each channel wall can be measured separately and the results stitched together to provide the complete description and avoid the four wall setup. For long cooling passages, the bulk reference temperature is not constant along the streamwise direction. In order to account for the bulk temperature change, all participating walls must be monitored simultaneously in order to account for the bulk temperature change. Chyu et al. [49] and von Wolfersdorf et al. [50] have developed two such techniques to account for the bulk temperature change based on a transient energy balance principle. Separate measurements of individual wall performance cannot be used to correct for the bulk temperature change without additional assumptions and loss of accuracy. Hence, backside viewing is the most suitable arrangement to monitor all active portions of the channel.

Bulk Temperature Measurement

The bulk temperature is one of the parameters needed in order to back-calculate the heat transfer coefficient during a transient TLC experiment. The time evolution of the bulk temperature must be known at all locations spatially and temporally throughout the experiment in order to correctly calculate the actual surface heat transfer coefficient. The measurement of the bulk temperature is complicated by the fact that the local flow temperature changes spatially and temporally.

Jenkins et al. [51] performed measurements of the flow temperature at many locations near a 180 degree bend in a transient TLC experiment. The normalized fluid temperature was shown to be independent of the inlet temperature step and relatively independent of the channel Reynolds number. That is, the normalized temperature profile at a given flow cross-section was time-independent. Domashke et al. [52] employed a combination of the temperature fields obtained from experimental measurements and numerical simulations to determine a suitable location in the channel cross section where a thermocouple could be placed to measure the bulk temperature.

In additional to temporal changes in flow temperature, the bulk temperature may also depends on the spatial location being considered. That is because the flow loses heat to the channel surfaces during the transient heat transfer experiment, in order to heat up the test surface and cause a change in the TLC color. If the time-dependent bulk temperature can be determined, using similar techniques to Jenkins et al. and Domashke et al., techniques exist to account for the spatial change in the bulk temperature.

Chyu et al. [18] proposed a method to calculate the heat transfer coefficient first using the time-varying entrance temperature as the reference temperature and to then apply an energy balance principle to calculate both the local heat transfer coefficient based on the correct local bulk temperature. An equivalent method of accounting for the bulk temperature variation was also formulated by von Wolfersdorf et al. [19] involving less assumptions than the method by Chyu et al but is more cumbersome to implement.

HYBRID HEAT TRANSFER TECHNIQUE

The hybrid heat transfer technique was developed to overcome the drawbacks of the standard technique. In the hybrid technique, the heat transfer on the smooth non-featured portions of the channel is calculated in the same fashion as the standard technique. The hybrid technique differs in that high conductivity (metallic) features are installed so that the average heat transfer on the metallic features can be calculated using a lumped capacitance approach. The temperature of the metallic features is obtained from liquid crystals applied at the base of the feature (between the metallic feature and PMMA substrate). This arrangement allows the color response of both surfaces to be recorded simultaneously for each of the channel walls as depicted in Figure 32 for one ribbed wall and two ribbed wall configurations. In the hybrid technique, both the featured and non-featured regions are recorded simultaneously.
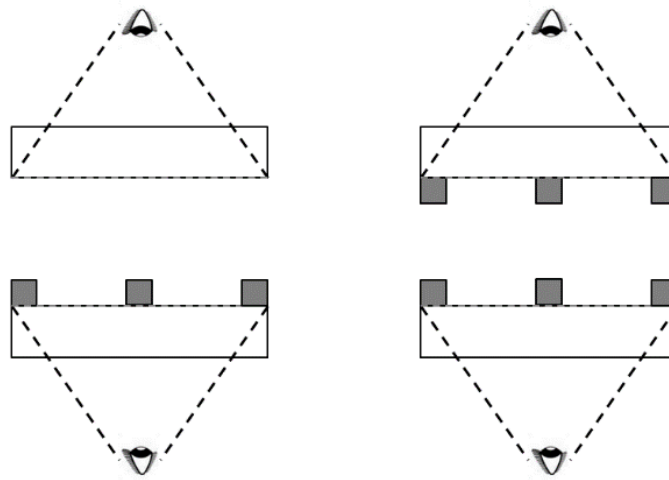
Figure 32: Observation Points for Hybrid Technique

History of the Hybrid Heat Transfer Technique

The hybrid heat transfer technique based on the transient thermochromic liquid crystal technique was presumably first employed in 2006 by Chen et al. [53] and Cunha and Chyu [54]. Chen et al. applied the hybrid technique for measurements of heat transfer over a gas turbine blade trailing edge configuration with an internal cooling channel containing an aluminum pedestal array on an acrylic substrate. In the study by Chen et al., the heat transfer coefficient on the sections not covered by pedestals was calculated with the classical lumped capacitance model. Cunha and Chyu also utilized the hybrid measurement technique in a similar study as Chen et al.

The hybrid measurement technique was also later employed in 2009 by Maurer et al. [55] to study the heat transfer enhancement in a rectangular channel with W-shaped and WW-shaped ribs for the backside cooling of gas turbine combustor liners. Maurer et al. improved on the method by Chen et al. by segmenting the lumped rib into multiple sections and applied the lumped capacitance model to the individual segments to obtain regional surface heat transfer coefficients. Maurer et al. also studied a configuration of only positive hemispheres with no ribs and used an approximate analytical solution for the one-dimensional transient heat conduction equation in a sphere to calculate the heat transfer coefficient on the hemispherical surfaces. In a similar study by Kunstmann et al [56], W-shaped, 2W-shaped, and 4W-shaped ribs were studied for channel aspect ratios of 2:1, 4:1, and 8:1. Maurer et al. and Kunstmann et al. both used an aluminum alloy as the rib material.

The hybrid measurement technique was developed independently by the author [57] and utilized to study the heat transfer enhancement in a 2:1 aspect ratio rectangular internal cooling

channel with orthogonal ribs of different rib aspect ratios. Copper ribs were attached, using double sided copper tape, onto an acrylic substrate already painted with liquid crystals.

Previous attempts at the hybrid TLC measurement technique suffered from using the incorrect analytical model (the classical lumped capacitance model). Each group of researchers assumed that the heat flux into the substrate (PMMA in all cases) was negligible due to the comparatively low thermal conductivity of PMMA. Chen et al. noted that the shaped blocks of larger characteristic size appear to be less valid in using a lumped model but restated that the Biot number calculation of the largest features was less than 0.002, and cited this condition as sufficient to use a lumped heat capacitance model. Maurer et al. used the comparative conductivity of the substrate relative to the features tested to similarly justify that the heat flux from the aluminum ribs into the Plexiglas substrate was negligible. Maurer et al. also noted the importance and necessity for the Biot number of the lumped features to be much lower than the Biot number of the base material. In utilizing the aforementioned assumption to neglect heat conduction through the substrate material, the apparent heat transfer coefficient obtained under-predicts the actual heat transfer coefficient and is a conservative estimate. The information obtained was still quite useful for designers of heat transfer surfaces (better than nothing) and these early studies were notable pioneering attempts of the hybrid technique.

Before these hybrid heat transfer experiments had been performed, a model for a lumped surface roughness was already derived in the dissertation work of Wang [58] and also published by Wang et al. [59]. This model correctly accounted for the heat conducted into the substrate material during the transient heat transfer experiment. The model was later extended by Son et al. for discrete bodies [60, 61].

106

Although the original work by Wang was not intended for a hybrid technique, the model derived could have been applied. However, these results were not widely adopted and its existence was overlooked for some time by other experimenters. An even more general improvement to the original lumped layer model by Wang and subsequent development by Son et al. is presented in this thesis.

In later chapters, it is demonstrate that the errors associated with wrongly making the assumption that the heat flux into the substrate is negligible. Analysis indicates that the error associated with the assumption of negligible heat can produce inaccurate calculations of the actual surface heat transfer coefficient. Errors resulting from the application of incorrect models in data reduction and post-processing, while these can lead to errors in the computed heat transfer coefficient, are less severe than errors introduced than measurement uncertainty. Errors from incorrect modeling assumptions are simpler post-processing errors and may be recovered, whereas experimental measurements are difficult to correct *post facto*.

The issues discussed facing the hybrid transient technique is not limited to only TLC based methods. The issues also affect techniques employing other means of measuring the surface temperature such as transient infrared thermography and transient temperature sensitive paint technique. The transient TLC method was discussed in particular, because of the history of the application of TLC for these transient tests where these issues arose and prompted further development and also because of the author's familiarity and experience with the technique.

Description of Hybrid Heat Transfer Experiment

The hybrid heat transfer experiment so far has been performed exclusively with the transient liquid crystals technique by Chen et al. [53], Cunha and Chyu [54], Maurer et al. [55, 57, 62] and the author [57, 62]. The hybrid heat transfer technique earns its denomination from the separate utilization of the two different procedures for evaluation of the heat transfer coefficient. The one-dimensional semi-infinite model is employed on regions that are not covered by surface features and the lumped capacitance model is employed on regions covered by the surface features. The hybrid technique is not limited to being performed only with liquid crystals. The hybrid technique occurred as a natural extension to experimental facilities already utilizing the TLC-based techniques. In principle the hybrid technique is compatible with virtually any surface temperature measurement such as those performed with thermocouples, infrared thermography, or by using temperature sensitive paints.

A schematic of a typical assembly for a hybrid heat transfer experiment utilizing thermochromic liquid crystals is given in Figure 33. The substrate (acrylic) is coated with the liquid crystals mixture beforehand and a black backing is then applied to improve the color contrast when viewed through the backside. Acrylic, or poly(methyl methacrylate) (PMMA), is a commonly used material for the substrate due to its attractive properties: optical transparency, low thermal conductivity, and low cost. The thickness of the substrate is chosen so that it exceeds the thermal penetration depth in order for the transient conduction to be considered semi-infinite. The thickness required can be estimated from an evaluation of the Fourier number based on plate thickness and maximum test duration, Eq. (73). A Fourier number less than 0.25 have been recommended by Wagner et al. [63].

$$Fo = \frac{\sqrt{\alpha t}}{L_c}$$
(73)

A metallic material (aluminum or copper) is often used for the surface enhancing features. The use of metals with high thermal conductivity ensures the Biot number criteria is satisfied during the experiment so that the lumped capacitance model is valid. The metallic features are adhered onto the surface via some sort of thermal adhesive. An adhesive is necessary to hold the positive disjoint features onto the surface.

During testing, the surface features experience an aerodynamic drag force as a result of the form drag and pressure drag induced by the feature. An adhesive may be necessary to hold the features onto the surface and prevent them from becoming dislocated during testing. High conductive thermal adhesives are therefore used to minimize the overall contact resistance between the feature and liquid crystals paint. Either thermal glue or double-sided metallic tape can be used to minimize the thermal resistance between the liquid crystals layer and metallic feature while providing the needed adhesive strength. Thermal paste may also be also be used, although the adhesive strength of thermal pastes are typically low.

1) Ribs
2) Adhesive
3) Black Backing
4) Liquid Crystals Layer
5) Acrylic Plate
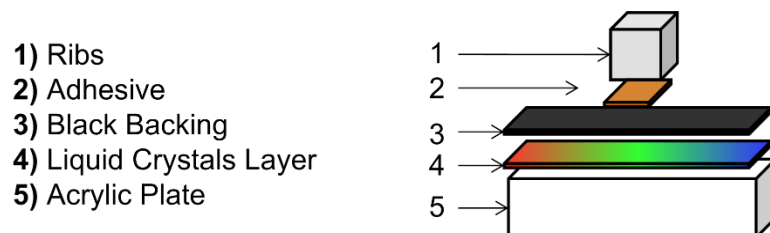
Figure 33: Assembly for hybrid heat transfer experiment

The classical 1-D semi-infinite model is invoked on regions not covered by the metal features. In regions covered by the metal features, the classical lumped capacitance model is used instead and the regionally averaged surface heat transfer coefficient is obtained. It should be stated here that the classical lumped capacitance model implicitly assumes that the heat conduction occurring between the lumped solid and the plastic substrate is negligible. As mentioned, this assumption is found to be incorrect and a new model which takes into account this effect is proposed for use instead of the classical lumped capacitance model in future hybrid heat transfer experiments.

Material Properties

Unlike metals such as aluminum or copper, the thermal properties of the PMMA substrate from commercial vendors can vary as much as 20% and cannot be considered to be known beforehand. The thermal properties of material samples of the stock materials used in the current setup were measured directly using a transient plane source technique out-of-house, the measured properties are listed in Table 12. Typical properties of Rohacell are also provided for comparison. Rohacell is a closed-cell porous foam material with low thermal conductivity and is commonly used an as insulator in heat transfer experiments.

Table 12: Measured thermal properties.

	Thermal Conductivity $\left(\dfrac{W}{m \cdot K}\right)$	Thermal Diffusivity $\left(\dfrac{mm^2}{s}\right)$	Volumetric Heat Capacity $\left(\dfrac{MJ}{m^3 \cdot K}\right)$
PMMA	0.2033 ± 0.0011	0.1235 ± 0.0022	1.646 ± 0.0222
Al 6061-T6	177.10 ± 1.39	75.14 ± 0.58	2.357 ± 0.031
Rohacell	0.041	0.154	0.267

ANALYTICAL SOLUTIONS

Analytical expressions also allow for the quick computation of the solution without having to solve the governing equation numerically. Numerical solutions are usually approximate solutions and less accurate than analytical ones. Numerical solutions to differential equations involve discretizing the governing equations (spatially and temporally). The accuracy of the solution is influenced by both the discretization scheme and number of discretization units. The solution of the discretized system is characterized by a system of (preferably linear) equations that must be solved; the size of the linear system is determined by the number of discretization units (the size of the spatial grid and number of time-steps). While the accuracy can be improved with better discretization schemes and increasing the density, it is usually at the expense of a greater computational cost (increased memory needed and time consumed for additional computations).

Even analytical expressions incur some error during their computation. At best, the numerical truncation error limits the accuracy of the computed expression to a limited number of significant digits. More important however, is the accuracy of the numerical algorithm used to compute the expressions. Even the computation of well-known functions such as trigonometric, exponential and logarithmic functions employs truncated infinite series representations in their underlying algorithms.

The determination of the temperature at a given instance in time is characterized by the direct evaluation of the analytical solution (involving only algebraic operations) or a solution of systems of equations in the case of discrete numerical solution. Because of the inherent

difference in the solution methodology, the computational expense of determining the solution numerically is always greater than compared with using analytical solutions. In practice the difference in computational time can be *several* orders of magnitude greater.

The importance of analytical solutions should not be over-glorified and practitioners should not be overly dependent on their *blind* use. The capability of analytical solutions to be evaluated much faster than the time needed to obtain numerical solutions makes them extremely attractive in implementations. In general, analytical solutions are preferred over numerical solutions because of their faster computational time. For complicated problems, the governing equations coupled with the initial conditions and boundary conditions may not have readily available closed-form analytical solutions. When analytical solutions are not already available they must be derived and implemented by new investigators. If the analytical solution is too difficult to obtain, then seeking a numerical solution is a suitable alternative at the expense of a longer wait time before the heat transfer coefficients can be solved for.

Both the analytical and numerical solutions are only as accurate as the underlying governing equation used to describe the physical problem. These governing equations are often formed based on some underlying assumptions, physical approximations, which may be violated in reality. When these assumptions are violated, the governing equations no longer completely valid and some error must be expected. Unfortunately, the governing equations themselves predates whether their solution is obtained analytically or numerically and is a much greater problem. For complicated physical processes the fundamental physics may not be completely understood.

Transient Heat Conduction

The governing equation for transient heat conduction in a solid is given by the heat equation, which can be derived from Fourier's law of heat conduction and the conservation of energy principle. Fourier's law, Eq. (74), states that heat conduction is proportion to the gradient of temperature and in the direction of decreasing temperature.

$$q_x'' = -k \frac{\partial T}{\partial x} \tag{74}$$

The transient heat conduction equation was formulated by Jean Baptiste Joseph Fourier himself [64] along with the notion of heat flux that is today known as Fourier's law of heat conduction. Fourier introduced the heat equation during a historic period when the nature of heat was still debated and not yet understood. Fourier envisioned heat transport throughout space in continuous media via heat conduction, localized heat storage because of heat capacity, and prescriptions at the boundaries that are known *a priori*.

The heat equation is derived by writing an energy balance to a differential control volume element, using a Taylor series expansion on the fluxes at the boundaries, and taking the limit as the size of the element approaches zero. The heat equation in three dimensions is thus Eq (75). The inhomogeneous term on the right hand side is the heat source, or localized heat generation term. Equation (75) can be re-written alternatively using operator notation as Equation (76).

$$\rho c \frac{\partial T}{\partial t} + \frac{\partial}{\partial x}\left(-k\frac{\partial T}{\partial x}\right) + \frac{\partial}{\partial y}\left(-k\frac{\partial T}{\partial y}\right) + \frac{\partial}{\partial z}\left(-k\frac{\partial T}{\partial z}\right) = \dot{S} \tag{75}$$

$$\rho c \frac{\partial T}{\partial t} + \nabla \cdot (-k \nabla T) = \dot{S} \tag{76}$$

Here, k is the thermal conductivity, c is the specific heat of the solid, and ρ is the mass density of the solid. An additional thermal property, the thermal diffusivity, is defined according to Eq. (77) for mathematical convenience to combine all the thermal properties in the heat equation and describe it using a single thermal property. Of these four thermal properties, only three are independent. Once any three are known, Equation (77) can be used to determine the fourth property.

$$\alpha = \frac{k}{\rho c} \tag{77}$$

In one dimension, and if no heat sources or sinks are present, the heat equation reduces to Equation (78).

$$\rho c \frac{\partial T}{\partial t} + \frac{\partial}{\partial x}\left(-k \frac{\partial T}{\partial x}\right) = 0 \tag{78}$$

If the thermal properties are constants, then the heat equation can be re-written as Equation (83). For the properties to be constant, they must be independent of time, temperature, and space. The advantage of assuming constant properties is that the partial differential equation is linear. Particular solutions to other problem types can therefore be formulated using the superposition principle.

114

$$\alpha \frac{\partial^2 T}{\partial x^2} = \frac{\partial T}{\partial t} \qquad\qquad (79)$$

Fourier applied the method of separation of variables and constructed infinite series solutions based on trigonometric series in order to solve the transient heat conduction equation in finite sized regions. Fourier would also later derived solutions based on integrals, a technique that would become the Fourier transform technique [64]. Today the transient heat conduction equation is a prototypical parabolic partial differential equation. The same method used by Fourier, separation of variables and representation of the solution using infinite trigonometric series, is now a standard technique for solving linear second order partial differential equations.

<u>Classical One-Dimensional Semi-Infinite Solid</u>

The semi-infinite solid is a useful model for many practical problems. The solid is

considered very large) and initially at a uniform initial temperature. One of the surfaces is

exposed to a new boundary condition. Because of the impulsively changed boundary condition,

the solid temperature in the solid will change until a new thermal equilibrium is reached. The

initial condition is given by Eq. (81) and the interior condition by Eq. (82). The initial

condition is a prescription of the initial temperature distribution in the solid at the start of the

problem. The interior condition is a statement that the domain is so large that the temperature at

the unexposed interior remains at the initial temperature. The exposed surface with the non-

trivial boundary conditions dictates the temperature evolution within the solid (hence the solid is

semi-infinite).

$$\alpha \frac{\partial^2 T}{\partial x^2} = \frac{\partial T}{\partial t} \tag{80}$$

$$T(x, t = 0) = T_i \tag{81}$$

$$T(x \rightarrow \infty, t) = T_i \tag{82}$$

To assist in dealing with non-homogeneous boundary or initial conditions, θ is often

defined by subtracting a reference temperature, Equation (83). Subtracting the initial

temperature is the one chosen, subtracting the convection temperature is another option.

$$\theta = T - T_i \tag{83}$$

The derivative of the new scaled temperature as it turns out, is equal to the derivative of the original unscaled temperature, Eq. (84)

$$\frac{\partial \theta}{\partial x} = \frac{\partial}{\partial x}(T - T_i) = \frac{\partial T}{\partial x} \tag{84}$$

The transient heat conduction equation in terms of the scaled temperature therefore, is the same as the original heat equation but with the unscaled temperature replaced by the scaled temperature, Equation (85). The benefit of using the scaled temperature is the convenience in the expression of the boundary conditions, which become homogeneous in terms of the scaled temperature. The initial condition using the scaled temperature is given by Eq. (86), and the interior condition is given by Eq. (87).

$$\alpha \frac{\partial^2 \theta}{\partial x^2} = \frac{\partial \theta}{\partial t} \tag{85}$$

$$\theta(x, t = 0) = 0 \tag{86}$$

$$\theta(x \to \infty, t) = 0 \tag{87}$$

The transient heat conduction equation in a one-dimensional semi-infinite solid can be solved analytically in closed-form for select cases of the surface boundary condition. The solution to the Dirichlet, Neumann, and Robin type boundary conditions are considered canonical and are often included in texts on transient heat conduction (see *Fundamentals of Heat and Mass Transfer* by Incropera and Dewitt [48], *Heat Transfer* by Adrian Bejan [46], and *Conduction of Heat in Solids* by Carslaw and Jaeger [47]).

Type 1–Applied Surface Temperature

The Type 1 boundary condition occurs when the surface temperature is suddenly forced to a different temperature and held there. The solution to the Type 1 boundary condition is given by Eq. (89) in terms of the complementary Gaussian error function. The instantaneous heat flux that occurs on the surface is not constant but varies with time according to Eq. (90), which can be derived by taking the gradient of the surface temperature and applying Fourier's law.

$$T(0, t = 0) = T_s \qquad (88)$$

$$\frac{T(x,t) - T_i}{T_\infty - T_i} = erfc\left(\frac{x}{2\sqrt{\alpha t}}\right) \qquad (89)$$

$$q_s''(t) = \frac{k(T_s - T_i)}{\sqrt{\pi \alpha t}} \qquad (90)$$

Type 2–Applied Surface Heat Flux

The second type of boundary condition occurs when the surface is subject to a constant heat flux, Eq. (91). This type of boundary condition is easy to achieve in reality by attaching a thin electric heater or cooling pad to an object' surface. Joule heating in the heater will provide a constant heat source if the electric current is regulated. If the heater is small enough that its temperature responds quickly to the temperature of the object, then the influence of the heater will be negligible and a constant supplied surface heat flux is closely approximated. The solution to the transient heat conduction equation for the applied surface heat flux is given by Eq. (92). Since the heat flux is known *a priori*, Fourier's law does not need to be applied to determine the instantaneous heat flux.

$$-k \frac{\partial T}{\partial x}\bigg|_{x=0} = q_s'' \tag{91}$$

$$T(x,t) - T_i = \frac{2q_s'' \sqrt{\frac{\alpha t}{\pi}}}{k} exp\left(-\frac{x^2}{4\alpha t}\right) - \frac{q_s'' x}{k} erfc\left(\frac{x}{2\sqrt{\alpha t}}\right) \tag{92}$$

Type 3–Convection (Radiation)

The third type of boundary condition is the convective boundary condition or radiation boundary condition [47]. This type is characterized by a surface heat flux determined from Newton's law of cooling, Eq. (93). The solution to the heat equation with the convective boundary is given by Eq. (94). The instantaneous surface heat flux can be obtained by applying Newton's law of cooling to the surface temperature solution (setting x=0).

$$-k \frac{\partial T}{\partial x}\bigg|_{x=0} = h(T_\infty - T) \qquad (93)$$

$$\frac{T(x,t) - T_i}{T_\infty - T_i} = erfc\left(\frac{x}{2\sqrt{\alpha t}}\right) - exp\left(+\frac{h^2\alpha(t-\tau)}{k^2}\right)erfc\left(+\frac{h\sqrt{\alpha(t-\tau)}}{k}\right) \qquad (94)$$

Equation (94) is attributed to the 1959 text by Carslaw and Jaeger [47]. The convective boundary condition is more popular in the field of engineering because it is more commonly encountered. Many situations arise where a solid may encounter a fluid and therefore by exposed to convection, or exchanging electromagnetic radiation with its surroundings. On the other hand, the solution to convective boundary condition case involves less popular and non-standard techniques. The first two types, solvable with standard techniques were available much earlier historically and are more well-known than the third type.

Time-Dependent Boundary Conditions

In practice, an ideal step-change or impulsive change in the boundary condition is difficult to achieve and unrealistic. Instead, the change in the boundary condition must be considered to be time-dependent. For constant thermal properties, the unsteady heat conduction equation is linear. By exploiting the linear property of the heat equation, Duhamel's superposition theorem can be applied. The linear property allows the solution of the heat equation to the time-dependent boundary condition to be constructed using the solution of the time-independent boundary condition and knowledge of the time-dependent boundary condition. Since the boundary conditions should be known beforehand, the temporal evolution of the boundary condition must also be known (i.e. the function that expresses the time-dependence is known). If this condition is met then the solution to the time-dependent boundary condition is obtained by taking the convolution of the corresponding problem with time-independent boundary conditions with the time derivative of the time-dependent boundary condition.

The solution to the time-dependent surface temperature is given by Eq. (95), which is a convolution of the solution to the perfect step-change with the time derivative of the surface temperature.

$$T(x,t) - T_i = \int_0^t erfc\left(\frac{x}{\sqrt{4\alpha(t-\tau)}}\right)\frac{\partial T_s}{\partial \tau}d\tau \qquad (\,95\,)$$

The surface heat flux for this arbitrary time-dependent temperature boundary condition is given by Eq. (96), which is again the convolution of the heat flux for a perfect temperature step with the time derivative of the surface temperature.

$$q_s''(t) = \int_0^t \frac{k}{\sqrt{\pi\alpha(t-\tau)}} \frac{\partial T_s}{\partial \tau} d\tau \qquad (96)$$

Similarly, for the third type boundary condition, if the convection temperature is time-dependent, the temperature at a given time is given by another convolution, Eq. (97).

$$T(x,t) - T_i = \int_0^t \left[erfc\left(\frac{x}{\sqrt{4\alpha(t-\tau)}}\right) \right.$$

$$\left. - exp\left(+\frac{h^2\alpha(t-\tau)}{k^2}\right) erfc\left(+\frac{h\sqrt{\alpha(t-\tau)}}{k}\right) \right] \frac{\partial T_\infty}{\partial \tau} d\tau \qquad (97)$$

Classical Lumped Capacitance Model

The classical lumped capacitance model offers a powerful and useful simplification to transient heat conduction problems. In the lumped capacitance model, the temperature distribution is considered to be spatially uniform at each instant during the transient process. The result is that all variables are limited to only dependence in time. The assumption of a uniform temperature in the lumped capacitance model is satisfied if gradients in temperature are negligible in the substance. For a non-trivial process, temperature gradients are guaranteed to be zero only if the thermal conductivity of the substance is infinite. The condition that temperature gradients be negligible can be closely approximated if the resistance to heat transfer within the solid is much less than the resistance to heat transfer to the surroundings.

The Biot number, Equation (98), is a non-dimensional number defined as the ratio of convection heat transfer rate to the rate of conduction heat transfer within the interior of the solid. The Biot number can also be thought of as the ratio of conduction heat resistance to convection heat resistance. The characteristic length, L_c is a length scale for the conduction process. For thin walls, the characteristic length is taken to be the wall thickness. For more complex configurations or geometry the characteristic length may be estimated as the ratio of the solid volume to its convective surface area.

$$Bi = \frac{hL_c}{k_{solid}}$$

(98)

Note that the Biot number is zero if the conductivity is infinite, the case when the either the heat transfer coefficient or the characteristic length is zero is the trivial case. In principle, when $Bi \ll 1$ the temperature gradients will be negligible. In practice, $Bi < 0.1$ is considered sufficient for errors in using the lumped capacitance model to be small [48].

A lumped solid suddenly exposed to external convection is an initial value problem. An energy balance applied to the lumped solid yields Equation (99), the governing equation, which is paired with the initial condition, Equation (100).

$$hA_s(T_\infty - T) = \rho V c \frac{dT}{dt} \tag{99}$$

$$T(t = 0) = T_i \tag{100}$$

The solution to Equation (99) can be obtained by the separation of variables method. Taking the natural logarithm of both sides yields a form that can be integrated directly, and manipulated using algebra into Equation (101). An alternative approach is to use an integrating factor and integrating, which will arrive at the same result in the same number of steps. The initial condition, Equation (100), is needed to determine the value of the constant of integration. Equation (101) is sometimes expressed in terms of an excess temperature such as in Eq. (102).

$$\frac{T(t) - T_i}{T_\infty - T_i} = 1 - exp\left(-\frac{hA_s}{\rho V c}t\right) \tag{101}$$

$$\frac{\theta(t)}{\theta_\infty} = 1 - exp\left(-\frac{hA_s}{\rho V c}t\right) \tag{102}$$

Enhanced Lumped Capacitance Model

The classical lumped capacitance model is appropriate for an isolated solid where the only heat exchange is by the convective condition. During a hybrid heat transfer experiment, the lumped solid exchanges heat with through convection with the fluid as well as conduction into the substrate material (an optically transparent thermoplastic). It is therefore inappropriate to use the classical lumped capacitance model to back-calculate the heat transfer coefficient during a hybrid heat transfer experiment; the forced use of the classical lumped capacitance model in these hybrid experiments will incur some modelling error. An accurate governing equation should include the conduction heat loss into the substrate material, such as Equation (103).

$$hA_s(T_\infty - T) - q''A = \rho V c \frac{dT}{dt} \qquad (\text{103})$$

It is implied that the conduction heat flux is uniform over the area. No additional assumptions are yet made concerning the nature of the heat exchange. The classical lumped capacitance model can be considered a special case of the enhanced lumped capacitance model for no conduction heat loss.

Derivation of Exact solution

The Laplace transform is an integral transform technique closely related to the Fourier transform. Both the Laplace transform and Fourier transform operations are linear operators. The Laplace operator transforms differentiation and integration in the real, time domain (the physical domain) into multiplication and division in the complex, frequency domain (the Laplace domain or s-domain). Instead of operating on the time domain, the Fourier transform operates on the spatial domains. The Laplace transform effectively turns differential equations in time domain into algebraic polynomial equations in frequency domain. Likewise the Fourier transform turns differential equations in spatial domain into algebraic equations in the spectral domain. The polynomial equations can then be easily solved in the frequency domain using algebraic techniques, probably the most significant advantage of the Laplace and Fourier transform techniques. The solution is then obtained by applying an inverse transform. When applied to partial differential equations (with time-space variables), the Laplace and Fourier transforms the differential operator in one variable (time/space) into an algebraic operator, and turns the partial differential equation into an ordinary differential equation in the non-transformed variable. The disadvantage of the Laplace and Fourier transform techniques is that the initial integral transform and inversion may be difficult to obtain, particularly the inversion.

The governing equation, which itself was derived by applying an energy balance to the control volume consisting of the lumped solid, for the enhanced lumped capacitance model is given by Eq. (104).

$$hA_s(T_\infty - T) - q''A = \rho Vc\frac{dT}{dt} \qquad (\text{104})$$

Take q'' to be the heat flux on the surface of a 1D semi-infinite solid of the Dirichlet type:

$$q'' = \int_0^t \frac{k\frac{\partial T}{\partial \tau}}{\sqrt{\pi\alpha(t - \tau)}}d\tau \qquad (\text{105})$$

Equations (104) and (105) form a coupled set of ordinary differential equations that must be solved together; Equation (104) describes the dynamics of the lumped solid region, whereas Equation (105) describes the dynamics semi-infinite solid region. The two regions are distinct and hence have distinct equations governing their dynamics. The two regions interact through an interface, which describes the nature of the coupling and interaction between the two regions.

Substitute the expression for q'' into the governing equation. Because of this substitution, it is implicitly assumed that the surface temperature of the semi-infinite solid is exactly equal to the lumped solid. The justification for the direct substitution is that the energy leaving the lumped solid is equal to the energy entering the semi-infinite substrate. The interface matching

principle for this case is one of perfect thermal contact between the lumped solid and semi-infinite substrate.

$$hA_s(T_\infty - T) - \int_0^t \frac{Ak \frac{\partial T}{\partial \tau}}{\sqrt{\pi\alpha(t-\tau)}} d\tau = \rho V c \frac{dT}{dt} \qquad (\ 106\ )$$

Equation (106) has been derived before by Sébastien Kunstmann in his dissertation work [65]. In the dissertation, it is referred to as the enhanced lumped capacitance model (ELC) to distinguish it from the classical lumped capacitance model (CLC). Kunstmann used this enhanced model to analyze the error in calculating the heat transfer coefficients using the classical model. Kunstmann used the same matching principle that is proposed here, perfect thermal contact. Unfortunately, Kunstmann chose to evaluate the model numerically (using an ODE solver) and did not derive its analytical solution. Because the analytical solution was not available, Kunstmann used the enhanced model only for error analysis and did not pursue it further as a replacement to the classical model to be used in the experiment.

We proceed to solve Eq. (106) using the Laplace transform technique. Note that the Laplace transform of a convolution of two functions is equivalent to the product of the Laplace transforms of the individual functions: We will exploit this property of the Laplace transform of convolutions of functions since we notice or recall that the heat loss term substituted into the original governing equation was the convolution of the lumped solid temperature with the heat flux into a one-dimensional semi-infinite substrate with time-dependent surface temperature.

$$\mathcal{L}\left\{\int_0^t \frac{Ak\frac{\partial T}{\partial \tau}}{\sqrt{\pi\alpha(t-\tau)}}d\tau\right\} = \mathcal{L}\left\{\frac{\partial T}{\partial \tau}\right\}\mathcal{L}\left\{\frac{Ak}{\sqrt{\pi\alpha t}}\right\} \qquad (107)$$

Take the Laplace transform of both sides of the governing equation:

$$\mathcal{L}\left\{hA_s(T_\infty - T) - \int_0^t \frac{Ak\frac{\partial T}{\partial \tau}}{\sqrt{\pi\alpha(t-\tau)}}d\tau\right\} = \mathcal{L}\left\{\rho Vc\frac{dT}{dt}\right\} \qquad (108)$$

$$\mathcal{L}\{hA_s(T_\infty - T)\} - \mathcal{L}\left\{\int_0^t \frac{Ak\frac{\partial T}{\partial \tau}}{\sqrt{\pi\alpha(t-\tau)}}d\tau\right\} = \mathcal{L}\left\{\rho Vc\frac{dT}{dt}\right\} \qquad (109)$$

$$\mathcal{L}\{hA_s(T_\infty - T)\} - \mathcal{L}\left\{\frac{\partial T}{\partial \tau}\right\}\mathcal{L}\left\{\frac{Ak}{\sqrt{\pi\alpha t}}\right\} = \mathcal{L}\left\{\rho Vc\frac{dT}{dt}\right\} \qquad (110)$$

$$hA_s\big(T_\infty(s) - T(s)\big) - \frac{Ak}{\sqrt{\pi\alpha}}\sqrt{\frac{\pi}{s}}(sT(s) - T(0)) = \rho Vc(sT(s) - T(0)) \qquad (111)$$

$$T(s)\left(hA_s + \frac{Ak}{\sqrt{\alpha}}\sqrt{s} + \rho Vcs\right) = hA_sT_\infty(s) \qquad (112)$$

$$T(s) = T_\infty(s) \frac{hA_s}{hA_s + \dfrac{Ak}{\sqrt{\alpha}}\sqrt{s} + \rho V c s} \qquad (113)$$

$$T(s) = T_\infty(s) \frac{\dfrac{hA_s}{\rho V c}}{\dfrac{hA_s}{\rho V c} + \dfrac{Ak}{\rho V c \sqrt{\alpha}}\sqrt{s} + s} \qquad (114)$$

The denominator in Eq. (114) can be factored, Eq. (115), and split by using the partial

fractions given in Eq. (116)

$$\left(\sqrt{s} + \frac{Ak}{2\rho V c\sqrt{\alpha}} + \sqrt{\left(\frac{Ak}{2\rho V c\sqrt{\alpha}}\right)^2 - \frac{hA_s}{\rho V c}}\right)\left(\sqrt{s} + \frac{Ak}{2\rho V c\sqrt{\alpha}} - \sqrt{\left(\frac{Ak}{2\rho V c\sqrt{\alpha}}\right)^2 - \frac{hA_s}{\rho V c}}\right) \quad (115)$$

$$\frac{1}{x^2 - y^2} = \frac{1}{(x+y)(x-y)} = \frac{\dfrac{1}{2y}}{x-y} - \frac{\dfrac{1}{2y}}{x+y} \qquad (116)$$

Introduce four new variables, which are groupings of existing variables. Equation (117)

defines a new parameter describing the time-scale of the heat conduction rate into the substrate.

Equation (118) is the time-constant from the classical lumped capacitance model. Equation (

119) and Eq. (120) form a conjugate pair of these two groupings.

$$a = -\frac{Ak}{2\rho Vc\sqrt{\alpha}} \tag{117}$$

$$b = \frac{hA_s}{\rho Vc} \tag{118}$$

$$\xi_1 = a + \sqrt{a^2 - b} \tag{119}$$

$$\xi_2 = a - \sqrt{a^2 - b} \tag{120}$$

$$-\xi_1 = -a - \sqrt{a^2 - b} \tag{121}$$

$$-\xi_2 = -a + \sqrt{a^2 - b} \tag{122}$$

$$\xi_1 - \xi_2 = 2\sqrt{a^2 - b} \tag{123}$$

A needed inverse Laplace transform for the two terms split using partial fractions is provided by Equation (124) and (125). Substituting the newly introduced variables and performing the inverse Laplace transform on Equation (114) into time domain results in Equation (126). The convective driving temperature is considered time-independent.

$$\mathcal{L}_s^{-1}\left\{\frac{1}{\sqrt{s} - \xi_1}\right\} = \frac{1}{\sqrt{\pi t}} + \xi_1 exp(\xi_1^2 t) erfc\left(-\xi_1\sqrt{t}\right) \tag{124}$$

$$\mathcal{L}_s^{-1}\left\{\frac{1}{\sqrt{s} - \xi_2}\right\} = \frac{1}{\sqrt{\pi t}} + \xi_2 exp(\xi_2^2 t) erfc\left(-\xi_2\sqrt{t}\right) \tag{125}$$

131

$$\frac{T(t) - T_i}{T_\infty - T_i} = \frac{hA_s}{\rho V c} \int_0^t \frac{\xi_1}{\xi_1 - \xi_2} exp\big(\xi_1^2(t - \tau)\big) erfc\big(-\xi_1\sqrt{t - \tau}\big) d\tau$$

$$- \frac{hA_s}{\rho V c} \int_0^t \frac{\xi_2}{\xi_1 - \xi_2} exp\big(\xi_2^2(t - \tau)\big) erfc\big(-\xi_2\sqrt{t - \tau}\big) d\tau \qquad (\,126\,)$$

Equation (126) can be further simplified via direct integration. The indefinite integral is given by Equation (127) with the two definite integrals given by Eq. (128) and Eq. (129).

$$\int \xi_1 exp\big(\xi_1^2(t - \tau)\big) erfc\big(-\xi_1\sqrt{t - \tau}\big) \, d\tau$$

$$= \frac{2\sqrt{t - \tau}}{\pi} - \frac{exp\big(\xi_1^2(t - \tau)\big) erfc\big(-\xi_1\sqrt{t - \tau}\big)}{\xi_1} \qquad (\,127\,)$$

$$\int_0^t \xi_1 exp\big(\xi_1^2(t - \tau)\big) erfc\big(-\xi_1\sqrt{t - \tau}\big) d\tau = -\frac{2\sqrt{t}}{\pi} - \frac{1 - exp\big(\xi_1^2(t)\big) erfc\big(-\xi_1\sqrt{t}\big)}{\xi_1} \qquad (\,128\,)$$

$$\int_0^t \xi_2 exp\big(\xi_2^2(t - \tau)\big) erfc\big(-\xi_1\sqrt{t - \tau}\big) d\tau = -\frac{2\sqrt{t}}{\pi} - \frac{1 - exp\big(\xi_2^2(t)\big) erfc\big(-\xi_2\sqrt{t}\big)}{\xi_2} \qquad (\,129\,)$$

After some manipulation, using Eq. (130) we arrive at Eq. (131).

$$-\frac{1 - exp\big(\xi_1^2(t)\big) erfc\big(-\xi_1\sqrt{t}\big)}{\xi_1(\xi_1 - \xi_2)} + -\frac{1 - exp\big(\xi_2^2(t)\big) erfc\big(-\xi_2\sqrt{t}\big)}{\xi_2(\xi_1 - \xi_2)} \qquad (\,130\,)$$

$$\frac{T(t) - T_i}{T_\infty - T_i} = \frac{hA_s}{\rho Vc} \frac{\xi_1}{\xi_1 \xi_2 (\xi_1 - \xi_2)} \left(1 - exp(\xi_2^2 t) erfc(-\xi_2 \sqrt{t})\right)$$

$$- \frac{hA_s}{\rho Vc} \frac{\xi_2}{\xi_1 \xi_2 (\xi_1 - \xi_2)} \left(1 - exp(\xi_1^2 t) erfc(-\xi_1 \sqrt{t})\right)$$

(131)

Equation (132) is used to simplify the expression further into Eq. (133)

$$\xi_1 \xi_2 = \left(a + \sqrt{a^2 - b}\right)\left(a - \sqrt{a^2 - b}\right) = a^2 - (a^2 - b) = b = \frac{hA_s}{\rho Vc}$$

(132)

$$\frac{T(t) - T_i}{T_\infty - T_i} = \frac{\xi_1}{\xi_1 - \xi_2} \left(1 - exp(\xi_2^2 (t)) erfc(-\xi_2 \sqrt{t})\right)$$

$$- \frac{\xi_2}{\xi_1 - \xi_2} \left(1 - exp(\xi_1^2 (t)) erfc(-\xi_1 \sqrt{t})\right)$$

(133)

Equation (133) is an exact, closed form, analytical solution to the enhanced lumped

capacitance model for the case of perfect thermal contact Equation (106). An expression such

as Equation (133) is of paramount important to techniques such as the hybrid heat transfer

technique which relies on the inverse solution of the transient thermal response to back-calculate

the convection heat transfer coefficient. The fundamental assumptions of this model are:

1. There is no spatial variation of temperature within the lumped solid

2. The conduction within the semi-infinite substrate is one-dimensional

3. There is perfect thermal contact between the lumped solid and substrate

4. Thermal properties are constant

Closed-form expressions allow the solution to be computed from a finite number of well-known functions. If the functions are particularly well-known, their computation can be performed using well established algorithms and function libraries and are more likely to be accurate, fast, & efficient.

The arguments of the complementary error function in Equation (133) is in general a complex number. The arguments are real if Eq. is true (i.e. if $a^2 \geq b$), otherwise the arguments are complex.

$$A\rho_s c_s k_s \geq 4hA_s \rho V c \qquad (\,134\,)$$

To evaluate Equation (133) numerically, appropriate function libraries are needed for the complex extension to the real error function. The complex extension is not as commonly encountered as the real error function. A popular programming environment for post-processing data in transient thermochromic liquid crystal experiments is MATLAB. As of MATLAB R2014a, the pre-packaged function libraries does not support the complex error function. However, numerous unofficial implementations to compute the complex error function exist. Weideman has demonstrated a routine to compute the complex error function with as few as 8 lines of MATLAB code [66]. The MATLAB implementation by Marcel Leutenegger [67] is a more updated routine preferred by the author. The routine by Leutenegger overloads the default MATLAB error function for real-valued numbers with a version that is 5-6x faster while also extending it to complex-valued numbers.

The two pre-factors or coefficients: Equations (135) and (136) play an important role in the dynamic response of the system. Particular values of these two coefficients will determine whether the behavior of the lumped solid more closely follows that of the classical lumped capacitance model (exponential growth-like behavior) or the one-dimensional semi-infinite solid model (characterized by scaled Gaussian error functions)

$$\frac{\xi_1}{\xi_1 - \xi_2} = \frac{a + \sqrt{a^2 - b}}{2\sqrt{a^2 - b}} = \frac{a}{2\sqrt{a^2 - b}} + \frac{1}{2} \qquad (135)$$

$$\frac{\xi_2}{\xi_1 - \xi_2} = \frac{a - \sqrt{a^2 - b}}{2\sqrt{a^2 - b}} = \frac{a}{2\sqrt{a^2 - b}} - \frac{1}{2} \qquad (136)$$

No Heat Capacitance

An interesting result can be obtained if we consider the limiting case when the heat capacitance of the surface feature approaches zero ($\rho Vc \rightarrow 0$). We apply this limit to the analytical solution to the enhanced lumped capacitance model. The limit of the two scaling factors is given by Eq. (137) and Eq. (138). One of the limits is zero, allowing us to skip the evaluation of the expression involving the complementary error function. The limit as the heat capacitance approaches zero for the remaining term is given by Eq. (139).

$$\lim_{\substack{\rho Vc \rightarrow 0 \\ A_s \rightarrow A}} \left(\frac{\xi_1}{\xi_1 - \xi_2} \right) = 1 \tag{137}$$

$$\lim_{\rho Vc \rightarrow 0} \left(\frac{\xi_2}{\xi_1 - \xi_2} \right) = 0 \tag{138}$$

$$\lim_{\rho Vc \rightarrow 0} (\xi_2) = \frac{Ak}{2\rho Vc\sqrt{\alpha}} - \sqrt{\left(\frac{Ak}{2\rho Vc} \right)^2 - \frac{hA_s}{\rho Vc}} = \frac{Ak - \sqrt{(Ak)^2 - hA_s 4\alpha\rho Vc}}{2\rho Vc\sqrt{\alpha}} = \frac{0}{0} \tag{139}$$

Since the limit results in an indeterminate form, l'Hôpital's rule must be used which gives the limit as Eq. (140):

$$\lim_{\rho Vc \rightarrow 0} (\xi_2) = -\frac{\dfrac{hA_s 4\alpha}{2\sqrt{(Ak)^2 - hA_s 4\alpha\rho Vc}}}{2\sqrt{\alpha}} = -\frac{hA_s\sqrt{\alpha}}{Ak} \tag{140}$$

If an additional restriction is imposed onto the limit in Equation (140) so that the exposed convective surface area is approaches the conduction heat loss area then the limit approaches the familiar parameter:

$$\lim_{\substack{\rho Vc \to 0 \\ A_s \to A}} (\xi_2) = -\frac{\dfrac{hA_s 4\alpha}{2\sqrt{(Ak)^2 - hA_s 4\alpha\rho Vc}}}{2\sqrt{\alpha}} = -\frac{h\sqrt{\alpha}}{k} \qquad (141)$$

Substitution of the limits, Equations (137), (138), and (141) into Equation (133) correctly simplifies the expression to Equation (142), a desirable result.

$$\frac{T(x,t) - T_i}{T_\infty - T_i} = 1 - exp\left(\frac{h^2 \alpha t}{k^2}\right) erfc\left(\frac{h\sqrt{\alpha t}}{k}\right) \qquad (142)$$

Equation (142) is a special case of the solution to the one-dimensional semi-infinite solid with a suddenly exposed convective boundary condition. Equation (142) is the surface solution obtained by letting x=0 in Eq. (94).

No Heat Loss, Adiabatic Contact

It was known beforehand that the classical lumped capacitance model is a special case of the enhanced lumped capacitance model (when there is no heat conducted into the substrate). The heat conducted into the semi-infinite substrate can be eliminated if the contact area is zero ($A \to 0$), the conductivity of the substrate is zero ($k_s \to 0$), or both ($Ak_s \to 0$). This limiting case is considered in this section. It is an interesting theoretical exercises to see what happens to the analytical solution to the enhanced model at this limit.

The limits of the two scaling factors are given by Eq. (143) and Eq. (144).

$$\lim_{Ak_s \to 0} \left(\frac{\xi_1}{\xi_1 - \xi_2} \right) = \lim_{A \to 0} \left(\frac{a + \sqrt{a^2 - b}}{2\sqrt{a^2 - b}} \right) = \frac{1}{2} \tag{143}$$

$$\lim_{Ak_s \to 0} \left(\frac{\xi_2}{\xi_1 - \xi_2} \right) = \lim_{A \to 0} \left(\frac{a - \sqrt{a^2 - b}}{2\sqrt{a^2 - b}} \right) = -\frac{1}{2} \tag{144}$$

The limits of the two complex parameters are given by Eq. (145)and Eq. (146)

$$\lim_{Ak_s \to 0} (\xi_1) = \sqrt{-\frac{hA_s}{\rho V c}} = i\sqrt{\frac{hA_s}{\rho V c}} = -\xi_2 \tag{145}$$

$$\lim_{Ak_s \to 0} (\xi_2) = -\sqrt{-\frac{hA_s}{\rho V c}} = -i\sqrt{\frac{hA_s}{\rho V c}} = -\xi_1 \tag{146}$$

Substitution of the first two limits into the analytical solution to the Eq. (133) gives the limiting behavior as Eq. (147), which can be simplified immediately to Eq. (148). Substitution of the latter two limits for the complex parameters gives Eq.(149).

$$\frac{T(t) - T_i}{T_\infty - T_i} = \frac{1}{2}\left(1 - exp\left(\xi_2^2(t)\right)erfc\left(-\xi_2\sqrt{t}\right)\right) + \frac{1}{2}\left(1 - exp\left(+\xi_1^2(t)\right)erfc\left(-\xi_1\sqrt{t}\right)\right) \quad (147)$$

$$\frac{T(t) - T_i}{T_\infty - T_i} = 1 - \frac{1}{2}exp\left(\xi_2^2(t)\right)erfc\left(-\xi_2\sqrt{t}\right) - \frac{1}{2}exp\left(+\xi_1^2(t)\right)erfc\left(-\xi_1\sqrt{t}\right) \quad (148)$$

$$\frac{T(t) - T_i}{T_\infty - T_i} = 1 - \frac{1}{2}exp\left(-\frac{hA_s}{\rho Vc}t\right)erfc\left(\sqrt{-\frac{hA_s}{\rho Vc}t}\right)$$

$$+ \frac{1}{2}exp\left(-\frac{hA_s}{\rho Vc}t\right)erfc\left(-\sqrt{-\frac{hA_s}{\rho Vc}t}\right) \quad (149)$$

The error function terms can be grouped together Eq. (150) by factoring.

$$\frac{T(t) - T_i}{T_\infty - T_i} = 1 - exp\left(-\frac{hA_s}{\rho Vc}t\right)\left[\frac{1}{2}erfc\left(\sqrt{-\frac{hA_s}{\rho Vc}t}\right) + \frac{1}{2}erfc\left(-\sqrt{-\frac{hA_s}{\rho Vc}t}\right)\right] \quad (150)$$

It is useful to employ the definition of the complementary error function, and the even property of the error function.

$$erfc(-z) = 1 - erf(-z) = 1 + erf(z) = 2 - erfc(z) \qquad (151)$$

Substituting the equality, Eq. (151), into Eq. (150) yields Eq. (152), which simplifies

expectedly into Eq. (153), the solution to the classical lumped capacitance model.

$$\frac{T(t) - T_i}{T_\infty - T_i} = 1 - exp\left(-\frac{hA_s}{\rho Vc}t\right)\left[\frac{1}{2}erfc\left(\sqrt{-\frac{hA_s}{\rho Vc}t}\right) + 1 - \frac{1}{2}erfc\left(\sqrt{-\frac{hA_s}{\rho Vc}t}\right)\right] \qquad (152)$$

$$\frac{T(t) - T_i}{T_\infty - T_i} = 1 - exp\left(-\frac{hA_s}{\rho Vc}t\right) \qquad (153)$$

Equation (133) may be considered as a correction to the existing solutions to the

classical lumped capacitance model or the one-dimensional semi-infinite solid. This mindset is

likely warranted considering that a heat loss term was simply inserted into the governing

equation for the lumped capacitance model. For the lumped capacitance case, Equation (133)

accounts for the heat conduction into the substrate material. For the semi-infinite solid case,

Equation (133) accounts for the delay in the surface response because of a bulk heat

capacitance on the surface. However, Equation (133) can be generalized further.

Generalization to Interior Solution

Equation (133) describes the development of the temperature of the lumped solid or the surface temperature of the substrate because it was assumed that these two temperatures were equal. Using Equation (133) as a starting point, it is possible to obtain an even more general result.

$$erf(z) = \frac{2}{\sqrt{\pi}} \int_0^x \exp(-t^2) dt \qquad (154)$$

Recall the definition of the Gaussian error function (erf(x)), Eq. (154).The derivative of the *complementary* error function is a type of Gaussian function, Eq. (155).

$$\frac{\partial}{\partial t} erfc\left(\frac{x}{2\sqrt{\alpha t}}\right) = -\frac{x}{2t^{3/2}\sqrt{\pi\alpha}} exp\left(-\frac{x^2}{4\alpha t}\right) \qquad (155)$$

The solution to the one-dimensional semi-infinite solid model with a time-dependent surface temperature is given by Eq. (156), which is a convolution of the solution to the time-independent step-change in surface temperature with the time-derivative of the imposed time-dependent surface temperature. A property of the convolution operator when applied to derivatives makes Eq. (156) equivalent to Eq. (157). The differentiation operator can be translated from one function to the other.

$$T(x,t) - T_i = \int_0^t erfc\left(\frac{x}{2\sqrt{\alpha(t-\tau)}}\right)\frac{\partial(T_s - T_i)}{\partial\tau}d\tau \qquad (156)$$

$$T(x,t) - T_i = \int_0^t \frac{\partial}{\partial\tau}erfc\left(\frac{x}{2\sqrt{\alpha(t-\tau)}}\right)(T_s - T_i)d\tau \qquad (157)$$

The derivative of the first function, given by Eq. (155) is substituted into Eq. (157), giving Eq. (158). The goal is to substitute Eq. (133) into Eq. (158). If we are able to perform the integration of Eq. (158) then we can determine the solution to the interior of the semi-infinite solid underneath the lumped solid analytically. It turns out that the integration requires lengthy manipulations.

$$T(x,t) - T_i = \int_0^t -\frac{x}{2t^{3/2}\sqrt{\pi\alpha}}exp\left(-\frac{x^2}{4\alpha t}\right)(T_s - T_i)d\tau \qquad (158)$$

As an aside, now suppose that the time-dependent surface temperature was somehow imposed by considering instead the surface temperature solution to the Type 3 boundary condition. Substituting the surface temperature solution for the Type 3 boundary condition into Eq. (158) gives Eq. (159).

$$\frac{T(x,t) - T_i}{T_\infty - T_i} = \int_0^t \frac{\partial}{\partial\tau}erfc\left(\frac{x}{2\sqrt{\alpha t}}\right)\left(1 - exp\left(\frac{h^2\alpha(t-\tau)}{k^2}\right)erfc\left(\frac{h\sqrt{\alpha(t-\tau)}}{k}\right)\right)d\tau \qquad (159)$$

It is already known beforehand, that when Eq. (159) is simplified, Eq. (160) is the result. By imposing that the surface temperature obey the Type 3 boundary condition case, we are simply considering that the problem is actually a Type 3 problem with time-independent convective boundary conditions and not actually a Type 1 problem with a time-dependent surface temperature. However, both interpretations are correct.

$$\frac{T(x,t) - T_i}{T_\infty - T_i} = erfc\left(\frac{x}{2\sqrt{\alpha t}}\right) - exp\left(\frac{hx}{k} + \frac{h^2\alpha t}{k^2}\right) erfc\left(\frac{x}{2\sqrt{\alpha t}} + \frac{h\sqrt{\alpha t}}{k}\right) \qquad (160)$$

Some algebra is used to manipulate Eq. (160) into Eq. (161).

$$\frac{T(x,t) - T_i}{T_\infty - T_i} = erfc\left(\frac{x}{2\sqrt{\alpha t}}\right) - exp\left(\frac{x}{2\sqrt{\alpha t}}\frac{2h\sqrt{\alpha t}}{k} + \frac{h^2\alpha t}{k^2}\right) erfc\left(\frac{x}{2\sqrt{\alpha t}} + \frac{h\sqrt{\alpha t}}{k}\right) \qquad (161)$$

We now consider a new parameter, Eq. (162). Equation (163) is the result when we re-write Eq. (161) using the new parameter, β. If we can find an equivalent expression for β we can solve Eq. (158) without having to perform the integration ourselves.

$$\beta = \frac{h\sqrt{\alpha t}}{k} \qquad (162)$$

$$\frac{T(x,t) - T_i}{T_\infty - T_i} = erfc\left(\frac{x}{2\sqrt{\alpha t}}\right) - exp\left(\frac{x}{2\sqrt{\alpha t}}2\beta\sqrt{t} + \beta^2 t\right) erfc\left(\frac{x}{2\sqrt{\alpha t}} + \beta\sqrt{t}\right) \qquad (163)$$

By direct comparison, it turns out that β is negative of the complex parameter ξ. By considering two such instances for β, we have Eq. (164) and Eq. (165).

The goal is to substitute Eq. (133) into Eq. (158). If we are able to perform the integration of Eq. (158) then we can determine the solution to the interior of the semi-infinite solid underneath the lumped solid analytically.

We use the result that Eq. (159) eventually leads to Eq. (160) to solve Eq. (158). The solution is given by Eq. (166)

$$\tilde{\beta}_1 = -\xi_1 \tag{164}$$

$$\tilde{\beta}_2 = -\xi_2 \tag{165}$$

$$\frac{T(x,t) - T_i}{T_\infty - T_i} = \frac{\xi_1}{\xi_1 - \xi_2}\left(erfc\left(\frac{x}{2\sqrt{\alpha t}}\right) - exp\left(-\frac{\xi_2 x}{\sqrt{\alpha}} + \xi_2^2 t\right)erfc\left(\frac{x}{2\sqrt{\alpha t}} - \xi_2\sqrt{t}\right)\right)$$
$$- \frac{\xi_2}{\xi_1 - \xi_2}\left(erfc\left(\frac{x}{2\sqrt{\alpha t}}\right) - exp\left(-\frac{\xi_1 x}{\sqrt{\alpha}} + \xi_1^2 t\right)erfc\left(\frac{x}{2\sqrt{\alpha t}} - \xi_1\sqrt{t}\right)\right) \tag{166}$$

Equation (166) bears a strong resemblance to the solution to the one-dimensional semi-infinite solid exposed to a convective boundary condition. The similarity between the two is not surprising, since the similarity was exploited in order to arrive at Equation (166). When Equation (166) is evaluated at the surface (x=0) it reduces to Equation (133). Unlike Equation (133) which only provides the surface temperature of the substrate, Equation (166) provides the temperature throughout the entire domain (all x).

Equation (133), which is a special case of Equation (166), already satisfies the classical and enhanced lumped capacitance model. It can be shown that Equation (166) is also solution to the heat diffusion equation, by substituting Equation (166) into the heat diffusion equation, taking the derivatives and simplifying to shown that both sides of the equality are the same. The fact that Equation (166) is a non-trivial solution to two different governing equations suggests that it is not simply a modification or correction to existing solutions but closer to a general solution. On the other hand, the derivation steps leading up to Equation (166) made repeated use of the convolution. Solutions to the heat diffusion equation were convoluted against the solution to the enhanced lumped capacitance model. Convolutions of solutions to the governing equations remain solutions, similar to how inhomogeneous equations can be solved be convoluting the inhomogeneity against a fundamental solution. Convoluting solutions of the two governing equations therefore unremarkably lead to Equation (133) and Equation (166) being solutions to both types of governing equations.

Additional Considerations

The classical lumped capacitance model which assumes adiabatic contact and the enhanced model which assumes perfect thermal contact are the two extreme coupling cases. In a practical scenario, where the thermal contact is not perfect, the temperature must fall somewhere between the classical and enhanced model. The classical lumped capacitance model, where there is no heat loss, predicts the fastest temperature change of the lumped body. The enhanced model, with perfect thermal contact, predicts the maximum heat loss and slowest temperature change of the lumped body. Hence, if the thermal contact is neither adiabatic nor perfect, the classical and

enhanced model can be used together to determine suitable upper and lower bounds of the error associated with the hybrid heat transfer technique.

By carefully tuning certain parameters, it is possible to reduce the difference between the predicted outcomes of the two models. The differences between the two models increases with longer testing duration or a large contact area between the lumped feature and semi-infinite substrate. The testing duration is primarily affected by the heat transfer coefficient and heat capacity of the surface feature. The heat capacitance can be altered by choosing a different material for the surface feature, though aluminum and copper are most commonly used. Aluminum has a lower heat capacity and lower cost compared to copper, and can shorten the testing time and is generally superior to copper in performance. The testing duration also depends on the driving temperature and temperature indicator used. TLC mixtures with different color play bandwidths can be selected to achieve different testing times.

Selecting a substrate material with a lower thermal conductivity and higher specific heat will also reduce the range of predictions between the classical and enhanced lumped capacitance models. However, this material will have a higher thermal diffusivity than before. For the same testing duration, a higher Fourier number will be achieved which adversely affects the validity of the semi-infinite body assumption. When the experimental technique relies on backside viewing, an optically transparent material must be used; there are few low cost alternatives to PMMA or polycarbonate for this type of technique. If backside viewing is not an issue, it may be possible to engineer or select materials with different properties, at the risk of violating the semi-infinite body assumption, though it is not recommended.

An alternative approach is to decrease the contact area between the lumped surface feature and substrate intentionally. Usually the contact area between the lumped body and semi-infinite substrate is decided by the geometry of the surfaces features tested and scaling of the setup. Ostanek et al. [68] described a technique for constructing an air gap, which limits the contact length, and also performed numerical analysis to demonstrate the benefit of the air gap. The method and analysis used by Ostanek et al. was developed for a steady state experiment in order to reduce the back-side conduction losses; however, this technique is also effective for transient heat transfer experiments. With the air gap technique, back-side viewing is still possible. The heat conducted into the substrate can be nearly eliminated by removing all but enough material to support the surface features as shown in Figure 34. Hoefler et al. [69] have similarly used a low conductivity adhesive tape combined with a fluted rib hub to ensure a nearly adiabatic rib hub.
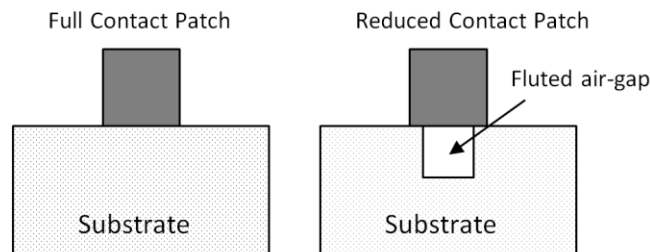
Figure 34: Air gap technique for reducing contact patch

Lumped Layer Model

The solution to the enhanced lumped capacitance model, Eq. (133), can be expressed alternatively as, Eq. (167), by algebraic manipulation.

$$\frac{T(t) - T_i}{T_\infty - T_i} = 1 - \frac{\xi_1}{\xi_1 - \xi_2} exp\left(\xi_2^2(t)\right) erfc\left(-\xi_2\sqrt{t}\right) + \frac{\xi_2}{\xi_1 - \xi_2} exp\left(\xi_1^2(t)\right) erfc\left(-\xi_1\sqrt{t}\right) \quad \text{(167)}$$

A similar expression to Eq. (167) has been presented by Wang et al. [58, 59]. The solution presented by Wang et al. is for a high conduction roughness layer. The high conduction roughness layer was modeled with a lumped capacitance approach, Figure 35, and the governing equations was proposed similar to the enhanced lumped capacitance model.
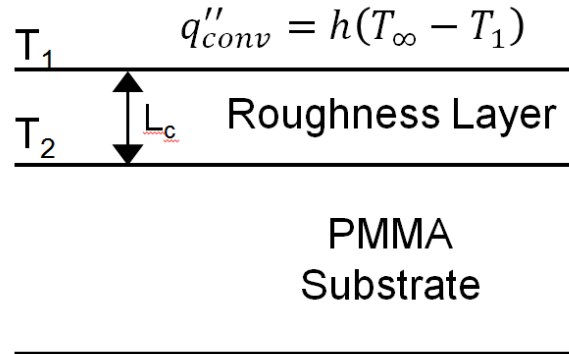
Figure 35: Lumped layer model by Wang et al. [58, 59]

According to the model proposed by Wang et al. T_1 is the temperature of the top of the roughness layer and T_2 is the base temperature of the lumped layer or the temperature of the top of the substrate. An average temperature, defined as the arithmetic average of T_1 and T_2 is defined as Equation (168).

$$\bar{T} = \frac{T_1 + T_2}{2}$$ (168)

The analysis by Wang also defined a parameter by on the heat capacitance and thermal resistance of the lumped layer, Eq. (169).

$$\beta = \rho c L_c \left(1 - \frac{hL_c}{2k} \right) = \rho c L_c \left(1 - \frac{Bi}{2} \right)$$ (169)

The problem was solved using the method of Laplace transforms. The solution is given by Eq. (170), with new definitions for the conjugate pair, Eqns. (171) and (172).

$$\frac{T(t) - T_i}{T_\infty - T_i} = 1 - h \left(\frac{exp(\xi_1^2 t)erfc(\xi_1\sqrt{t})}{\beta\xi_1(\xi_1 - \xi_2)} - \frac{exp(\xi_2^2 t)erfc(-\xi_2\sqrt{t})}{\beta\xi_2(\xi_1 - \xi_2)} \right)$$ (170)

$$\xi_1 = \frac{\sqrt{\rho_s c_s k_s}}{2\beta} \left(1 + \sqrt{1 - \frac{4\beta h}{\rho_s c_s k_s}} \right)$$ (171)

$$\xi_2 = \frac{\sqrt{\rho_s c_s k_s}}{2\beta} \left(1 - \sqrt{1 - \frac{4\beta h}{\rho_s c_s k_s}} \right)$$ (172)

The original experimental technique by Wang et al. was not a hybrid approach. The lumped layer model was applied everywhere. Son et al. [60, 61] later extended the model by Wang et al. for discrete bodies, by employing an effective thickness and incorporated it into a hybrid technique for surface protrusions instead of simple roughness.

Equation (133) is nearly identical to Equation (170) only for the special case when $A_s=A$. The difference is a result of different modeling assumptions when deriving the governing equation.

The lumped layer model takes its governing equation for a continuous roughness layer on top of the substrate material, whereas the energy balance for the enhanced lumped capacitance model was performed on a discrete surface feature.

The lumped layer model is characterized by a single characteristic length (the layer thickness) whereas the enhanced lumped capacitance model contains two lengths (one for the rate of conduction within the body and a second length for the rate of heat transfer to the substrate). The lumped layer model is not applicable to discrete bodies. The dual characteristic lengths in the enhanced lumped capacitance model can be summarized as the ratio of the lumped body volume to the convection surface area (V/As) and the ratio of the volume to the contact area (V/A). Substitution of either ratio (V/A$_s$ or V/A) as an equivalent characteristic length into the lumped layer model is insufficient. The enhanced lumped capacitance model is equivalent to the lumped layer model only for the degenerate case (when $A_s=A$). In this aspect, the enhanced lumped capacitance model is an improvement over the lumped layer model proposed by Wang et al. and the version used Son et al.

Wang et al. modeled the spatial temperature profile across the lumped layer using a quasi-steady state approach and incorporated the Biot number into the solution. This model allows for the convection surface temperature to be different than that of the base temperature of the lumped layer. The enhanced lumped capacitance model as presented so far does not take this approach, the temperature profile is assumed to be spatially uniform. In other words, the Biot number is assumed to be zero. In this regard, even if $A_s=A$, the enhanced lumped capacitance model and lumped layer model are still not identical. However, for lump-able bodies the Biot number is significantly less than unity, the difference between the predictions based on the enhanced lumped capacitance model or the lumped layer model is quite small. If the Biot number is too large, then neither the enhanced lumped capacitance model nor the lumped layer model are applicable physically. Hence the difference is important only when extreme accuracy and precision are required.

The lumped layer model has the advantage that it permits finite Biot numbers whereas the enhanced lumped capacitance model assumes that the Biot number is identically zero. The lumped layer model is better at prediction the spatial temperature profile inside the lumped body than the enhanced lumped capacitance model. On the other hand, the lumped layer model only admits a single characteristic length, whereas the enhanced lumped capacitance model accepts dual characteristic lengths and is more applicable to discrete bodies than the lumped layer model. In the near future, it is likely that the two strengths of these models can be incorporated into the same model. This model would need to allow for finite Biot numbers as in the lumped layer model while starting with the energy balance of a discrete body as in the enhanced lumped capacitance model.

Numerical Validation of Enhanced Lumped Capacitance Model

While analytical solutions may perfectly predict the outcome of a particular governing equation, the solution is only to the degree that the governing equation is an accurate representation actual processes. The enhanced lumped capacitance model is essentially zero-dimensional in the lumped solid region and one-dimensional in the semi-infinite substrate. In reality, experiments conducted are two-dimensional or three-dimensional in geometry. In addition to the geometry, the convective boundary condition is in general, inhomogeneous and non-uniform. Even on a flat surface, a non-uniform heat transfer coefficient can also give rise to multi-dimensional heat conduction as the heat from high temperature regions tends towards low temperature regions because of the differences in the convective boundary condition.

The temperature development of a two-dimensional configuration was simulated numerically using the finite volume method based solver [70] to verify the appropriateness of the enhanced lumped capacitance model for use in a hybrid heat transfer experiment. The solver used is the commercial computational fluid dynamics software package, Fluent (v15) by Ansys, Inc. A simpler two-dimensional simulation was chosen, to reduce computational costs. A two-dimensional simulation should be sufficient for analyzing multi-dimensional effects. Results obtained from the two-dimensional simulation can be generalized and applied to three-dimensional cases. A grid refinement study was also performed to quantify the sensitivity of the solution to the grid used for the simulation.

Problem Setup and Definition

The modeled domain is based on an experiment conducted by the author in which the hybrid heat transfer technique was used [62]. Ribs of square cross section were applied to a surface at a rib-pitch-to-rib-height ratio of 10. Aluminum 6061-T6 was used as the material for the rib roughness. The computational domain spans a rib half-pitch and applying symmetry boundary conditions at the mid-plane of the rib and inter-rib space. The computational domain is depicted in Figure 36. The height of the rib was 5.08 mm (0.20 in) and the substrate thickness was 12.7mm (0.50 in). The width of the computational domain is thus 25.4 mm (1.00 in). A regular Cartesian grid was generated using GridPro. The grid contains 64 cells along the rib height, which yields 2048 cells in the aluminum rib and 51,200 cells in the PMMA substrate.
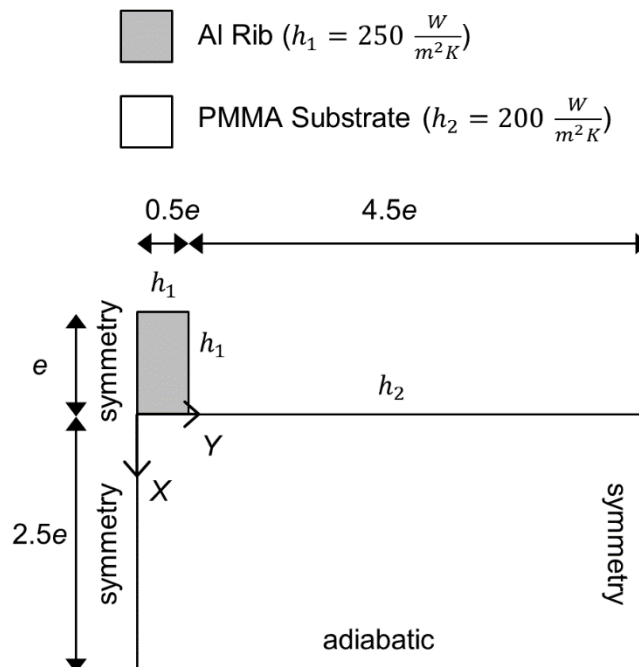

Figure 36: Computational domain

The coordinate system is also depicted in Figure 36. X is taken to be the canonical direction of the heat penetration depth (surface normal coordinate), with X=0 placed at the PMMA surface and base of the aluminum rib. Y is the spanwise or lateral direction, parallel to the surface of the substrate. Symmetry boundary conditions are applied along the Y=0 and Y=5e locations; an adiabatic boundary condition is applied to the lower X=2.5e surface corresponding to the interior boundary condition. Constant material properties are applied in each region. The thermal properties of aluminum and PMMA used in the simulation are provided in Table 13.

Table 13: Material Properties

Material	k $\left[\dfrac{W}{m \cdot K}\right]$	ρ $\left[\dfrac{kg}{m^3}\right]$	c $\left[\dfrac{J}{kg \cdot K}\right]$
Al 6061-T6	177.1	2719	866.863
PMMA	0.2033	1180	1395

The initial temperature is specified as 300 K everywhere. The convective boundary condition is applied to the exposed surface of the substrate and the two surfaces of the lumped solid. The convection temperature was set to 320 K. A uniform heat transfer coefficient was applied to each region.

On the aluminum rib, the heat transfer coefficient applied was 250 W/(m^2·K). The heat transfer coefficient applied to the PMMA substrate was 200 W/(m^2·K). These heat transfer coefficients are similar to the regionally averaged heat transfer results obtained experimentally on the same geometry and reported in [62]. The calculated Biot number, known *a priori* for this

case, is 0.0072, using the rib height as the characteristic length and heat transfer coefficient of 250 W/(m^2·K).

2nd order central differencing is used for the spatial discretization and a 2nd order backward differencing scheme is used for the temporal discretization using an implicit time-stepping scheme. The physical time-step size was 0.01 seconds, and the unsteady simulated was solved up to 60 seconds in physical time. The time-step size is comparable to experimental capabilities. Camera frame rates are usually 30 frames per second. The speed of flow temperature data acquisition for thermocouples is on the order of 100 samples per second. As long as the simulation is accurate, a time-step size of 0.01 seconds should is sufficient to capture the important dynamics. Experiments are limited in test duration because of the risk of violating the semi-infinite body assumption. The numerical simulation carries the same risk, because the interior boundary condition is approximated using an adiabatic boundary on the lower surface. Iterative convergence at each time-step before proceeding to the next time-step was considered achieved when the scaled energy residual was better than 10^{-15}, this occurred within 8 to 12 iterations. The physical temperature computed from the numerical simulation at various spatial locations and time-steps is used to compute a non-dimensional temperature, defined according to Eq. (173), which is the dynamic variable of interest for general problems. The non-dimensional temperature distribution is plotted in Figure 37 for an elapsed time of 60 seconds.

$$\theta = \frac{T - T_i}{T_\infty - T_i}$$

(173)
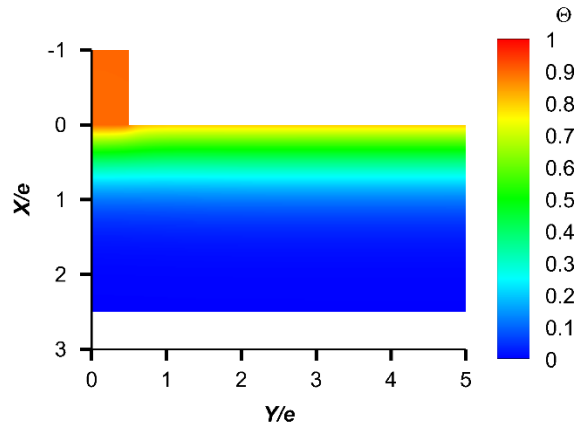
Figure 37: Temperature distribution at t = 60 s for perfect thermal contact

The take away for Figure 37 is that the temperature at the adiabatic boundary on the lower surface remains at the initial temperature, which is sufficient to verify that the semi-infinite body has not yet been violated. For longer testing duration, the thermal information will eventually reach the interior surface and the semi-infinite body assumption will no longer be valid. The choice of the ½ inch depth chosen for the simulation and experiment (½ inch thickness PMMA was used in the experiment) is therefore sufficiently thick that the semi-infinite body assumption may be used. Within the aluminum region, the temperature is nearly uniform. Except in the immediate vicinity of the aluminum rib, the subsurface temperature gradients are normal to the surface and nearly one-dimensional. Figure 37 suggests, qualitatively, that the assumptions of a lumped region for the aluminum rib, and one-dimensional semi-infinite solid model between the ribs are appropriate.

Grid Refinement Study

A grid refinement study was performed in order quantify the grid sensitivity of the numerical solution by generating two finer grids. The grid refinement study was performed only for perfect contact (no thermal resistance). The grid spacing was reduced globally by a factor of 2 and the time-step size was also reduced by a factor of 2 in order to capture the influence of both the spatial and temporal discretization schemes. A halved grid spacing corresponds to a quadrupling of the total cell count for each refinement. Hence, the medium grid was computed on a domain four times as large for twice as many time-steps compared to the base coarse grid, an 8x increase in computational cost. The computational cost of the fine grid solution is 64x the base grid. The grid sizes are summarized in Table 14. The N1 notation refers to the most dense grid, N2 the intermediate grid, and N3 the coarsest grid.

Table 14: Grid Parameters

	N1 Fine grid	N2 Medium grid	N3 Coarse grid
# Cells	128x256 + 640x1280	64x128 + 320x640	32x64 + 160x320
Δx	$\dfrac{e}{256}$	$\dfrac{e}{128}$	$\dfrac{e}{64}$
Δt	0.025 s	0.05 s	0.01 s

The convergence parameter selected was the average temperature in the aluminum region. The Grid Convergence Index (GCI) was estimated following the procedures developed by Roache [71]; a factory of safety of 1.25 was used since three grids were available. The GCI was computed by comparing values at time-steps common to all three grids. The GCI for the coarse grid (GCI_{32}) and medium grid (GCI_{21}) are plotted in Figure 38. The root-mean-square GCI of all the time steps was calculated to be 0.0313% for the GCI_{32} and 0.0175% for GCI_{21}. The asymptotic range of convergence was also computed, and found to be nearly unity for all time-steps.
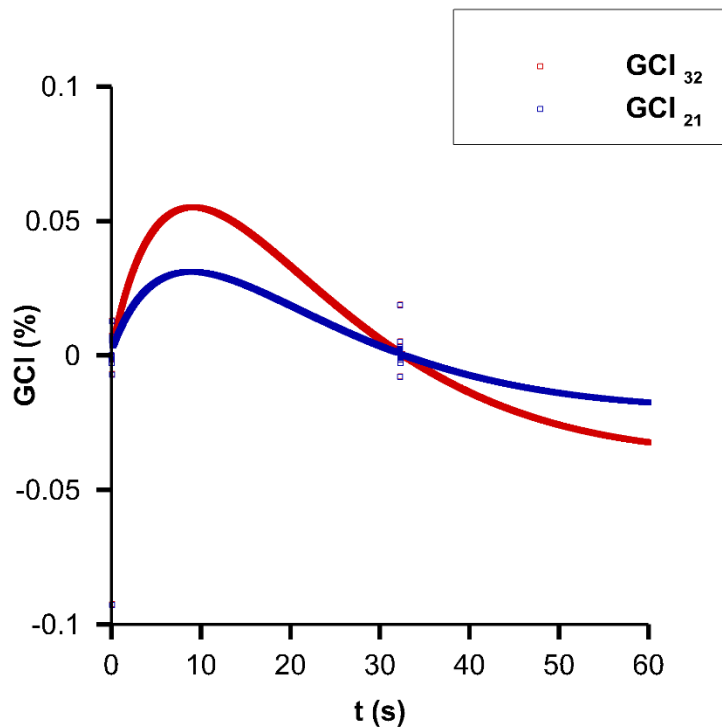

Figure 38: Grid refinement results

Modeled Contact Resistance

Fluent natively supports a thermal resistance model. A two-layer interface is always generated between adjacent zones, with one layer applied to each region. Perfect contact was simulated by setting the interface thickness to zero thickness (which is the default option). A thermal resistance may be modeled by setting the interface to a finite thickness. A pseudo steady-state heat conduction equation is solved on the interface region, resulting in behavior similar to an empirical contact resistance. The thickness of the interface was set to achieve a contact resistance of 2.75×10^{-4} m$^2 \cdot$K/w. This value is typical for aluminum surfaces in contact with air as the interfacial fluid [48]. Air as the interfacial fluid between two metal surfaces in contact is a sort of worst case estimate. The simulation with the thermal resistance was performed using the original base grid. The medium and fine grids were used only for the grid convergence study.

The non-dimensional temperature distribution of the simulation using the thermal resistance is plotted in Figure 39 after 60 seconds. Figure 39 is nearly identical to the same distribution for the perfect contact case, Figure 37, indicating that the influence of the contact resistance is minor.
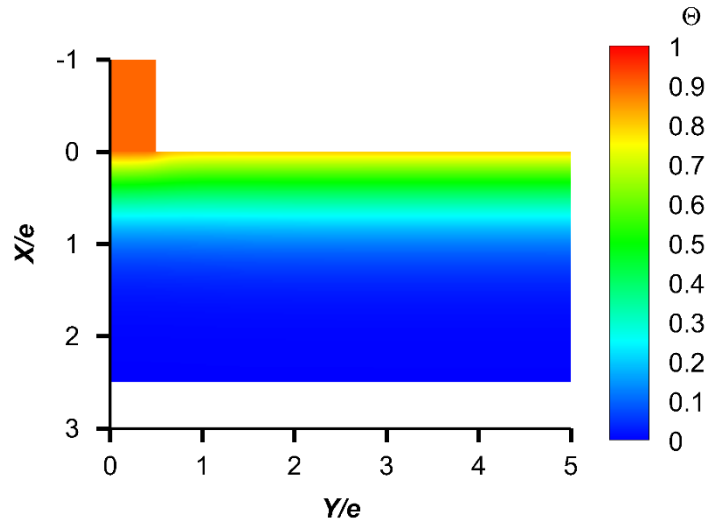
Figure 39: Temperature distribution at t = 60 s with contact resistance

The history of the average temperature in the aluminum region is plotted in Figure 40 for both the perfect contact and contact resistance simulations. The predicted temperature computed using the analytical solutions to the lumped capacitance model and enhanced lumped capacitance model are also plotted in Figure 40 for comparison. The classical lumped capacitance model is plotted with a solid line, the enhanced lumped capacitance model with a dashed line, the numerical simulation with perfect contact with a dash-dotted line, and numerical simulation with contact resistance with a dotted line.
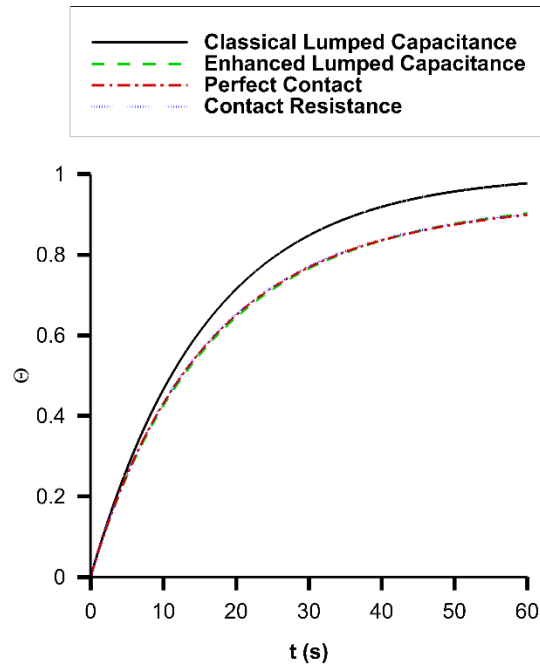
Figure 40: Evolution of lumped solid temperature

The classical and enhanced lumped capacitance models assumes there is no temperature variation in the solid. In the numerical simulation, the spatial temperature variation is solved. Hence, the temperature obtained from the numerical simulation is the actual average temperature of the aluminum rib, whereas the lumped capacitance approaches are approximations. Both simulations with and without contact resistance predict nearly the same temperature in the aluminum region, indicating that the influence of contact resistances is minor for this geometry. The classical lumped capacitance model, because it does not account for the heat conducted into the substrate, consistently over-predicts the average temperature. The enhanced lumped capacitance model is superior to the classical model in this regard, as the enhanced model predicts a temperature that is in close agreement with the numerical simulation.

161

Spatial Temperature Variation

Using the same numerical procedures, additional simulations were performed on ribs of different geometry. The purpose of the additional simulation is to determine whether a lumped approach can be applied to significantly larger sized ribs; that is, whether the assumption of a uniform temperature distribution might be violated because of insufficient conduction in a larger sized rib. A new computational grid was generated for a rib with the same rib height (e = 5.08 mm) and rib width equal to five times the rib height (w = 25.4 mm). The rib aspect ratio (RAR) of the new rib is five, whereas the original rib aspect ratio was unity. The updated grid had the same spatial resolution as the coarse (N3) grid. The wide rib configuration is motivated partly by a previous experiment by the author [72, 73]. The wide rib configuration results in a channel configuration that is 50% ribbed, which can alternatively be interpreted as a channel of smaller dimension that is 50% trenched. The thermal resistance at the interface was not applied to the wide rib, since its influence was found to be minor. The same heat transfer coefficient is applied to the wide rib as the small rib. It has been determined that the heat transfer for wider ribs is less than that of the narrower ribs at the same Reynolds number [72, 73]. The choice of using the same heat transfer coefficient for both rib sizes in the numerical simulation is a matter of convenience for comparing results of the two simulations under the same conditions, rather than trying to accurately mimic the actual process. The temperature distribution for the wide rib taken at the end of simulation is plotted in Figure 41.
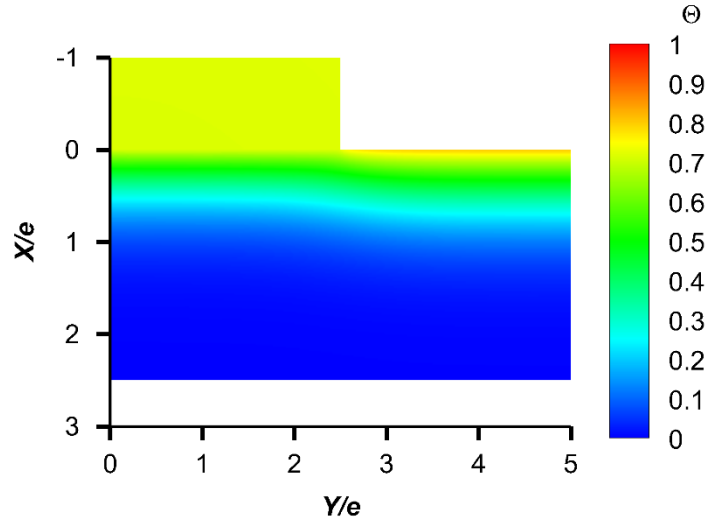
Figure 41: Temperature distribution at t = 60 s for wide rib

The scaled temperature variation considered, defined according to Eq. (174), is the difference between maximum and minimum temperature in the aluminum regions divided by the driving temperature difference. The temperature variation is computed at every time-step of the numerical simulation and plotted in Figure 42 for both the original RAR = 1 rib and RAR = 5 rib.

$$\Theta^* = \frac{T_{max} - T_{min}}{T_\infty - T_i}$$

(174)
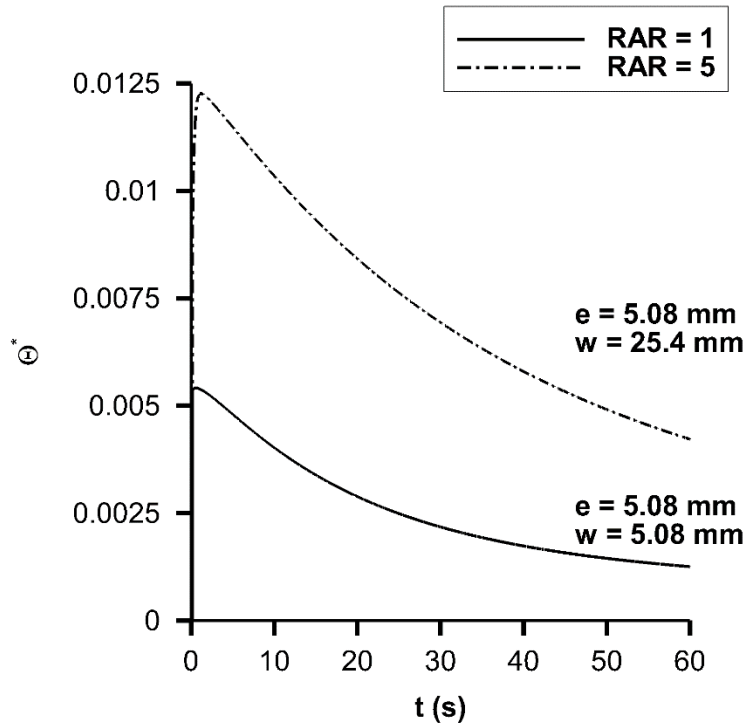
Figure 42: Spatial temperature variation within lumped solid

The spatial temperature variation within the aluminum feature is important because it represents the absolute error in the measurement of the lumped solid temperature, whether the temperature is measured using surface or point-wise measurements. For the RAR = 1 case, the worst temperature variation encountered was 0.0054 and occurred near the beginning of the simulations, when the aluminum rib is suddenly exposed to the convective boundary condition and starts to respond to the new temperature. The temperature variation in the larger rib is consistently greater than the smaller rib of similar shape and boundary condition (same heat transfer coefficient and driving temperature). For the wider ribs, the temperature variation was up to 0.0125. The thermal properties are the same for both RAR = 1 and RAR = 5, only the

164

geometric size of the rib is altered and some ratios that involve rib geometric parameters. The spatial temperature variation decrease with increasing time as the thermal information propagates into the interior, allowing the interior portions to approach the convective temperature. Using sensitivity analysis, a bias Θ of 0.0054 results in a bias uncertainty of 2% when the heat transfer coefficient is back calculated (where Θ is considered to range between 0.3 and 0.7). For the wider ribs, the bias of 0.0125 translates to an error of 5% in the heat transfer coefficient.

The maximum temperature variation in the lumped solid is represented by Θ^*. Hence, Θ^* is also an estimate of the error in the temperature measurement is perfected on the surface of the aluminum ribs (such as when TLC is painted directly onto the aluminum). Θ^* is a conservative estimate of the error, since it is defined as the difference between the maximum and minimum temperatures. The actual error is less than Θ^*, since the average temperature is in-between the maximum and minimum temperatures. Therefore, an additional factor of safety is not needed to use Θ^* as an estimate of the bias error in when measuring the average temperature using surface measurements. On the other hand, during a hybrid heat transfer experiment the lumped surface features can be glued to the PMMA surface that is already coated with TLC. In this configuration there is an interfacial gap between the temperature measurement and metallic feature; an addition bias in the temperature measurement occurs because of the thermal resistance of the interface.

Influence of Interface Contact Resistance

Analysis based on a numerical simulation without an interface resistance will not capture the error in the base temperature measurement if the metallic features are glued onto an already TLC coated surface. Hence an additional simulation was performed with the added contact resistance (by setting the interface thickness to the finite amount) for the RAR = 1 case. The temperature at the nodes at the interface layer adjacent to the substrate was extracted from the numerical simulation. The temperature at the substrate-adjacent layer is a lower temperature, which occurs after the heat has travelled past the thermal resistance of the interface (past the contact resistance). The temperature of the substrate-adjacent layer is therefore the temperature that would be recorded by the temperature indicators during the hybrid heat transfer experiment. The average temperature of the substrate-adjacent nodes is considered to be the base temperature. This base temperature is compared with the average temperature in the aluminum region and scaled using the initial driving temperature difference. The non-dimensional temperature difference, $\Delta\Theta_{base}$, Eq. (175), is plotted for the duration of the numerical simulation.

$$\Delta\Theta_{base} = \frac{\bar{T}_{avg} - \bar{T}_{base}}{T_\infty - T_i} \tag{175}$$
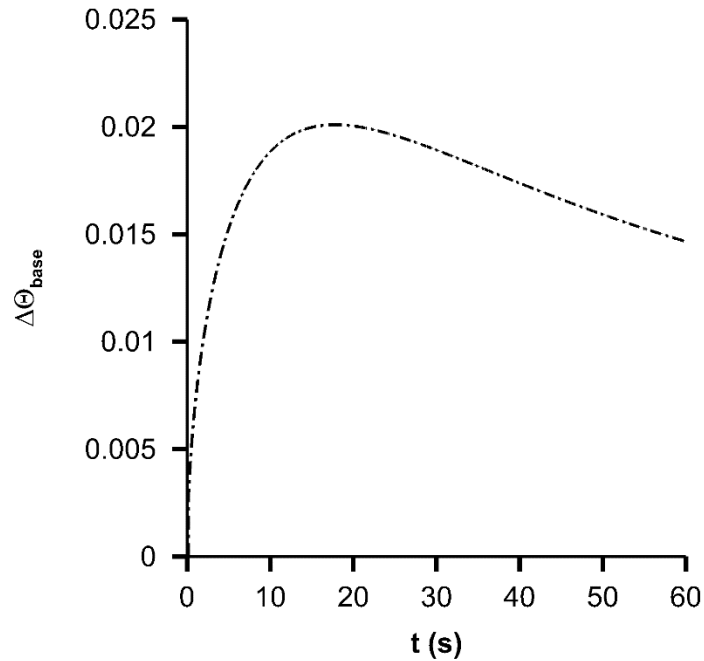
Figure 43: Bias error of imperfect contact

The variance in the base temperature nodes for both the perfect contact and with the contact resistance was found to be negligible, less than $6 \cdot 10^{-4}$ K or a variance in of $3 \cdot 10^{-5}$. Hence, comparing the average of the base nodes to the volumetric average temperature of the aluminum rib is a reasonable comparison, rather than having to deal with a localized treatment of the different base node temperatures. A maximum value of $\Delta\Theta$base encountered was 0.02. This peak occurred at an intermediate time at approximately 17 seconds.

When the aluminum ribs are glued to the PMMA substrate, various values of the interface contact resistance will be encountered. The contact resistance for aluminum-aluminum contact with air as the interfacial fluid is among the greatest that will be encountered. If filler

167

materials are used in the interface (such as thermal paste and thermal adhesives), then the contact resistance will be less. Hence the reported maximum of 0.02 for $\Delta\Theta_{base}$ is a fairly conservative estimate of the actual error in the measurement of the average temperature using a base temperature indicator. The actual error may vary between none for perfect contact and the reported value of 0.02. Based on a bias in the temperature measurement of 0.02, the bias in the inverse calculation of the heat transfer coefficient was found to be 6%. The 6% error was determined by considering the error propagation for the inverse problem, or sensitivity analysis. The reported value of 0.02 is for this particular rib geometry and may not be universal. For surface enhancement features of other geometry, it is recommended to perform a separate analysis using a similar procedure for a more accurate estimate of the error.

Validity of Enhanced Lumped Capacitance Model

The numerical simulation based on the finite volume method has the advantage that few assumptions are made, since the heat transport equation was solved in both the aluminum and PMMA regions. The results from the numerical simulation can also be used to quantify the error in the modeling assumptions used in the enhanced lumped capacitance model. The volumetric average temperature of the aluminum simulation taken from the numerical simulation (T_{FVM}) is compared with the temperature predicted by the enhanced lumped capacitance model (T_{ELC}.). T_{ELC} is computed using the analytical solution to the enhanced lumped capacitance model and T_{FVM} calculated based on the temperature results from the FVM simulation. The temperature difference, $\Delta\Theta_{err}$, based on these two parameters is scaled by the initial driving temperature difference, Eq. (176). The average temperature computed from the finite volume method based simulation is considered the true volumetric average temperature where, unlike the lumped

capacitance model, which assumes a spatially uniform temperature profile, no assumptions were
made concerning the spatial uniformity of the temperature distribution in the aluminum region.
The temperature difference between the average temperature computed from the FVM
simulation and prediction by the enhanced lumped capacitance model are plotted in Figure 44 for
RAR = 1 & 5 configurations (with e = 5.08 mm). Both the perfect contact and contact resistance
simulations for the RAR =1 case are plotted in the figure (the RAR = 5 case was only simulated
using a perfect contact). The perfect contact cases are plotted with solid lines; the contact
resistance case is plotted with a dashed line.

$$\Delta\Theta_{err} = \frac{T_{FVM} - T_{ELC}}{T_\infty - T_i}$$
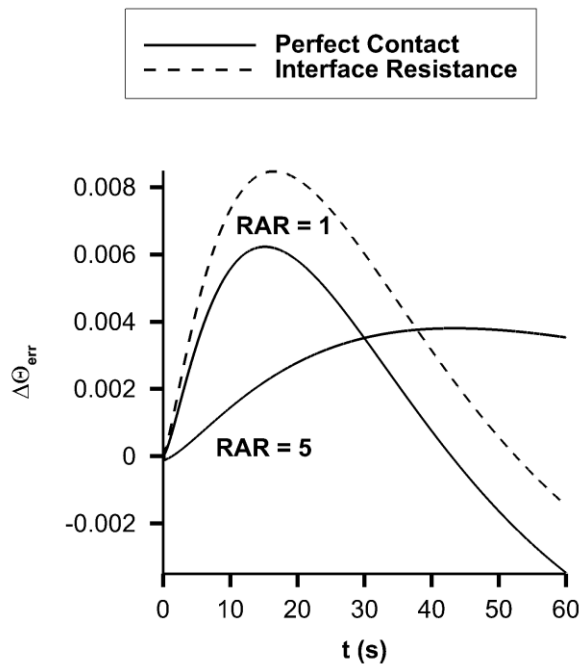
(176)

Figure 44: Modeling error of enhanced lumped capacitance model

169

Because the enhanced lumped capacitance model assumes perfect thermal contact, the prediction by the analytical solution deviates from the FVM simulation with contact resistance more than with the perfect contact. For RAR = 1, the maximum value of $\Delta\Theta_{err}$ was 0.0062 for perfect thermal contact and 0.0085 with an interface resistance. Again using the sensitivity analysis, these biases translate to a 1.8% error in the back-calculated heat transfer coefficient for the perfect contact case and 2.5% if there is a contact resistance. For RAR = 5, the maximum value of $\Delta\Theta_{err}$ was 0.0038, which yields a 1.5% error in the heat transfer coefficient. Even though the spatial temperature variation of the wide rib (RAR = 5 case) was more significant than the small rib (RAR = 1 case), the modelling error, based on $\Delta\Theta_{err}$, was less for the large rib than the smaller rib. For the prefect contact case, the root-mean-square of $\Delta\Theta_{err}$ was nearly the same for both RAR = 1 and RAR =5.

Using sensitivity analysis, Yan and Owen demonstrated that $\Theta = 0.5$ is the optimal value for minimizing the uncertainties in the calculated heat transfer coefficient; and Θ should be limited to between 0.3 and 0.7 [74]. The error amplification is relatively small if the non-dimensional temperature is within the range of $0.3 < \Theta < 0.7$, allowing the heat transfer coefficient to be accurately computed. Yan and Owen determined this optimal value by considering all the uncertainties in the temperature measurements to be equal and uncertainties from parameters such as the elapsed time to be negligible. Although the analysis by Yan and Owen did not consider errors introduced by modeling assumptions such as multi-dimensional effects or thermal resistances, the optimal range of $0.3 < \Theta < 0.7$ precedes these effects. Outside this range, even small errors in the temperature measurement are greatly amplified, which adversely affects the calculation of the heat transfer coefficient. Recall that even though the bias

error in $\Delta\Theta_{err}$ was less than 0.01 the error in the back-calculated heat transfer coefficient was slightly more than 1%, because of the error amplification. On the other hand, the uncertainty in Θ for a typical experiment can be up to 5-10% and is much more significant compared to the errors stemming from the modelling assumptions.

Error Range for Classical Lumped Capacitance Model

Previous sections used the results from the numerical finite volume method based simulation to demonstrate that the errors stemming from the use of the enhanced lumped capacitance model were acceptable. Errors stemming from multi-dimensional effects and surface contact resistances were quantified and found to be less significant than errors from other sources. Before the exact solution to the enhanced lumped capacitance model was available, previous experimenters used the classical lumped capacitance model to compute the heat transfer coefficient [53, 54, 56, 57, 65, 73, 75]. In this section, the performance of the classical lumped capacitance model is compared directly with the enhanced model in order to show that the error from its misuse is not negligible as previously believed. The parameters of the rib geometry are similar to the FVM study and recent experiment [62]. The parameters for the lumped solid are varied by changing the rib aspect ratio, from the baseline case of 1 to 3 and 5, while alternatively holding the rib height constant (e = constant) or rib width constant (w = constant). In a previous experiment, the rib height was held constant and ribs of different aspect ratios were tested, by altering the rib width to achieve RAR = 1, 3, & 5, in order to test ribs of various aspect ratios with the same relative roughness [57].

The same thermal properties for aluminum are used from Table 13 as well as the heat transfer coefficient of 250 W/(m^2·K). The non-dimensional temperature Θ, as a function of time, of the lumped solid temperature is plotted in for Figure 45 for RAR=1, 3, & 5 with the rib height held constant and Figure 46 also for RAR = 1, 3, & 5 for a constant rib width. Θ is defined according to Eq. (180) and is computed from the analytical solution to the enhanced lumped capacitance model, Eq. (181). Each curve in Figure 45 and Figure 46 was generated by

applying the correct convective surface area and contact area corresponding to each combination of rib height and rib width. Table 15 lists the various combinations of rib height and width. For convenience, the equation defining the rib aspect ratio is Eq.(177), the convective surface area is Eq. (178), and the contact area is Eq. (179)

Table 15: Rib Parameters

	RAR = 1	RAR = 3	RAR = 5
e = 5.08 mm	5.08 mm	5.08 mm	5.08 mm
x	x	x	x
w varied	5.08 mm	15.24 mm	25.4 mm
e varied	5.08 mm	1.693 mm	1.016 mm
x	x	x	x
w = 5.08 mm	5.08 mm	5.08 mm	5.08 mm

$$RAR = \frac{w}{e} \qquad (177)$$

$$A_s = 2e + w = e \cdot (2 + RAR) \qquad (178)$$

$$A = w = e \cdot RAR \qquad (179)$$

$$\Theta = \frac{T(t) - T_i}{T_\infty - T_i} \qquad (180)$$

$$\frac{T(t) - T_i}{T_\infty - T_i} = \frac{\xi_1\left(1 - exp(\xi_2^2(t))erfc(-\xi_2\sqrt{t})\right) - \xi_2\left(1 - exp(\xi_1^2(t))erfc(-\xi_1\sqrt{t})\right)}{(\xi_1-\xi_2)} \qquad (181)$$
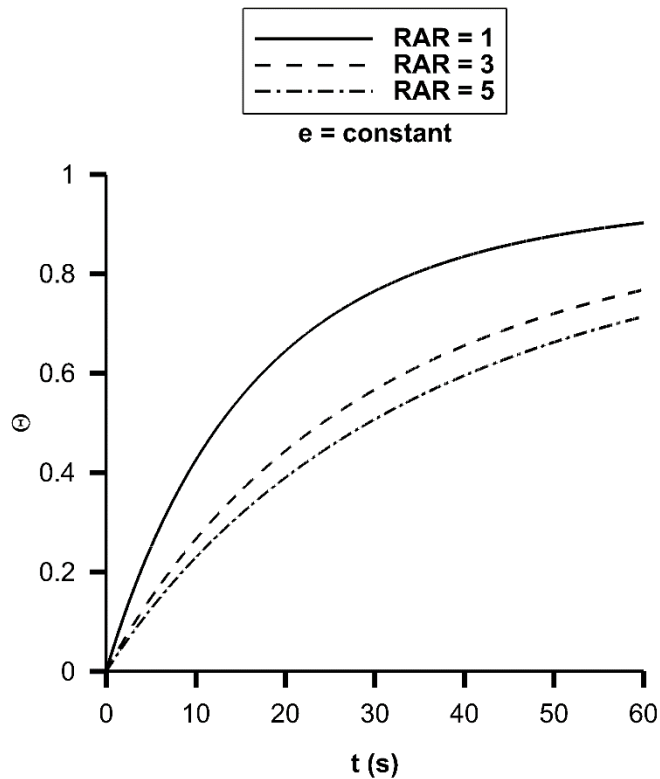
Figure 45: Rib temperature evolution for different RAR with e held constant

When the rib height is held constant, the volume, heat capacitance, and time-constant increases as the rib aspect ratio increases. Additionally, the contact area increases linearly with the rib width. A consequence is that the ratio of the heat capacity to the contact area is also a constant, no matter the change in rib aspect ratio. Hence, the RAR affects only the time constant of the rib. These parameters result in the temperature curves having the same shape, with different response times, but curves from different RAR do not intersect.
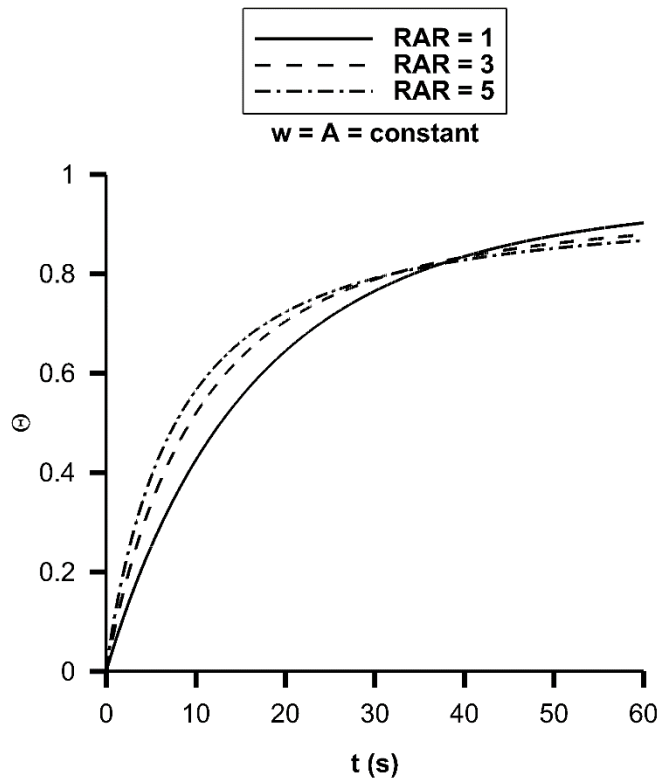
Figure 46: Rib temperature evolution for different RAR with w held constant

Unlike when the rib height is held constant, the ratio of the heat capacitance to contact area does change if the rib width is held constant and the rib aspect ratio is varied. Increasing the rib aspect ratio requires a reduction in the rib height, which reduces the volume, even though the contact area remains constant. Hence, temperature curves from different rib aspect ratios can cross and intersect. When the rib height was held constant, different curves did not intersect.

The apparent heat transfer coefficient is the heat transfer coefficient that would be computed if the classical lumped capacitance model was blindly applied. When the analytical solution to the classical lumped capacitance model is used, the inverse solution of the heat transfer coefficient in terms of the other parameters is given by Eq. (182).

$$h_{app} = -\frac{\rho V c}{A_s \cdot t} \ln(1 - \Theta)$$

(182)

For each of the forward calculations of temperature, the apparent heat transfer coefficient was calculated by using Eq. (182). The relative error in the computed heat transfer coefficient is given by Eq. (183). If the heat transfer coefficient is not known *a priori*, then the heat transfer coefficient calculated using the enhanced lumped capacitance model may be used as the reference value (since it is closer to the actual value than the classical model). The percentage error in the perceived heat transfer coefficient when the lumped capacitance model is applied is plotted in Figure 47 for cases when the rib height was held constant and Figure 48

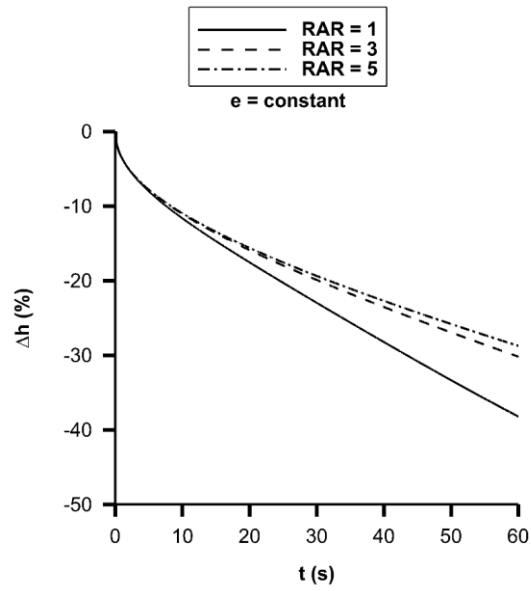$$\Delta h = \frac{h_{app} - h_{actual}}{h_{actual}}$$

(183)

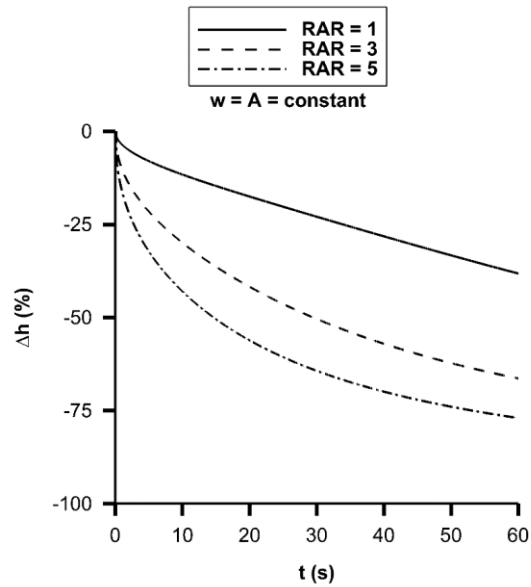Figure 47: Error encountered for classical model with e Held Constant

Figure 48: Error encountered for classical model with w held constant

177

Since the classical lumped capacitance model does not account for the heat conducted into the substrate, it over-predicts the lumped solid temperature and under-predicts the heat transfer coefficient; the apparent heat transfer coefficient is always less than the actual heat transfer coefficient when the classical lumped capacitance model is applied). For both cases, the classical model deviates further with increasing time. The error range of applying the classical model is summarized in Table 16, considering an effective testing window with $0.3 < \theta < 0.7$ (approximately 10 to 30 seconds). The errors in applying the classical lumped capacitance model can be quite large, with the investigated range of 9-54% error depending on the rib geometry and the time at which the temperature indication should take place.

Table 16: Summary of $|\Delta h|$

	RAR = 1	RAR = 3	RAR = 5
e = 5.08 mm w varied	9-20%	12-26%	13-28%
w = 5.08 mm e varied	9-20%	20-42%	27.54%

The analysis in this section utilized a rather arbitrary selection of rib parameters; the parameters were chosen based on similar values encountered in previous experiments. However, the method of analysis used is rather universal. For a given set of known conditions, the temperature evolution of the lumped solid using the enhanced model can be computed from the analytical solution to the enhanced model, Eq. (181). Then the apparent heat transfer coefficient can is computed from the solution of the classical model, Eq. (182) . The computation of the relative error is then straightforward, by using Eq. (183).

178

Contamination Effects onto Substrate

The focus of this section is on the inter-rib region where the enhanced lumped capacitance model is not used. Recall that in the hybrid heat transfer experiment, a lumped capacitance approach is used underneath the metallic features. Away from the features, the classical one-dimensional semi-infinite solid model is used. The finite volume method simulation used to analyze the validity of the enhanced lumped capacitance model can also be used to analyze any adverse effects in the inter-rib region. Away from the rib features, it is expected that the one-dimensional semi-infinite solid model may be used without ill effects caused by the presence of a metallic rib feature. However, near the feature but still in the inter-rib space, the substrate might still experience some influence of the metallic rib. The process of thermal diffusion from the metallic rib into the inter-rib space is sometimes called thermal contamination. It is called contamination because it negatively affects the validity of the one-dimensional semi-infinite solid model. Essentially, the presence of the metallic rib induces multi-dimensional heat conduction effects, which violates one of the fundamental assumption of the one-dimensional semi-infinite solid model (it is assumed that the heat conduction is strictly one-dimensional).

The temperature on the exposed surface of the PMMA region at each time-step was extracted from the numerical simulation (the same N1 grid was used for this analysis). The non-dimensional temperature was computed from the local temperature and used to calculate the apparent heat transfer coefficient. Unlike for the aluminum rib where the solution to the lumped capacitance model was used, here the solution to the one-dimensional semi-infinite solid model was used to back-calculate the apparent heat transfer coefficient. Recall that the heat transfer coefficient applied in the simulation was 200 W/(m^2·K) and is thus known *a priori*. The relative

error in back-calculated heat transfer coefficient then can be computed using the previous method, Eq. (183). The error in the back-calculated heat transfer coefficients are plotted in Figure 49 for all the available surface nodes and all available time-steps.

Figure 49: Contamination on inter-rib region
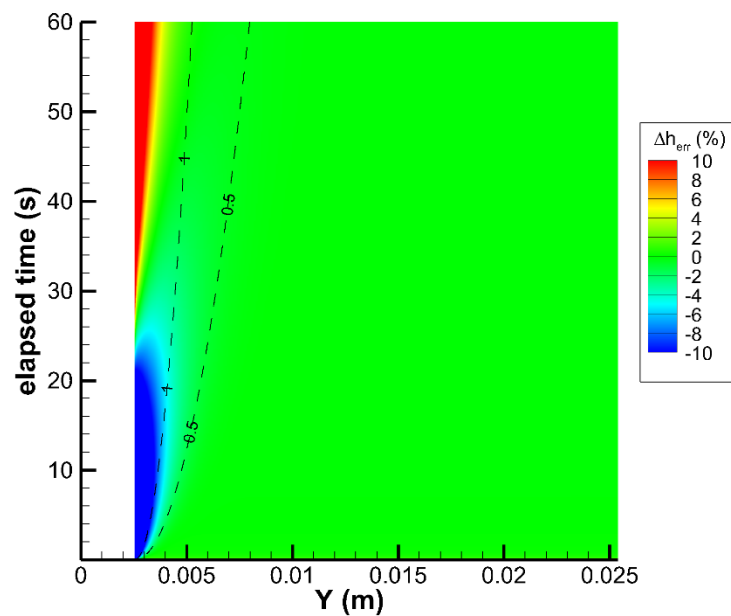
The contours are shaded based on the percentage error in the heat transfer coefficient, but the range is clipped to -10% and +10%. The Fourier number based on distance from the rib, Eq. (184), is plotted in figure as dashed lines for values of 1.0 and 0.5. Since the length scale appears in the denominator of the Fourier number, it decreases further away from the rib (greater Y).

$$Fo = \frac{\sqrt{\alpha t}}{Y - \frac{e}{2}} \qquad\qquad (184)$$

The apparent heat transfer coefficient under-predicts during early times (the first 20-25 seconds) and over-predicts for later times. The amount of which the heat transfer coefficient is under-predicted or over-predicted is difficult to determine for the general case. That is because it depends on the properties in the metallic rib region (heat capacity, time-constant) as well as the heat transfer coefficient there. In this simulation, a heat transfer coefficient of 250 W/(m^2·K) was applied to the ribs. For early time, the heat capacity of the aluminum rib does not respond quickly to the change in boundary condition and the underlying substrate does not experience the temperature change immediately. In this early regime, the temperature in the inter-rib region increases faster than underneath the aluminum rib, causing the heat to leak into the space underneath the rib. This heat leakage effect causes the temperature at the nodes adjacent to the base of the rib to be lower than they would have been had the aluminum rib not been present, resulting in the under-prediction of the heat transfer coefficient. Eventually the aluminum rib catches up, partly because of the higher heat transfer coefficient, and the heat loss into the substrate starts to become significant. In this later regime, the aluminum rib, because of its higher heat capacity and greater thermal energy storage, maintains the temperature of the base nodes higher than if the aluminum rib were not present. This later regime is characterized by heat leaking from the aluminum rib into the inter-rib space, raising the temperature of those nodes and causing the heat transfer coefficient to be over-predicted. The degree of under-prediction or over-prediction can be unacceptably large, up to 80-90% for the nodes closest to rib. However, only

181

the regions closest to the aluminum rib are affected. Approximately one rib height away from the rib, the error is a more tolerable 1%; after two rib heights the error is less than 0.1%. It is found that the regions where the error in the heat transfer coefficient are worse than 10%, are contained within the region where the Fourier number is greater than one. A Fourier number of approximately 0.5 appears to mark areas where the error is worse than 1% and a Fourier number approximately equal to 0.3 marks areas with an error greater than 0.1%. Outside of these regions, (where the Fourier number is less than 0.3) there is negligible error when the one-dimensional semi-infinite solid model is applied (less than 0.1%).These demarcation lines may be more visible in Figure 50, where the error is plotted on a banded contour plot rather than continuous colors.
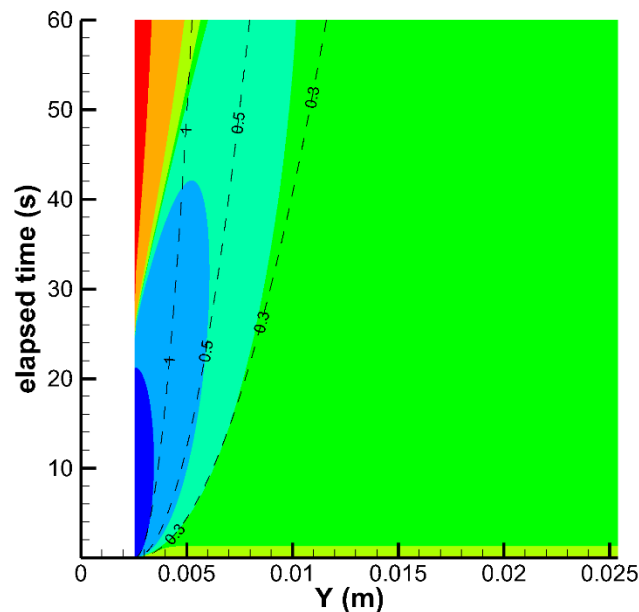
Figure 50: Error plot for inter-rib region

DEMONSTRATION OF HYBRID HEAT TRANSFER TECHNIQUE

Detailed Nusselt number measurements were performed for a square channel with ribs on one wall in the Reynolds number range of 50,000-150,000 using the hybrid version of the transient thermochromic liquid crystals technique. The rib aspect ratio is 1:1, the rib height-to-hydraulic diameter ratio is 0.10, the rib-pitch–to–rib-height ratio is 10, and the ribs are oriented orthogonal to the streamwise direction. These ribbed channel configurations are encountered in industrial power generation turbines.

Measurements performed on all four walls allow a nearly complete picture of the heat transfer distributions in the cooling channel. A benefit of having measurements on all four walls is that the bulk temperature variation throughout the channel during the transient experiment can be accounted for with fewer assumptions.

Ribs made out of Rohacell and aluminum were used simultaneously. The enhanced lumped capacitance model is used to resolve the average heat transfer of the aluminum rib features. A comparison of the data obtained using the Rohacell and aluminum rib features is made to quantify experimentally the influence of the rib-induced thermal contamination. Friction augmentation, overall heat transfer augmentation, and overall thermal performance are also reported for this configuration.

Experimental Setup

 The current experimental setup is a significant advancement over previous transient TLC

experiments that were performed at the facility. A schematic of the open loop wind tunnel is

shown in Figure 51. Figure 52 is a photograph of the wind tunnel while it was being built.
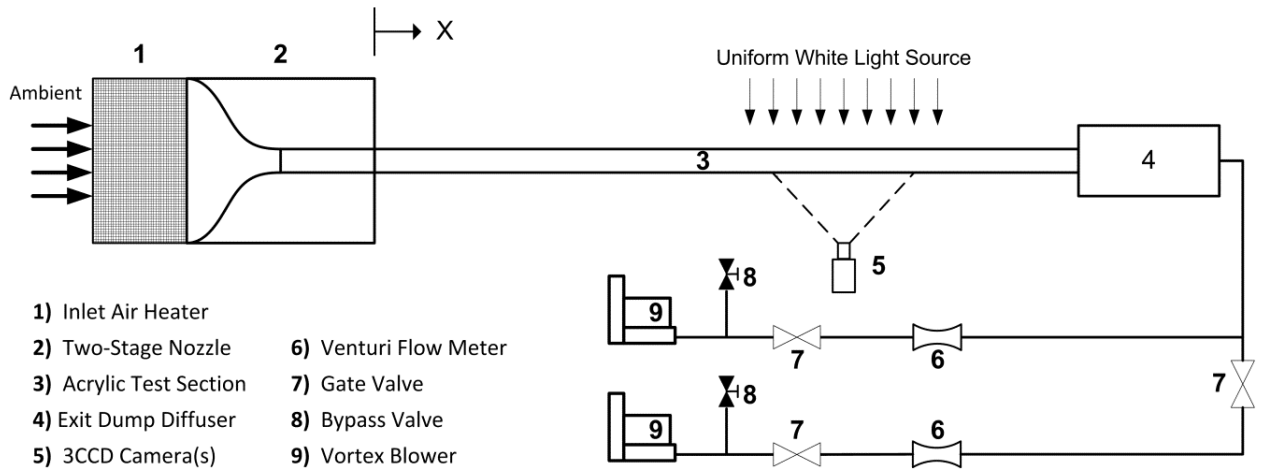
Figure 51: Sketch of experimental setup
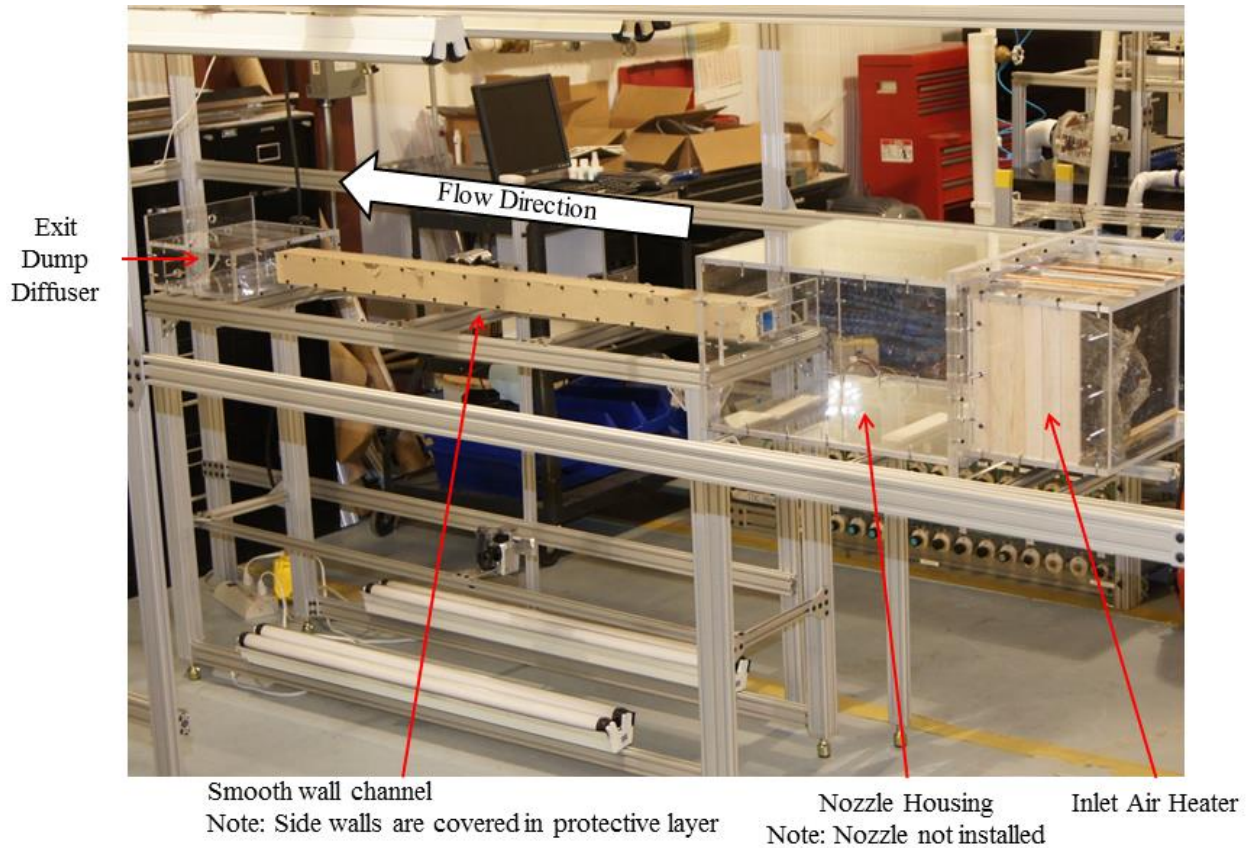
Figure 52: Partially assembled wind tunnel

The inlet is open to ambient conditions. Air enters the inlet air heater before entering the two-stage contraction which contracts the flow to the test section dimensions. The compact heater has a rectangular cross section, dimensions of 45.7 cm by 30.5 cm. Figure 53 is a photograph of the air heater at the inlet of the wind tunnel. The inlet air heater is powered by a Staco 6020-3Y autotransformer, capable of delivering 29.1 kVA (shown in Figure 54).
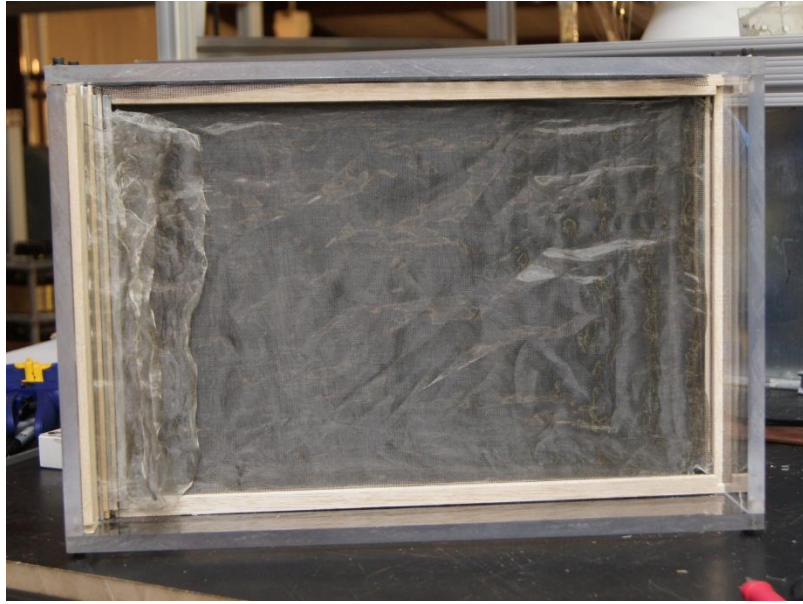
Figure 53: Inlet of mesh heater
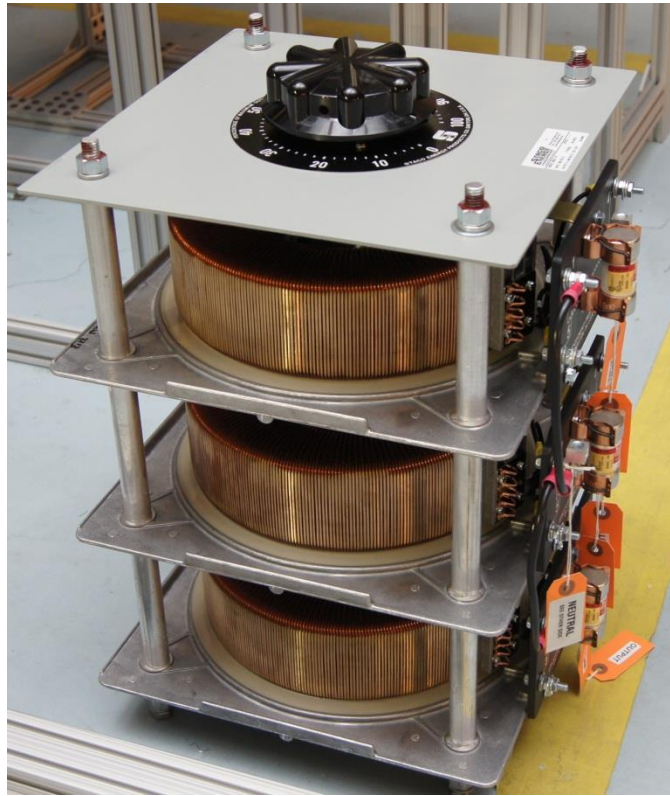
Figure 54: Staco 6020-3Y Autotransformer

The flow passes over 24 stainless steel mesh screens inside the heater region. The screens are composed of optical grade, high transparency T316 stainless steel mesh (80 mesh per 2.54 cm, plain square weave, wire diameter 0.0305 mm, 81% open area percentage). The 24 screens are connected in a striped configuration in order to form a balanced 3-phase wye resistance heater (8 screens per branch). The number of total screens was selected to minimize the bulk temperature increase per screen to prevent the development of large temperature variations. The heater dimensions are then chosen to optimize the resistance of the heater configuration as well as minimize the oncoming flow velocity and minimize the pressure loss across the heater screens. After the heater, the flow area changes in a two-stage contraction. Each stage is a 1D contraction accomplished with a matched symmetric cubic profile. Both stages of the nozzle have the same length of 30.5 cm. In the 1st stage, the flow experiences a 6:1 contraction in the Y-direction immediately followed by the 2nd stage, a 9:1 contraction in the Z-direction. The two-part nozzle is constructed out of foam supported in an acrylic housing. The flow exits the acrylic test section via a dump diffuser which transitions to the circular plumbing. A two-stage contraction was used for added flexibility. The wind tunnel was designed to handle channel aspect ratios of up to 5. The different contraction stages can be rebuilt to achieve other aspect ratios as shown in Figure 55.
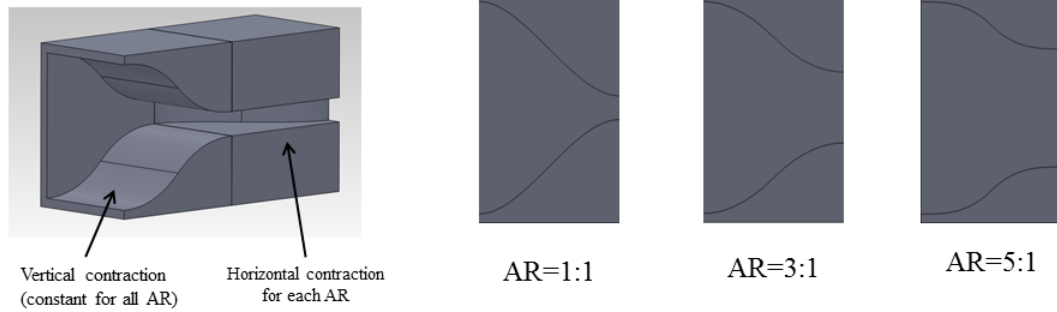
Figure 55: Different contraction assemblies

Two parallel 15 horsepower (10 kW) regenerative vortex blowers, Figure 56, operating under suction induce the flow through the test section. The flow rate is metered with separate venturi flow meters, Figure 57, installed in each parallel circuit along with gate valves and bypass valves to control the flow rate. Additional gate valves allow for each of the parallel circuits to be shut off so that only one venturi-blower combination is needed for the lower flow rates. The differential pressure reading, static pressure at venturi throat, and flow static temperature were measured using handheld digital manometers and thermocouple readers.

Figure 56: Regenerative vortex blower

188

Figure 57: Venturi flow meter

Test Section

The test section is a 4-walled channel of PMMA. The channel height is 5.08 cm, width 5.08 cm, and length 152.4 cm. The top and bottom walls are fabricated from 12 mm thickness stock. The side walls are thicker, 18 mm, to allow the channel to be assembled according to Figure 58. The origin of the coordinate system is placed at the geometric center of the flow cross section at the inlet of the test section. Also shown is the relative positioning of the 3CCD cameras and fluorescent light strips.

The time history of the visible color change of the TLC coating is recorded with Panasonic PV-GS180 3CCD cameras with 720 pixels x 480 pixels resolution and a capture frame-rate of 30 frames per second. The four cameras are mounted and centered over and orthogonal to each of the test section walls as depicted in Figure 58.
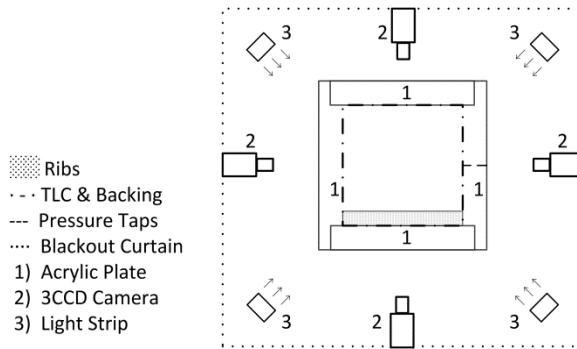
Figure 58: Camera and Lighting arrangement

High color rendering index (CRI) fluorescent white-light lamps were installed on the rig frame to achieve a constant and uniform lighting condition for the TLC. A frame was built around the setup from the inlet air heater to the exit of the test section and was completely covered with Roc-lon budget blackout fabric to block any ambient lighting near the TLC test section, Figure 59. The test section is located entirely inside the covered enclosure.

Figure 59: Covered enclosure

The four 3CCD cameras (Panasonic PV-GS180) are connected to the PC via IEEE 1394

Firewire interface so that the videos can be recorded directly to PC without the need to perform a

time-costly conversion from film tapes. The four 3CCD cameras used are the same ones used for

the calibration. The PC is also connected to the DAQ for the thermocouple measurements as well

as a separate DAQ with a digital 5 Volt output channel, which controls the power through the

heater via a solid state relay. The solid state relay controlled by the DAQ is visible in the top of

Figure 60. The solid state relay is routed to the supply line and controls a 4-pole 3-phase

contactor, the 4-pole contactor is visible in the bottom of Figure 60.
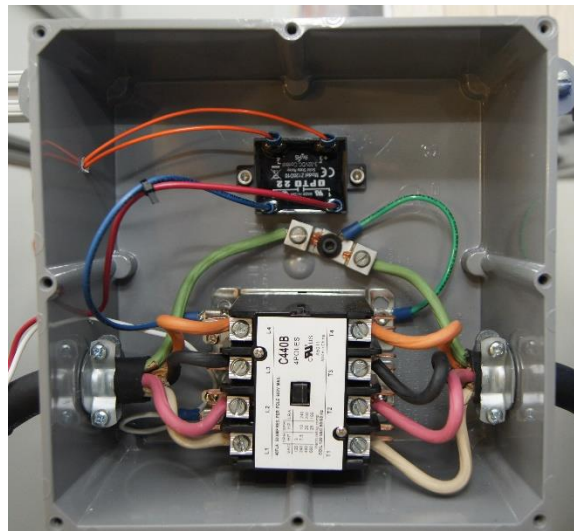
Figure 60: Relay-Contactor assembly

The DAQ used is a PCIM DAS16JR/16. 16-bit analog-to-digital converter with support

of up to 16 channels (either 8 differential or 16 single-ended measurements). The DAQ is

equipped three 16-bit internal counters (82C54 chip package) to provide clock, gate, and output

connections. The maximum sampling rate of the DAS16 is 100 kHz while the clock frequency

can be configured to operate at 1 MHz or 10 MHz (we used it in 10 MHz mode). The DAS16 is also equipped with a 1024 sample FIFO buffer (First In, First Out), which assures that data taken from the board is transferred into the computer memory without missed samples.

For thermocouple measurements, the thermocouples are interfaced to the DAS16 with a multiplexed expansion board (CIOEXP32). The expansion board increases the maximum number of connections to 32 channels per CIO-EXP32 board used by binning the channels to two banks of 16 channels. The CIO-EXP32 can be daisy chained up to four-way, to increase the maximum number of thermocouples connected to the same DAS16 board to 128. The maximum number of connections is not 256 because 1 channel (out of the 16) on each board is always reserved for the CJC (cold-junction compensation) unit. The CJC unit has a coefficient of 24 mV per °C and is engineered to produce an output voltage of 0 mV at 0 °C.

Individual banks on specific expansion boards are accessed by the DAS16 by using the 4 digital output channels. The 4 digital outputs serve as binary triggers to select a particular expansion board and particular bank on each board (using 4 bit binary logic). The binary mapping is configured by physical jumper switches located on the expansion boards and are user configured.

The output voltage of a thermocouple circuit is on the order of a few millivolts, which cannot be accurately measured by a DAS16 without additional signal conditioning. The DAS16 is configured for a full scale operating range of ± 10V (with a resolution of 305 μV). The CIO-EXP32 provides an analog voltage amplifier (gain) for each bank. Four amplifiers are installed with gains of: 10x, 100x, 200x, and 500x. The amplifiers may be compounded and any of the 16

possible combinations of the amplifiers may be use. Since T-type thermocouples were used, only the 100x amplifier was used. Additional analog filters can be installed on the expansion cards by physically soldering resistors and capacitors, the PCB already has dedicated junctions for these filters. Although the expansion cards were capable, no analog filters were not used in this work.

During the transient heat transfer experiment, the start of relay activation, measurement of temperature data, and video acquisition are all coordinated, by a LabVIEW control algorithm, to occur simultaneously. The LabVIEW algorithm constructs a buffer for all four videos beforehand in the computer RAM (random-access memory). The buffer allows the video feed from the 3CCD cameras to be loaded directly onto the computer memory without dropping frames and in uncompressed video format (corresponding to raw intensity readings). The PC used had 24 GB of RAM, which allowed for just over 60s of video to be recorded at full resolution (720 px x 480 px) on all four cameras. The 5 V output channel on the DAQ is connected to a solid state relay. The SSR controls a 4-pole contactor which completes the circuit between the mesh heater and 3-phase transformer. During the transient heat transfer experiment, the start of relay activation, measurement of temperature data, and video acquisition is all coordinated by the control algorithm to occur simultaneously and only after the video buffer has been built in the RAM.

Because some time is needed to allocate the large amount of RAM used, the LabVIEW algorithm waits to verify that the buffer has been constructed before triggering the solid state relay for the mesh heater and recording the measured temperatures. All the raw measurement data is stored on computer RAM and not saved to hard disk until the end of the transient heat transfer experiment because of the slower speed at which data can be written to the hard disk.

Using this approach, 10GB of video data are generated during a single transient experiment (one Reynolds number).

Although 3CCD equipment has been emphasized, single CCD sensors equipped with Bayer filters to separate the red, green, and blue components may also be used as well as CMOS-based (complementary metal-oxide-semiconductor) sensors. The 3CCD cameras used have been discontinued for several years and are largely outdated. Off-the-shelf and consumer grade cameras today support full high definition video color formats (1920x1080p). Equipment in the near future will likely comply with the newer 4k and 8k ultra high definition standards. An upgrade to these newer cameras is fairly straightforward. However, the required RAM to store the larger image resolutions is proportional to the resolution. For the same testing duration of 60 seconds, to switch to an HD 2.1 megapixel standard would need 60 GB of RAM, a 4k UHD 8.3 megapixels standard would need 135 GB and the 8k UHD 33.2 megapixels standard would require 960 GB of RAM. These RAM amounts are far in excess of the memory density available in desktop and workstation PCs today. The required hard disk space to save the videos at the end of testing is the same as the required RAM. These RAM requirements were estimated based on using uncompressed video formats. The memory requirements can be reduced significantly if encoding is used to compress the videos. Hardware encoders are nowadays built-in to the camera hardware. Using hardware encoders, the amount of computer RAM needed can be reduced significantly by compressing the videos on-the-fly. Alternatively, the videos can be compressed after the data collection to minimize the hard disk storage space. While compressed video formats are suitable for televised airwaves where complete accuracy is not a concern, the use of encoded video formats is debatable for scientific use.

Ribs are applied starting at 1H from the exit of the contraction (inlet of the test section) over the entire test section. The initial 1H length is left un-ribbed so that the hydrodynamic boundary layer of the flow entering the test section is allowed to start its development before interacting with the ribs, which reduces the tendency of flow bifurcations at the inlet which can persist further downstream. Ribs are applied to only the bottom wall with double-sided adhesive tape. The top and side walls are left smooth. Ribs are square in cross section (5.08 mm x 5.08 mm) and span the channel width in a direction orthogonal to the flow direction. The rib pitch is 10 times the rib height (p = 10e). The rib pitch is equal to the channel height (p = H).

Sprayable TLC was used without modification as purchased from LCR Hallcrest (SPN100G35C1W with a color play bandwidth of 1 ℃ centered at 35 ℃). Black backing was airbrushed on top of the TLC to improve color contrast. Unlike the calibration that was performed on the copper block, the TLC was viewed from the backside of the PMMA panel. Hence the black backing for the transient TLC experiment was sprayed over the TLC, which is opposite the procedure used during the calibration. TLC was applied only within the viewing window (17H<X<23H) where the flow is at a periodically fully developed state. A T-type thermocouple was placed immediately at the inlet of the test section (at X = 0) and two more are placed just before the TLC painted section (at X = 17H) to measure bulk temperature (T_b) and centerline temperature (T_c). The bulk temperature was measured by placing a thermocouple at the location in the channel cross section where the local fluid temperature was closest to the bulk temperature rather than the centerline temperature as suggested by Domaschke et al. [52]

The region near the TLC painted window is shown in Figure 61. The first two ribs in the interrogation window are Rohacell, followed by two checkered Rohacell and aluminum ribs, and

finally two fully aluminum ribs. A checkered rib consists of five aluminum cubes and five

Rohacell cubes in an alternating arrangement. These features can be seen in Figure 62, a

photograph of the ribbed wall near the test window. The ribs outside the TLC painted window

are all Rohacell. The aluminum ribs are applied onto the already TLC painted surface using

double-sided copper tape of 0.088 mm thickness, according to Figure 63.
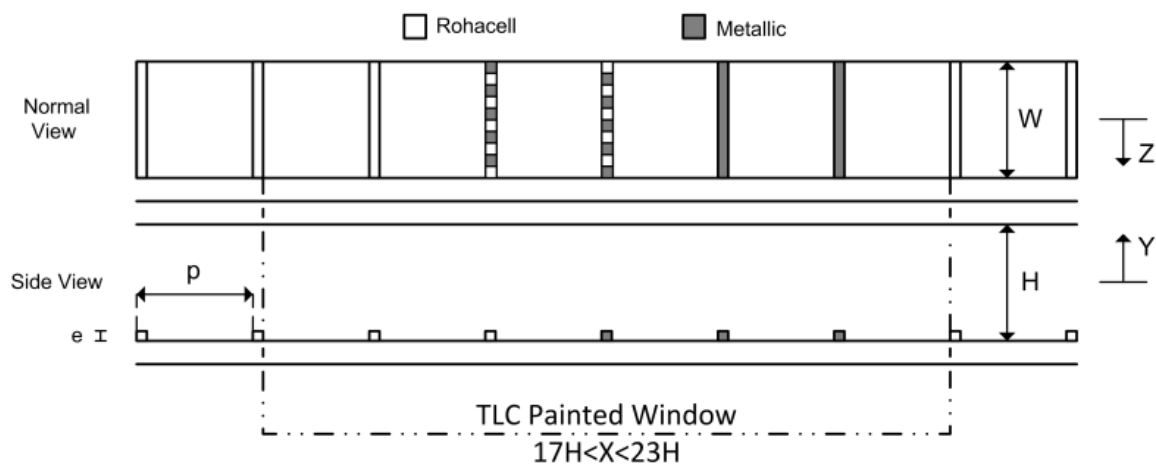
Figure 61: Rib layout
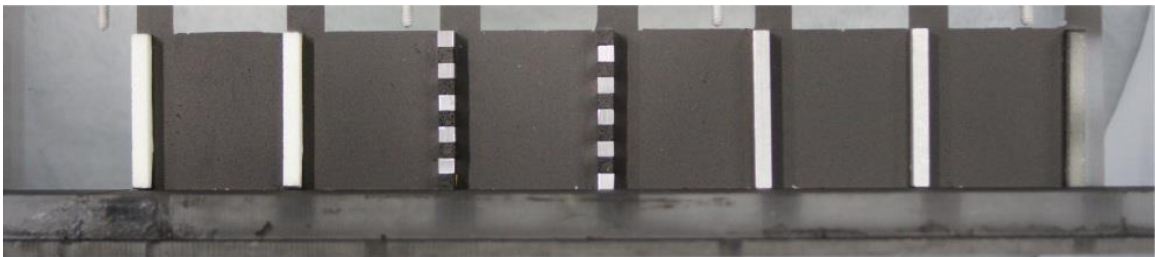
Figure 62: Photo of ribbed wall
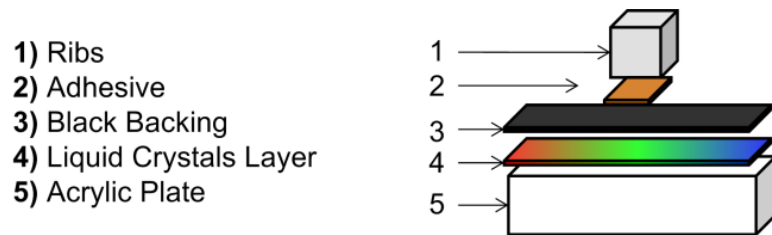
Figure 63: Assembly for metallic ribs

Rohacell is a closed-cell porous foam material with exceptionally low thermal conductivity, which allows for the Rohacell ribs to be considered nearly adiabatic. Aluminum 6061-T6 alloy material was also used for the metallic ribs. For such high Reynolds numbers and heat transfer augmentation obtained with rib turbulators, it is challenging to maintain a suitably low Biot number across the entirety of the rib. One of the concerns is whether the heat conducted from along the length of the metal rib is significant. The purpose of segmenting the ribs into smaller aluminum cubes is to reduce the amount of lateral heat conduction that occurs by placing Rohacell segments in-between two aluminum ones. A conservative estimate of the Biot number for the aluminum cube is less than 0.01. Another goal of constructing the checkered rib was to investigate whether a full-width, or contiguous, metallic rib can accurately reproduce the average heat transfer experienced by the segmented rib.

Testing Conditions

The Reynolds numbers targeted was 50,000, 75,000, 125,000, and 150,000. The channel Reynolds number, based on the unobstructed channel hydraulic diameter (D_h), is calculated from the flow conditions and metered mass flow rates. For the best replicability of flowrate and testing conditions, various gate valves were adjusted so that each tested Reynolds number was precise

197

(less than ±1% from the targeted Reynolds number). For the heat transfer experiment, the Reynolds number was taken from the conditions of the cold flow before the transient heating process. This ambiguity does not exist for the friction factor experiments. Only one blower was used for the 50,000 and 75,000 Re cases (lower flow rates are needed to achieve these Reynolds numbers); two blowers are used for the 125,000 and 150, 000 Reynolds number cases. The use of a single blower was preferred for the lower Reynolds numbers because it allows for a higher flow rate through the venturi flow meter, the higher differential pressure reading at higher flow rates could be more accurately measured.

Friction Factor Testing

The measurement of the channel friction must be done separately from the transient heat transfer experiment. A separate side wall is implemented with static pressure taps, Figure 64. The taps are equally spaced apart at the channel half-height (Y=0), with taps located at 25% and 75% of the rib pitch. Static pressure measurements are taken using a Scanivalve mechanically multiplexed pressure transducer. The pressure transduced used was a PDCR24 series transducer, a linear output transducer which supports differential pressure readings using a reference port and has a full scale output of 5 psi. A signal conditioner is also installed in the Scanivalve housing, model SCSG2/±5V/VG. The signal condition was configured to apply an analog gain of 100x to the output of the transducer.

The data from the distributed taps are monitored to verify that the flow attains a hydrodynamically periodically fully developed state. Only the 12 taps installed in the intended viewing area were used to calculate the friction factor. The pressure gradient was obtained by least-squares regression over the 12 static pressure measurements.

198
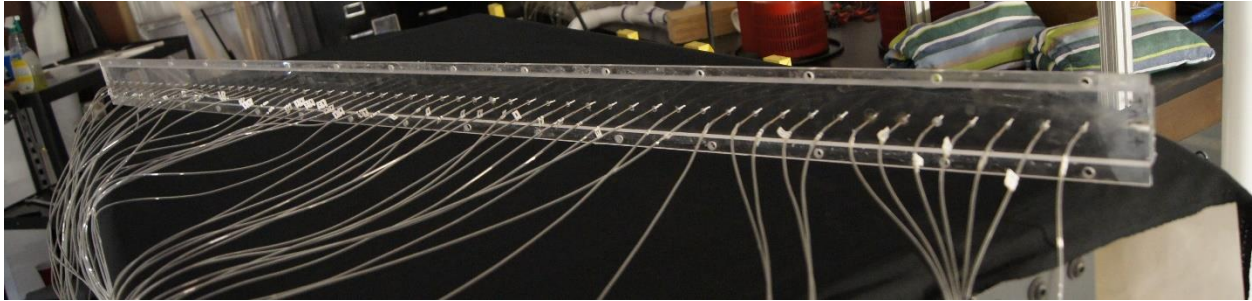
Figure 64: Sidewall with pressure taps

Heat Transfer Testing

Once the flow rate has been set for the desired Reynolds number and has reached steady state, the thermocouple temperatures are measured to obtain the initial start temperature. The transformer voltage is set so that the flow entrance temperature at the start of the TLC window is in the range of 45-55 °C. Setting the correct transformer voltage was done by trial-and-error. At the start of the test, the relay is closed and permits electricity to be transmitted to the mesh heater, which provides the temperature step for the experiment. Heat is applied until the entire wall has exceeded the color-play, at which point the power supply is turned off and the channel is allowed to cool to room temperature before the next transient experiment. The time between tests needed for the test section to cool down was around 10 minutes and tests were never conducted faster than 15 minutes apart. However, the time needed to establish the next flow rate for different Reynolds numbers often took more than 15 minutes. The testing duration was limited to 60 seconds to avoid violating the semi-infinite body assumption.

<center>Data Reduction</center>

To characterize the pressure loss in the channel for each case, the slope of the measured pressure distribution was computed over the interrogation window and the experimental friction factor was calculated using Eq. (24). The friction factor augmentation, Eq. (27), of each case was the experimentally determined friction factor normalized by the baseline value, Eq. (32).

For the non-ribbed portions of the channel, the local heat transfer coefficient was solved for using the one-dimensional semi-infinite solid model. The semi-infinite model is valid for sufficiently short test duration such that the heat penetration depth is less than the wall thickness, or equivalently the Fourier number based on wall thickness should be much less than unity [13]. Wagner et al. recommended a stricter value of less than 0.25 [63]. The maximum Fourier number was calculated to be less than 0.05, which satisfies the requirement and justifies the use of the semi-infinite body assumption.

Post processing was done in the MATLAB environment. The elapsed time history of the color change of each pixel is obtained from the digitized recorded video images. The recorded RGB intensities are digitized using an 8-bit per color scheme. The characteristic TLC temperature of the peak green color intensity is used for Tw and is obtained from calibration. Knowing T_i, T_b, T_w, the thermophysical properties of acrylic, and the time at which T_w occurs (t) for each pixel, the heat transfer coefficient at each pixel location can be determined.

The transient technique used is the so-called slow transient technique whereby the increase in flow temperature cannot be considered an ideal step-change. To account for this, Duhamel's superposition theorem is applied. By segmenting the overall temperature change into a number of smaller temperature steps, the accuracy of the method can be maintained. For both

<center>200</center>

the ribbed and non-ribbed portions of the channel, Eq. (185) is solved by taking the convolution of the appropriate solution to the constant bulk temperature case with the time-varying entrance bulk temperature by substituting either Eq. (94) or Eq. (133) for Ψ.

$$T_w(t) - T_i = \int_0^t \Psi(t-\tau) \frac{\partial T_\infty}{\partial \tau} d\tau \tag{185}$$

During the transient TLC experiment, the bulk temperature must be known at all locations spatially and temporally to calculate the surface heat transfer coefficient based on local bulk temperature. Depending on the testing conditions, the bulk temperature change over the testing window may be significant. The bulk temperature correction method by Chyu et al. [15] was applied in this work. The technique is based on the principle of a locally invariant heat flux. Heat transfer coefficients based on arbitrary reference temperatures are related to one another by the local heat flux; the relation between the heat transfer coefficient based on the entrance temperature and local bulk temperature is given by Eq. (186).

$$h_e(T_e - T_w) = h_b(T_b - T_w) \tag{186}$$

At any given streamwise position, we can compute the average of the upstream heat transfer coefficients that were computed using the entrance temperature, Eq. (187).

$$\overline{h_e}(x) = \frac{\int_{x0}^x \oint_P h_e(x,y,z)\, dx}{P_{wet}x} \tag{187}$$

A correction factor can be defined by Eq. (188) using the average upstream heat transfer just calculated (the correction factor is also related to the Stanton number).

$$C(x) = \frac{\dot{m}c_p}{\overline{h_e}} \frac{1}{P_{wet}x}$$

(188)

After some assumptions that are highlighted by Chyu et al. in their publication [49], the heat transfer coefficient based on the local bulk temperature can be computed by Eq. (189).

$$h_b(x,y,z) \approx h_e(x,y,z) \frac{C}{C-1}$$

(189)

To summarize, the method proposed by Chyu et al. is to calculate the heat transfer coefficient first using the time-varying entrance temperature, $T_b(X=17H,t)$, and to then apply an energy balance principle to calculate the local heat transfer coefficient based on the correct local bulk temperature, $T_b(17H \leq X \leq 23H,t)$.

An alternative method for correcting the bulk temperature was proposed by von Wolfersdorf et al [50] which utilizes fewer assumptions and is more accurate for long channels. The bulk temperature correction technique proposed by Chyu et al. was preferred because it uses an algebraic correction, which does not add significant post-processing time, and was easier to implement than the method by von Wolfersdorf et al.

After correcting for the local bulk temperature, the local heat transfer augmentation for a particular pixel is the local Nusselt number, based on hydraulic diameter, normalized by the baseline Nusselt number, Eq. (34), predicted by the Kays and Crawford correlation [25].

Experimental Uncertainty

The calculated uncertainty for the final results was performed using the procedures described by Kline and McClintock [76], Moffat [77], and PTC 19.1 [78] to 95% confidence level. Each rib pitch was measured to be accurate to within 3% of the overall rib pitch. The relative error of mass flow rate is 5% and pressure gradient is 2%, resulting in an uncertainty of friction factor of 10% when a single blower is used (50,000 and 75,000 Re cases) and 15% when two blowers are used (125,000 and 150,000 Re cases). Neglecting errors made in the assumptions of the models used; the typical uncertainty in the ribbed heat transfer coefficients using the enhanced model is 10%. If the 2% error from interface resistance and 6% from lumped solid assumption is included, the combined uncertainty when using the enhanced model is 12%. The uncertainty in the un-ribbed semi-infinite model heat transfer coefficients is less than 8%, resulting in an uncertainty in the overall Nusselt number of 8%. Multidimensional effects will affect the results near corners and where there are spatial variations in the convection heat transfer coefficient, these effects were not included.

Results

Smooth Wall Channel Validation

A set of smooth-wall tests is first run to validate the heat transfer and friction factor results from the experiment by testing the channel without any added ribs. Figure 65 shows the experimental friction factor for the smooth wall tests (f_{SW}). The friction factors of the smooth wall channel (SW) are within 5% of the smooth channel friction factor correlation. Figure 66 also depicts the overall averaged Nusselt number values (average along all X, Y, and Z of all walls) of the smooth channel tests (Nu_{SW}). Nusselt numbers predicted by the Dittus-Boelter correlation (Nu_{DB}) and Kays-Crawford formula (Nu_{KC}) are also plotted. The overall average Nusselt numbers of the smooth channel are within the range of these two correlations.
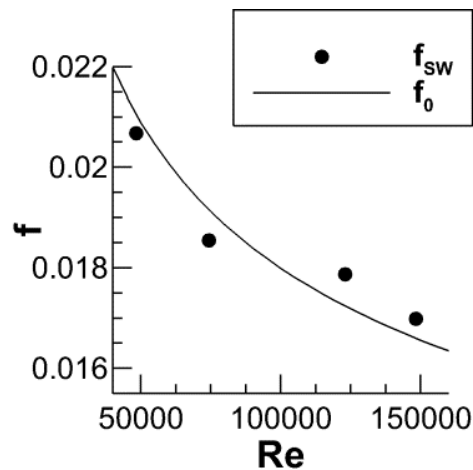
Figure 65: Smooth channel friction factor
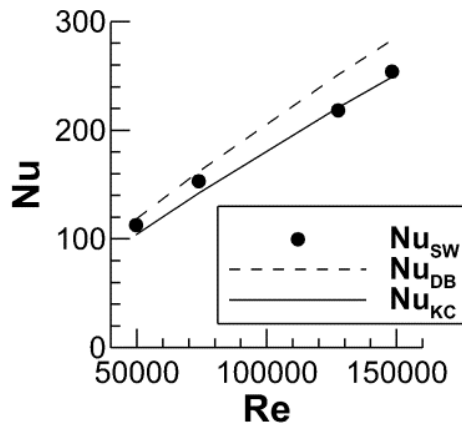
Figure 66: Smooth channel Nusselt number

Steady state copper block methods are also capable of measuring the overall heat transfer in a duct, usually with better accuracy than a transient TLC technique. The advantage of the transient TLC technique over these methods is the ability to measure the local heat transfer. The local distribution of the heat transfer augmentation is plotted in Figure 67 for the 150,000 Reynolds number test. The local distributions are fairly uniform in Figure 67 because a smooth channel was tested. Turbulators or vortex generators were not installed to generate coherent structures to alter the distribution of the heat transfer. The local heat transfer distributions for the other Reynolds numbers closely resemble the distribution for the 150,000 Reynolds number test.
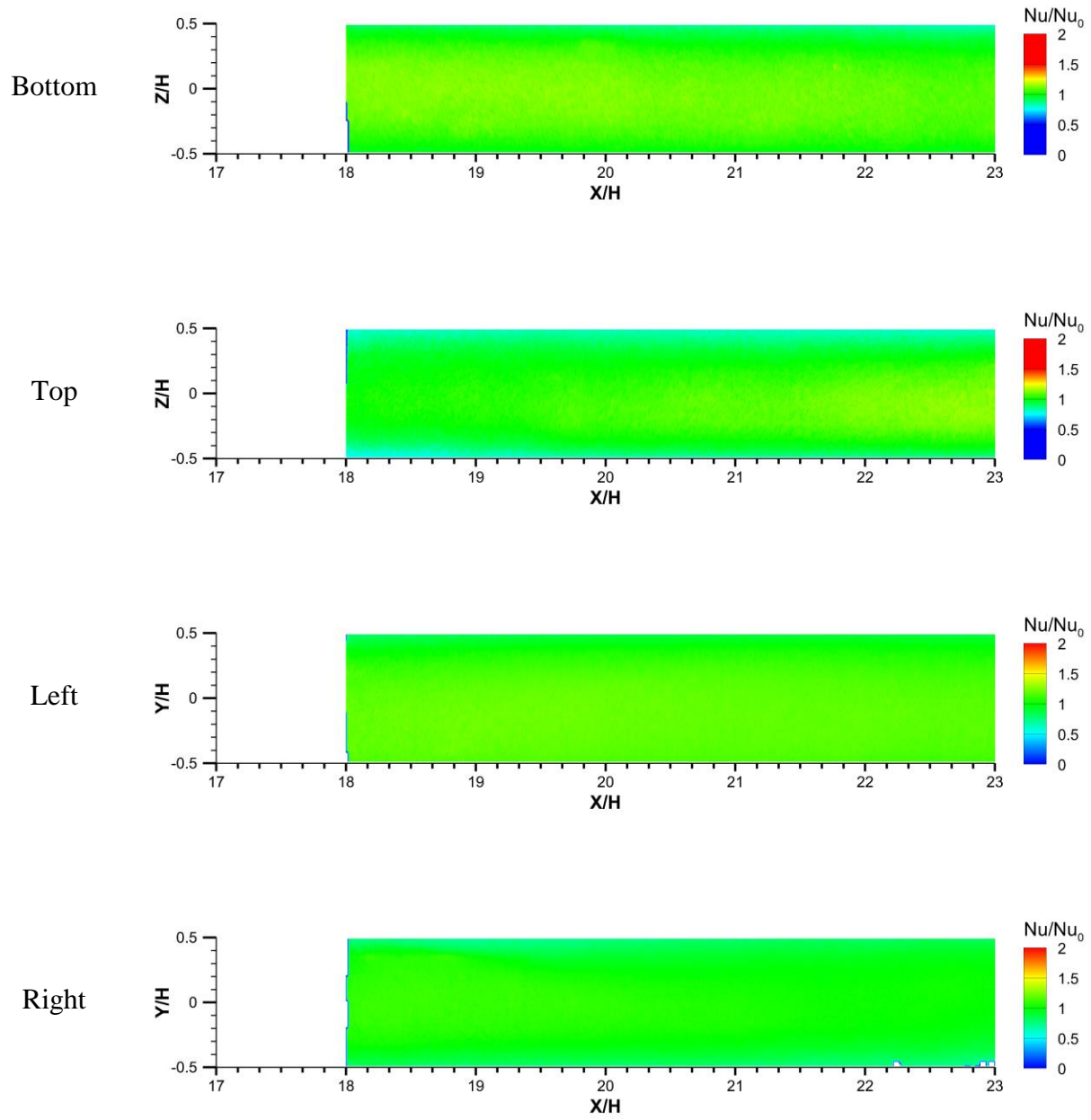
Figure 67: Local heat transfer augmentation distributions at 150,000 Reynolds number

Local distributions are important in mechanical design where the thermal stresses significantly affect the part life. The local maxima and minima of the heat transfer coefficient results in local cold spots and hot spots on the cooled part. Thermal gradients within the part gives rise to additional thermal stresses, reducing the part life. On the other hand, the maximum part temperature must also be maintained below the allowable material limit. Copper block techniques can only record the surface averaged heat transfer and cannot give any information on their local distribution.

Characterization of Inlet Turbulence

The inlet turbulence was characterized using constant temperature anemometry with single-wire hot-wire; the bridge operated in constant temperature mode. The hot-wire was positioned at the channel centerline, 1 channel height after the nozzle exit. The region immediately downstream of the inlet was avoided because that is the region of the abrupt contraction as the flow exits the nozzle contraction, there may be local zones of flow separation near the inlet. One million samples are recorded at a sampling rate of 100 kHz. From the time-series data, the mean velocities are computed and used to decompose the instantaneous velocity field into a mean and fluctuating component. The root-mean-square of the fluctuating component normalized by the mean velocity is the turbulence intensity. The turbulence intensities for each Reynolds number is listed in Table 17. In addition to providing information of the flow quality entering the test section, these turbulence intensities are needed for the inlet boundary conditions if CFD simulation is being performed by future investigators who may be trying to benchmark their simulation against the current results. They may also be used for comparison with other experiments.

Table 17: Turbulence Intensity at inlet centerline

Re	Turbulence Intensity
50,000	2.5%
75,000	3.0%
125,000	2.0%
150, 000	1.8%

Mean quantities such as the turbulence intensity do not provide information on the

unsteadiness of the incoming flow. Unsteadiness, or intermittency of the incoming flow is

undesired. Unsteadiness hints towards dynamic effects occurring upstream such as vortex

shedding or flow separation that may interfere with the data downstream in the test section.

When experiments are being conducted to determine the behavior of a stationary flow problem,

flow unsteadiness is associated with insufficient control over the environmental conditions. In

general, flow unsteadiness has a negative impact on the quality of the experiment because many

quantities are calculated assuming that the flow is stationary. For example, the heat transfer

coefficient is assumed to be a time-independent, which is a fundamental assumption of the

transient TLC technique.

Unlike laminar flows, turbulent flows are characterized by random chaotic motions. This

randomness of the flow makes it difficult to objectively and quantitatively determine the level of

unsteadiness of the flow. High frequency intermittent effects are usually overcome by the

turbulent motions. However, low frequency effects can linger longer. These low frequency

events are usually what is being referred to as unsteadiness. Unsteadiness may be caused by

intermittency in blowers and pumps used to power the wind tunnel. While difficult to quantify,

qualitatively unsteadiness appears as elevated areas in the energy and power spectral density. For a statistically stationary flow, the energy and power spectral density describes how the energy or power is distributed over different frequencies respectively.

The power spectral density of the how-wire measurements are estimated using the Welch's Overlapped Segment Averaging method. The one million samples are broken into segments of 2^{14} data points. The shortened segments are multiplied by a Hamming window with 50% overlap. The power spectral density is computed (the discrete Fourier transform is computed and then squared to obtain the power spectrum) on the windowed segments; the individual spectrums are then averaged. It is necessary to shorten the overall data series into shorter segments in order to reduce the variance in the computation of the power spectral density. The overlapped segments help to reduce the loss of information caused by the windowing. The Welch method decreases the variance (or signal noise) in the estimated power spectral density; in exchange for a loss of resolution in frequency. The power spectral density (PSD) of each Reynolds number is plotted in Figure 68. Fortunately, elevated regions in the PSD could not be determined for any of the Reynolds numbers tested. Hence, the level of unsteadiness is too low to detect compared to the natural turbulence of the wind tunnel.
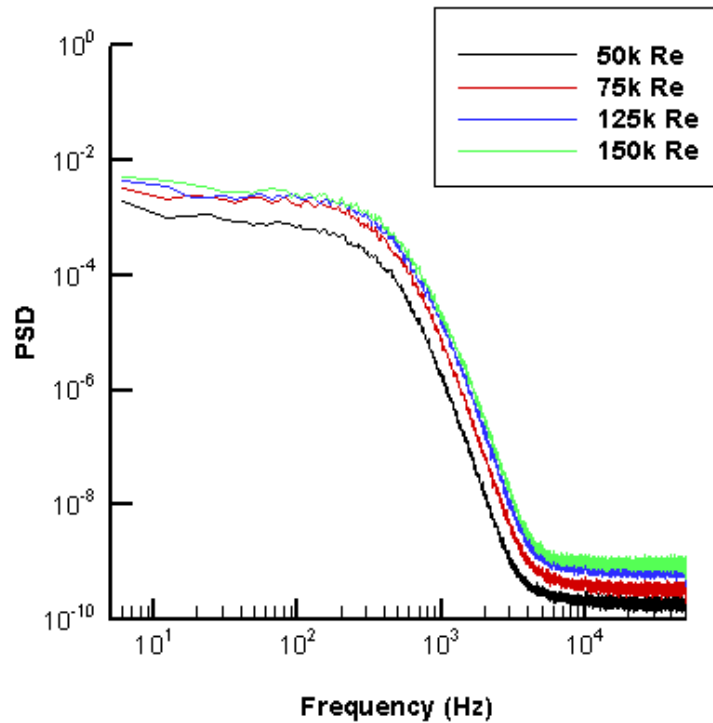
Figure 68: Power spectral density of inlet centerline turbulence

Measurements of the longitudinal velocity fluctuations at a fixed location usually only gives information of the time-scales of the turbulent eddies and not their spatial length scales. However, it is possible to estimate the length scales from these measurements. For example, Barret & Hollingsworth have provided a review of several methods for estimating the integral length scales based on the spectral information [79].

Figure 68 also reveals some turbulent characteristics of the inlet flow. The cut-off for the spectra occurs in the range of 3 kHz – 5 kHz; this cut-off frequency is closely related to the smallest scales of motion, of the Kolmogorov eddies. For example, this cut-off frequency suggests that a planar or volumetric particle image velocimetry setup with a temporal resolution

of around 10 kHz (twice the cut-off frequency because of the Nyquist sampling limit) and sufficient spatial resolution would be able to directly measure all of the turbulent motions, all to the smallest Kolmogorov eddies. High-powered fast repetition rate lasers along with high speed cameras would be needed to accomplish this feat. The Litron LDY 304 is a dual cavity unit with a repetition rate up to 20 kHz with an energy of ~3 mJ per pulse (or ~6 mJ per pulse at 10 kHz). While high speed cameras of up to 1 million frames per second have been developed, these cameras are limited by loss of image resolution at the highest frames rates. The FASTCAM SA-X2 available from Photron can capture 12-bit megapixel images at up to 13,500 frames per second. These cost of these systems however is currently prohibitive for users; if the capital costs of these equipment can be made affordable as well (as the cost of commercial software to operate these systems), then nearly exhaustive measurements of turbulent flows in practical systems may be readily performed in the near future.

Ribbed Channel

The friction factor for the one ribbed wall case (1RW) was constant for the Reynolds number range investigated, within uncertainty, and agrees with common trends that for high enough Reynolds number, the friction factor of ribbed channels is independent of Reynolds number. The corresponding friction augmentation therefore increases with increasing Reynolds number as depicted in Figure 69.
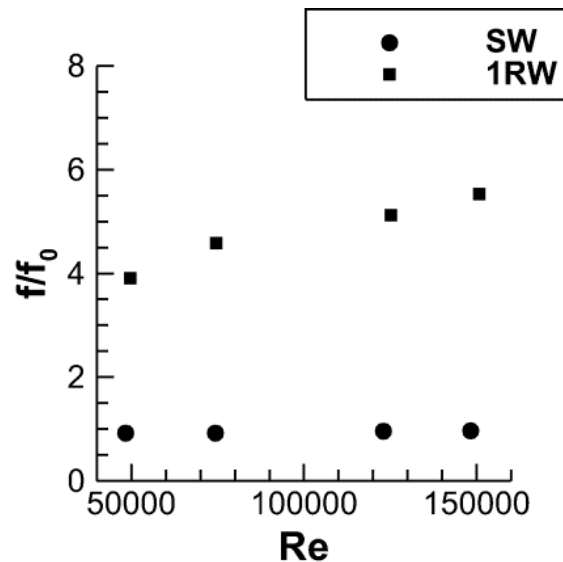
Figure 69: Friction augmentation results

Friction factor augmentation varied between 3.9 and 5.5 for the 1RW case. The friction augmentation of the SW case is also plotted in the same figure for comparison. The friction augmentation of a smooth channel should be close to 1 for a square duct, but some scatter from experimental errors should be expected. The square ducts, the baseline friction factor may not be entirely represented by the Blasius or PKN correlations, those correlations are valid only for a

circular pipe. A more representative of the true friction augmentation of the ribbed channels should use the friction factors obtained experimentally for the SW case as the normalizing factor. However, we chose to use the friction factor computed from correlations anyway since that is how results are typically represented in numerous publications. The natural friction factor in a square duct is actually less than that of a circular duct, in the range of 80-100% of the circular duct friction factor. The reason for the lower friction factor is because of the increased thickness of the laminar sublayer in the duct corners.

The local heat transfer augmentation for each of the walls is plotted in Figure 70 for the 150,000 Reynolds number testing condition. The local distribution of heat transfer for the other Reynolds numbers are similar to distributions obtained for 150,000 Re with some local differences in magnitude. The heat transfer augmentation for the ribs plotted in Figure 70 is based on the projected surface area, Ap. The projected heat transfer is obtained by multiplying the actual h of the ribs by the area factor (A_s/A_p=3). The local augmentation indicates that the streamwise development of the surface heat transfer is close to a periodically fully developed state, within measurement uncertainty.
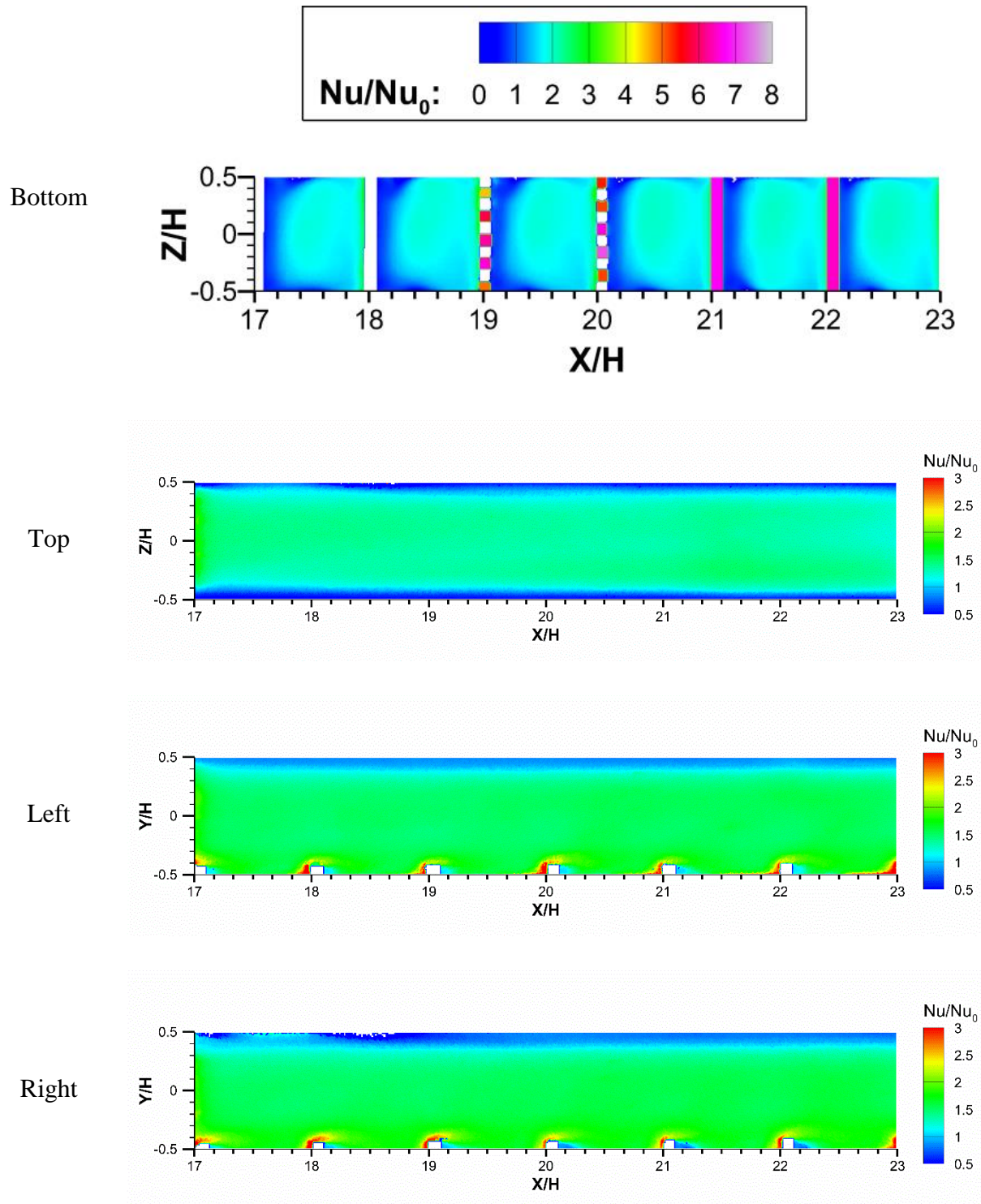
Figure 70: Local heat transfer augmentation at 150k Re

A region of high heat transfer augmentation on the non-ribbed portion of the bottom wall was found in-between two rib features, where phenomena associated with reattachment of the separated shear layer occur. This local maximum augmentation occurred at a relative distance of 5-6 rib heights downstream of the upstream edge of the rib. This trend is consistent with that reported in many studies including [12] which was performed on a similar configuration, albeit at lower Re and with ribs applied to two opposite walls.

The impact of the rib induced flow can be seen on the side walls (left and right walls). The highest heat transfer enhancement on the side walls occurs on the upstream leading edge of the rib, where the flow experiences a rapid contraction because of the obstruction of the flow caused by the rib. The heat transfer enhancement passes over the top of the rib and is angled upwards.

Locally Resolved Rib Heat Transfer

The application of the smaller aluminum cubes in the checkered arrangement provides increased spatial resolution over which the lumped capacitance model can be more accurately solved. Due to the use of Rohacell in-between aluminum cubes, there is no direct interaction from one aluminum segment to another, allowing the local heat transfer on the rib to be partially resolved spatially as well.

The variation of the heat transfer on the 10 smaller rib segments compared to their average is 15%, which can be considered significant. Although an experimental uncertainty of 10% obscures any analysis, based on physical conjectures, this variation is likely representative of the spanwise variation of the locally unresolved heat transfer on the rib surface. The heat

transport is stronger near the rib center where the flow impingement is stronger because of the greater flow velocity. In the presence of the side walls, the flow velocity is reduced which weakens the strength of the impingement. Hence the rib segments nearest the channel side walls have the lowest augmentation whereas the segments closer to the channel centerline generally have higher augmentation. The trend for the rib segments are also supported by the local heat transfer augmentation found on the smooth sections near the rib, which are also lowest near the side walls and highest near the channel centerline.

Segmented Rib versus Solid Rib

Since the contiguous aluminum ribs span the entire channel width, there is concern that multidimensional effects will dominate the transient response of the rib and that the lumped capacitance model may not be valid. For the full aluminum ribs, it was observed that the deviation in color-change time of all the pixels describing the response of the rib was approximately 1.0 s. For comparison, the uncertainty in the time at which the peak green intensity occurs for a typical non-ribbed pixel is 0.2–0.3 s. The lumped capacitance problem is less sensitive to the color-change time than a purely semi-infinite solid because of the large thermal mass of the rib feature. The 1 second deviation resulted in a deviation of the calculated local heat transfer coefficient for a particular rib of approximately 5%, which is less than the experimental uncertainty of the heat transfer coefficient for non-ribbed pixels despite the magnitude of the variation in color-change times being much greater than for a typical non-ribbed pixel.

Comparing the average heat transfer augmentation of the segmented ribs with the contiguous aluminum ribs, the differences in the average heat transfer augmentation are less than

12%, which is just beyond the experimental uncertainty. At least for the orthogonal ribs used in this study, the use of contiguous aluminum ribs provided results close to that of using smaller segmented rib-cubes, where the lateral conduction effects are restricted. This agreement is not expected to hold for ribs of arbitrarily greater lengths. The 90° rib arrangement is symmetrical with respect to the XY-plane, restricting the spanwise variation of the convection heat transfer coefficient distribution. For more complicated angled rib configurations where the rib arrangement is not symmetrical, a temperature gradient from end to end can occur.

Adiabatic versus Metallic Features

The spanwise average (average along Y or Z at a specific X) heat transfer augmentation of each wall is plotted in Figure 71. The results in the region 17H<X<19H are equivalent to results obtained using the standard technique whereas the results in the region 21H<X<23H are representative of measurement using a truly hybrid technique. This approach allows the two techniques to be compared directly.
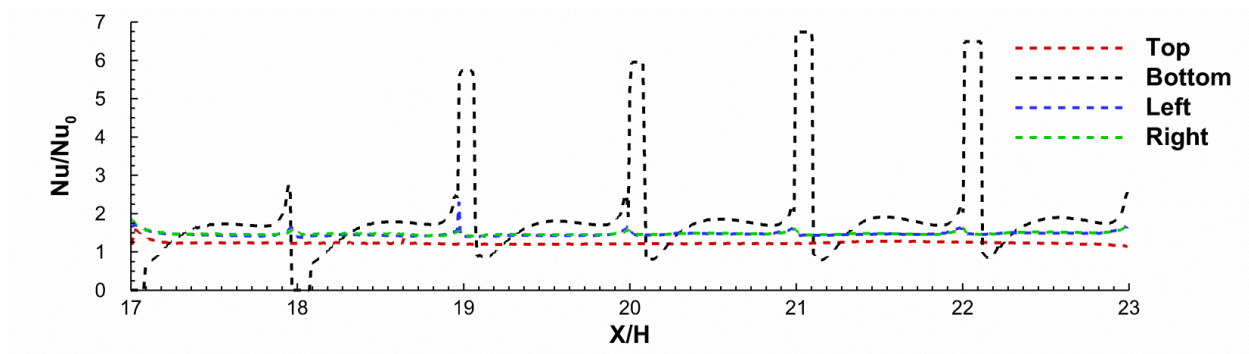
Figure 71: Spanwise averaged heat transfer augmentation at 150,000 Reynolds number

217

The spanwise averaged heat transfer augmentation on the smooth un-ribbed portions of the channel directly downstream of the Rohacell ribs (X/H = 17.1, 18.1) differs from the contiguous aluminum ribs (X/H = 21.1, 22.1) by up to 50% for pixels closest to the ribs and decreases quickly farther away from the rib. After 4-5 pixels, the differences attenuated to about 5%, on the order of the experimental uncertainty.

Taking the Fourier number equal to 1, the thermal penetration depth was calculated to be approximately 0.1H (5 to 6 pixels). Recall that in the numerical analysis, it was found that a Fourier number of 1 bounded most of the zones of error worse than 10%, whereas empirically only errors up to 5% were observed. This observation provides experimental verification that the thermal contamination effects are confined to the order of the penetration length, as it should for diffusion phenomena; it is also consistent with the results from the numerical analysis on the possible thermal contamination. However, the empirical results appear more optimistic than the numerical simulation, especially when considering that the mismatch in boundary conditions is more extreme experimentally than numerically. The mismatch refers to the Rohacell ribs (which can be considered adiabatic) being placed on the PMMA substrate and then comparing these results with the aluminum ribs placed on a PMMA substrate. The numerical simulation analyze the errors for only the latter case. The reason for the disagreement in magnitude of the errors encountered are probably related to the local distributions of the heat transfer coefficient on both the rib surfaces and the inter-rib surface.

With the current spatial resolution, the error introduced by miscalculating the heat transfer augmentation around metal features can affect the rib pitch average by no more than 2.5%. Even though the errors in the local heat transfer coefficient can be up to 50% the pixels

take up only a small area of the total surface being measured and have a smaller contribution to the surface average. If the 2.5% error is included in the uncertainty of the inter-rib heat transfer, the overall uncertainty is only marginally increased from 8% to 8.5%.

Similar thermal contamination effects were observed on the regions directly upstream of the rib features but the difference in heat transfer was less in magnitude and not as significant. The portion immediately behind the rib is more adversely affected because of the large differences in the apparent heat transfer at that location, between the very high heat transfer rib and the very low heat transfer in the recirculation region (which directly influences the color-change time of the liquid crystals). Additionally, even though the Rohacell ribs can be considered adiabatic, the one-dimensional semi-infinite assumption may also not be valid near these ribs because of the greater importance of multidimensional conduction effects. Under this context, the use of participating features may actually improve the validity of the 1D model close to the features.

A concern when a new technique is introduced is how comparable the results obtained with the new technique are with existing techniques. When benchmarking against results obtained from different experimental techniques, it is useful to know how the results of particular techniques compare to one another both qualitatively and quantitatively. The findings so far have demonstrated that both metallic and adiabatic features can be installed in transient heat transfer experiments without grossly affecting the overall quantitative results. Only the local results in the immediate vicinity of the ribs are affected. Far away from the features, either Rohacell or aluminum, the results are unaffected. In other words, results obtained using the hybrid technique can be compared directly (and locally) to results from the standard technique at a sufficient

distance from the features (which can be estimated by taking the Fourier number equal to 1). At distances closer than this critical length, numerical differences should be expected.

<p align="center">Regionally Averaged Heat Transfer</p>

The regionally averaged heat transfer augmentation is plotted for the 1RW case in Figure 72. The unfilled downward triangle represents the average of all the smooth inter-rib portions of the bottom wall only. The unfilled circles denote the average of only the metallic ribs (based on the actual area, A_s). The filled triangle symbols are oriented in the direction of the respective walls and represent the average of the individual wall. The surface average of the non-ribbed left, top, and right walls is unambiguous. The all wall average for the bottom wall is the area-weighted average of the ribs and the inter-rib heat transfer, where the total heat transfer of the ribs has been projected onto the planform area (the projected area, or area of just the base of the ribs).
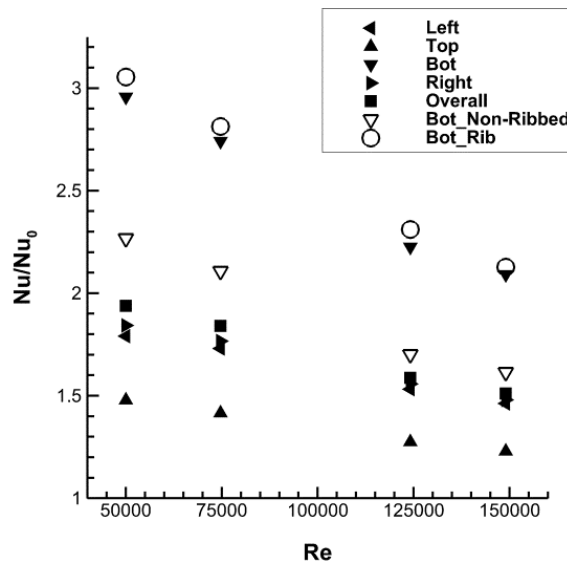
<p align="center">Figure 72: Regionally averaged heat transfer augmentation</p>

The highest overall heat transfer augmentation was 1.94 at 50,000 Re; the lowest overall augmentation was 1.51 at 150,000 Re. The heat transfer augmentation plotted for the ribs in Figure 72 is based on the actual convective surface area, A_s, to compare the rib versus non-ribbed heat transfer. The non-ribbed part of the ribbed wall has a lower heat transfer augmentation than the rib itself. When the heat transfer augmentation of the rib is multiplied by the area factor $(A_s/A_p = 3)$ to calculate the overall Nusselt number, the relative impact of the rib heat transfer on the overall heat transfer is even more significant. The overall Nusselt number is dominated largely by the performance of the ribs despite their small footprint.

The ribbed bottom wall produced higher wall-average heat transfer augmentation than the smooth top, left, and right walls, with a value of 2.96 for 50,000 Re and a value of 2.09 for 150,000 Re. The average of the non-ribbed section of the bottom wall also had a higher heat transfer augmentation than the other smooth walls but had a slightly lower augmentation than the ribs. The heat transfer augmentation of the non-ribbed section of the bottom wall was 2.27 for 50,000 Re and 1.61 for 150,000 Re. The left and right walls had 30-40% lower heat transfer augmentations than the bottom ribbed wall, while the top wall produced 40-50% lower heat transfer augmentations when compared to the bottom ribbed wall.

Overall Thermal Performance

The overall Nusselt number augmentation (average of all four walls) and friction factor augmentation are used to calculate the thermal performance, Eq. (29). The thermal performance of the smooth walled channel (SW) and ribbed channel (1RW) are plotted in Figure 73. The thermal performance decreases as Reynolds number increases because of the increase in friction factor augmentation coupled with the decrease in heat transfer augmentation. The thermal performance of the ribbed channel was greater than unity at the lower Reynolds numbers and less than unity at the higher Reynolds numbers. For ribbed channels with more than 1 ribbed wall, the thermal performance is typically much less than unity at high Reynolds numbers because of the significant friction augmentation encountered in those configurations.
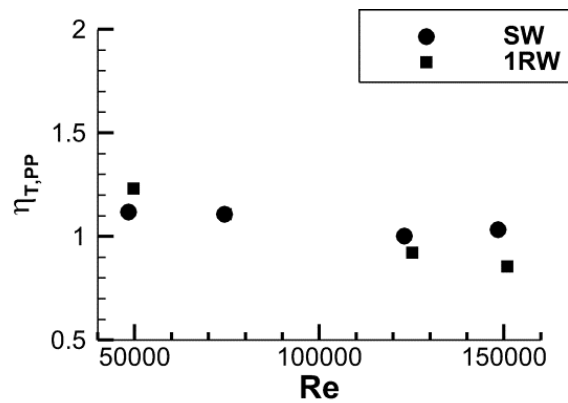
Figure 73: Thermal performance

Summary of Experimental Results

Heat transfer measurements were performed for a square channel with ribs on one wall in the Reynolds number range of 50,000 to 150,000 using the hybrid transient TLC technique. Adiabatic and aluminum ribs were used in tandem. Heat transfer results obtained using adiabatic and metallic rib features were compared quantitatively. It was demonstrated that the effects of thermal contamination were limited to a few percent of the overall heat transfer on the inter-rib section and only locations closest to the metallic features are affected. It was also demonstrated that, at least for the rib configurations in this study, the use of larger metallic ribs spanning the entire channel width did not invalidate the lumped capacitance model and the larger ribs were able to accurately represent the average heat transfer of the rib. Friction augmentation, overall heat transfer augmentation, and overall thermal performance of the one ribbed wall channel were also reported.

SINGLE-BAND MULTI-COLOR TECHNIQUE

This section introduces a novel single band, multicolor technique. The multi-color technique is an improvement of the traditional single color technique used in transient TLC experiments. The multi-color technique enables a redundant measurement of the surface temperature. Compared to traditional single-color techniques, the multi-color technique increases the yield of usable data. The multi-color technique can also be extended, perhaps in future work, into techniques using multiple TLC mixtures to form a multi-band multi-color technique. Data from the smooth channel validation experiment is used as a platform to demonstrate the multicolor technique and how this technique can be applied to typical transient heat transfer experiments.

An over-determined problem occurs when multiple surface temperature indicators are used to back-calculate the heat transfer coefficient, since there are more provided equations than unknown variables (the only unknown is *h*). An elementary approach is to solve the problem for the two indicators independently and then pool the result in an average. That is, solve Eq. (190) using the red temperature indicator and then solve Eq. (191) using the green temperature indicator and averaging.

$$\frac{T_r - T_i}{T_\infty - T_i} = 1 - exp\left(\frac{h^2 \alpha t}{k^2}\right) erfc\left(\frac{h\sqrt{\alpha t}}{k}\right) \qquad (190)$$

$$\frac{T_g - T_i}{T_\infty - T_i} = 1 - exp\left(\frac{h^2 \alpha t}{k^2}\right) erfc\left(\frac{h\sqrt{\alpha t}}{k}\right) \qquad (191)$$

A better approach is to solve the over-determined problem by least squares. The least

squares approach seeks the solution that minimizes the square sum of the residual, Eq. (192).

Because the residuals are minimized, the solution obtained using the least squares technique is

more optimal than solving the problems independently. The non-linear least squares algorithm

(*lsqnonlin*) in MATLAB is used to solve the over-constrained problem, replacing the *fsolve*

function used to solve the one-dimensional semi-infinite solid model.

$$min \sum_j \left[\frac{T_j - T_i}{T_\infty - T_i} - \left(1 - \left[exp\left(\frac{h^2 \alpha t_j}{k^2} \right) \right] \left[erfc\left(\frac{h\sqrt{\alpha t_j}}{k} \right) \right] \right) \right]^2 \qquad (192)$$

Table 18, contains the surface average Nusselt Number on each channel wall (Top,

Bottom, Left, and Right) using the single-color technique and the multi-color technique, and a

channel average Nusselt number using the aforementioned techniques along with the Dittus-

Boelter correlation and the Kays and Crawford correlation. These results are taken from the 50k

Re 1RW case in the previous section. The raw measurement data from the 50,000 Reynolds

number case was re-processed by solving the least squares problem for both the temperatures of

the red and green maximum signal intensities.

Overall, the results of the multi-color based post-processing technique predict 2% to 4%

higher heat transfer than the equivalent single color technique. The channel averaged (all walls)

Nusselt number of the experiment using the single-color technique are slightly lower than the

Nusselt number calculated from the Dittus-Boelter correlation, while the channel averaged

Nusselt number using the multi-color technique, of the exact same experiment, are slightly

higher than the Nusselt number calculated using the Dittus-Boelter correlation. The 2-4%

difference is within the 8% uncertainty in Nusselt Number for the single-color technique, and

can be considered marginal.

Table 18: Nusselt numbers obtained at 50k Reynolds number

	Top	Bottom	Left	Right	All Walls
Single-Color Red-Signal	60.63	66.02	64.22	62.3	63.29
Single-Color Green Signal	59.09	64.8	63.63	61.66	62.29
Multi-Color	61.28	65.6	64.92	62.84	63.66
Nu_{DB}					61.16
Nu_{KC}					53.79

In this implementation, the least squares solution is un-weighted between the wall

temperature indications obtained using the red and green signals. The optimal weighting

parameter that should be assigned to the solution of the red and green wall temperature is the

reciprocal of their uncertainties. However, given that the surface temperature indications occur at

similar temperatures (relative to the driving temperature difference) and that calibrated

uncertainties in the red and green peak intensities are nearly the same, the un-weighted approach

should be near optimal and a pooled variances for the combined uncertainties in the red and

green color signals may be used.

Uncertainty of Multi-Color Technique

In the previous section, the reprocessed results using the multi-color technique were mostly marginal. Given the marginal difference, the multi-color technique may not be worth pursuing. In this section, the propagation of error or sensitivity analysis method is used to compute the uncertainty is the heat transfer coefficient based on uncertainties in measured variables. The multi-color technique has the benefit of reduced uncertainty compared to the equivalent single-color technique, a more convincing argument for encouraging the use of the multi-color technique.

Temperature Uncertainty

Recall the normalized temperature defined according to Eq. (193):

$$\theta = \frac{T_w - T_i}{T_\infty - T_i} \tag{193}$$

The variance of the normalized temperature on the left hand side in terms of the variances of the right-hand side variables is given by Eq. (194).

$$\sigma_\theta^2 = \left(\frac{\partial \theta}{\partial T_w}\sigma_{T_w}\right)^2 + \left(\frac{\partial \theta}{\partial T_\infty}\sigma_{T_\infty}\right)^2 + \left(\frac{\partial \theta}{\partial T_i}\sigma_{T_i}\right)^2 \tag{194}$$

We arrive at Eq. (195) after evaluating the partial derivatives analytically.

$$\sigma_\theta^2 = \left(\frac{\sigma_{T_w}}{T_\infty - T_i}\right)^2 + \left(\theta \frac{\sigma_{T_\infty}}{T_\infty - T_i}\right)^2 + \left((\theta - 1)\frac{\sigma_{T_i}}{T_\infty - T_i}\right)^2 \tag{195}$$

By dividing both sides by the non-dimensional temperature, we have come up with an expression for the fractional or percentage uncertainties of each component using Eq. (196).

Knowing the uncertainties in the measured wall temperature, bulk temperature, and initial

temperature, the uncertainty in the non-dimensional temperature can be readily calculated.

$$\left(\frac{\sigma_\theta}{\theta}\right)^2 = \left(\frac{1}{\theta}\frac{\sigma_{T_w}}{T_\infty - T_i}\right)^2 + \left(\frac{\sigma_{T_\infty}}{T_\infty - T_i}\right)^2 + \left(\left(\frac{\theta - 1}{\theta}\right)\frac{\sigma_{T_i}}{T_\infty - T_i}\right)^2 \qquad (196)$$

Uncertainty of Least Squares

For the un-weighted least squares problem, we have Eq. (197), which relates the

variances in the observations to the variances in the fitted parameters. The two are related

through the Jacobian, Eq. (198). The inverse of the Jacobian terms in Eq. (197) are provided in

Eq. (199). We can thus re-write Eq. (197) as Eq. (200).

$$\sigma_\eta^2 = \sigma_\theta^2 (J^T J)^{-1} \qquad (197)$$

$$J = \begin{bmatrix} \dfrac{\partial \phi_1}{\partial \eta} \\ \dfrac{\partial \phi_2}{\partial \eta} \end{bmatrix} \qquad (198)$$

$$(J^T J)^{-1} = \frac{1}{\left(\dfrac{\partial \phi_1}{\partial \eta}\right)^2 + \left(\dfrac{\partial \phi_2}{\partial \eta}\right)^2} \qquad (199)$$

$$\sigma_\eta^2 = \frac{\sigma_\theta^2}{\left(\frac{\partial \phi_1}{\partial \eta}\right)^2 + \left(\frac{\partial \phi_2}{\partial \eta}\right)^2} \qquad (\ 200\ )$$

For the un-weighted least squares method, the variances of the observations are assumed equal. If the variances are not equal, then a weighted least squares method must be used. The weight factors are easily determined as the reciprocal of the variances of the observation. The un-weighted least squares method was chosen, rather than a weighted least squares method, because it was easier to implement in MATLAB. In future work, it would be useful to improve the multi-color technique using a weighted least squares approach. To use the un-weighted method where the variances in the red and green color signal are in general different, the variances must be pooled.

For demonstration purposes, suppose the two partial derives are equal in magnitude, which simplifies Eq. (200) to Eq. (201). This assumption is actually not very farfetched, since the temperature indicators are nearly the same temperature, the partial derivatives when computed at those temperatures will be nearly identical. Equation (201) more clearly shows the benefit of the multi-color technique. When additional temperature indicators are used, the variance or uncertainty in the solved parameter decreases with the square root of the number of indicators used, Eq. (202). Equations (201) & (202) closely resembles the variance of means in statistics.

$$\sigma_\eta^2 \approx \frac{\sigma_\theta^2}{n\left(\frac{\partial\phi}{\partial\eta}\right)^2} \qquad (201)$$

$$\sigma_\eta \propto \frac{\sigma_\theta}{\sqrt{n}} \qquad (202)$$

If the red and green color signals were solved independently and the results averaged, an equivalent uncertainty analysis would arrive at Eq. (202). This result does not mean that least-squares technique is equivalent to the method of separate solution. It was assumed that the temperature indicators were degenerate, the same temperature. This assumption was only to demonstrate how additional temperature indicators reduces the uncertainty. In general, the red and green color indicators do not occur at the same temperature, and the correct equation to evaluate the variance of the fitted parameter is Eq. (200).

Overall Uncertainty of Heat Transfer Coefficient

Recall that the argument of the complementary error function and the scaling exponential function can be expressed using the group variable, Eq. (203); the use of the group variable makes some of the arithmetic more neat without loss of generality. The solution to the one-dimensional semi-infinite solid model is given by Eq. (204). Equation (204) provides the relationship between the temperature observations and heat transfer coefficient which we like to solve. The sensitivity of the non-dimensional temperature to the grouped variable is given by Eq. (205). In the transient TLC technique, the inverse problem is solved rather than the forward problem. That is, temperature measurements are used to determine the heat transfer coefficient and not the other way around. Hence we need to compute the sensitivity of the heat transfer

230

coefficient to the temperature measurement. This partial derivative can be computed using the relation for derivatives of inverse functions, Eq. (206). Note that Eq. (204) is a monotonically increasing function and therefore one-to-one, which allows Eq. (206) to be used.

$$\eta = \frac{h\sqrt{\alpha t}}{k} \qquad (203)$$

$$\phi(\eta) = 1 - e^{\eta^2} erfc(\eta) \qquad (204)$$

$$\frac{\partial \phi}{\partial \eta} = \frac{2}{\sqrt{\pi}} - 2\eta e^{\eta^2} erfc(\eta) \qquad (205)$$

$$\frac{\partial \eta}{\partial \theta} \approx \frac{\partial \eta}{\partial \phi} = \frac{1}{\frac{\partial \phi}{\partial \eta}} \qquad (206)$$

The heat transfer coefficient can be expressed based on the group variable, material properties, and time at which the temperature indication takes place, Eq. (203).

$$h = \frac{\eta k}{\sqrt{\alpha t}} \qquad (207)$$

The uncertainty in the heat transfer coefficient based on these parameters is given by Equation (208). Equation (209) is the result once the partial derivatives have been evaluated analytically. Dividing both sides by the heat transfer coefficient (h) we then have an expression

231

for the fraction or percentage uncertainty of the heat transfer coefficient based on the fractional uncertainty in the other parameters, Eq. (210).

$$\sigma_h^2 = \left(\frac{\partial h}{\partial \eta}\sigma_\eta\right)^2 + \left(\frac{\partial h}{\partial t}\sigma_t\right)^2 + \left(\frac{\partial h}{\partial \alpha}\sigma_\alpha\right)^2 + \left(\frac{\partial h}{\partial k}\sigma_k\right)^2 \qquad (\ 208\ )$$

$$\sigma_h^2 = \left(\frac{k}{\sqrt{\alpha t}}\sigma_\eta\right)^2 + \left(\frac{\eta k t}{2(\alpha t)^{3/2}}\sigma_t\right)^2 + \left(\frac{\eta k \alpha}{2(\alpha t)^{3/2}}\sigma_\alpha\right)^2 + \left(\frac{\eta}{\sqrt{\alpha t}}\sigma_k\right)^2 \qquad (\ 209\ )$$

$$\frac{\sigma_h}{h} = \sqrt{\left(\frac{\sigma_\eta}{\eta}\right)^2 + \left(\frac{1}{2}\frac{\sigma_\alpha}{\alpha}\right)^2 + \left(\frac{\sigma_k}{k}\right)^2} \qquad (\ 210\ )$$

Equations (196), (200), and (210) are the ones needed to compute the uncertainties in the heat transfer coefficient for the multi-color technique. For the single-color technique, only Equations (196) and (210) are needed; Equation (200) is a redundant equation.

Representative uncertainties for the temperature measurements are given in Table 19. These uncertainties correspond to the accuracy of the thermocouples used for the bulk temperature and initial temperature measurements and the accuracy of the calibrated temperatures for the red and green peak intensities. The uncertainty in the normalized temperature is computed over the range of $0.3 < \theta < 0.7$ recommended by Yan & Owen [74] by evaluating Eq. (196).

Table 19: Uncertainty in temperature measurements

$\dfrac{\sigma_\theta}{\theta}$	$\dfrac{\sigma_{T_w}}{T_\infty - T_i}$	$\dfrac{\sigma_{T_\infty}}{T_\infty - T_i}$	$\dfrac{\sigma_{T_i}}{T_\infty - T_i}$
5-10%	0.3%	5%	5%

As summarized in Table 19, the uncertainty in the normalized temperature is currently dominated by the measurement of the driving temperature difference. The reason for that is because the uncertainties in the temperature measurements using thermocouples is less accurate than TLC. The accuracy of the TLC temperature is already quite high. The uncertainty of the normalized temperature can benefit from an improvement in the measurement of the bulk and initial temperatures.

Based on the range of uncertainties in the normalized temperature, Eq. (210) is used to evaluate the uncertainty in the calculated heat transfer coefficient for the single-color technique (n=1) and multi-color technique (n=2); the results are tabulated in Table 20.

Table 20: Uncertainty of multi-color technique

n	$\dfrac{\sigma_h}{h}$	$\dfrac{\sigma_\eta}{\eta}$	$\dfrac{\sigma_t}{t}$	$\dfrac{\sigma_\alpha}{\alpha}$	$\dfrac{\sigma_k}{k}$
1	5-10%	2-8%	1-3%	1.8%	0.5%
2	4-7%				

The uncertainty in the time at which the peak intensity takes place was determined from experience, from several hundred transient TLC experiments conducted by the author. With the appropriate filtering of the temporal R,G,B signals, the time at which the peak intensity in the red and green signals can be determined to within ±0.3 seconds (on equipment with a frame rate of 30 frames per second). For unfiltered signals the time of the event can be determined to ±0.3 seconds. The uncertainties of the material properties were taken from the calibration of PMMA.

The uncertainty of a typical single-color transient TLC experiment is thus 5-10%, which can be improved slightly using a multi-color experiment (4-7%) with small algorithmic changes. This analysis however, assumes the validity of the one-dimensional semi-infinite solid model. The semi-infinite body assumption is usually not violated in an experiment. However, the conduction into the semi-infinite body is not necessarily one-dimensional. Surface enhancement features such as dimple, rib, and wedge-shaped turbulators can induce highly non-uniform distributions of heat transfer coefficients. These non-uniform boundary conditions results in multi-dimensional conduction in the substrate material during the transient testing. Additional, the heat conduction in corners of the test duct where the side walls meet the top and bottom walls as well as corners made by the turbulators and substrate surface is also multidimensional. The additional error of should be accounted for when reporting the overall uncertainty, however the quantification of these effects has eluded researchers for some time. A few limited studies have been carried out to document their effects; Kingsley-Row et al. [80] have even proposed a technique to account for the lateral conduction error cause by non-uniform distributions of the heat transfer coefficient.

Summary of Multi-Color Technique

The multicolor technique utilizes two surface temperature indications from a single band thermochromic liquid crystals mixture to add redundancy to the surface temperature measurement. The multicolor technique can complement existing single color, multiband techniques without excessive complexity. Data previously collected using a single-color technique was easily reprocessed using the multi-color technique. Existing single-color algorithms can be updated with relative ease to use the multi-color approach. No changes to existing experimental procedure or equipment are needed. In future work the multicolor technique can be extended to multicolor, multiband techniques for very accurate measurements of surface heat transfer coefficients.

CONCLUSION

A numerical benchmark was performed using the computational fluid dynamics software package Fluent. The theoretical roughness functions were calculated from the bulk channel pressure drop and average surface heat transfer coefficient. These roughness functions were compared against a semi-empirical correlation. The numerical simulations were performed for a fixed geometry over the entire Reynolds number range of the correlation. Several turbulence modelling approaches were used. The various outcomes predicted by each turbulence model raises doubts over the predictive capabilities of the numerical simulations, especially in the absence of complementary experimental datasets.

The hybrid heat transfer technique, a full surface transient thermochromic liquid crystals based technique was presented. Details of the experimental setup are given, enabling the measurement of surface heat transfer coefficients on all participating surfaces. In the hybrid technique, local resolution is available in between the surface enhancements whereas only a regionally averaged heat transfer coefficient can be obtained on the metallic features.

An exact, closed form analytical solution to the enhanced lumped capacitance model was derived and implemented in the hybrid heat transfer technique. The spatiotemporal temperature development during a hybrid experiment was simulated numerically. Analysis on the results of the numerical simulation was used to characterize and quantify the errors in the modelling assumptions of the enhanced lumped capacitance model. Predictions of the enhanced lumped capacitance model are compared with the classical lumped capacitance model. The comparison

demonstrates that an inverse calculation of the heat transfer coefficient using the classical model will lead to erroneous results, beyond acceptable levels of experimental uncertainty.

Calibration experiments demonstrate that the red color signal may also be utilized as a surface temperature indicator, having similar characteristics as the green color signal. The traditional single color technique, which uses only the peak green intensity, is augmented to include the peak red intensity, resulting in a single-band, multi-color technique. The multi-color technique offers reduced experimental uncertainty without resorting to multiple bands or multiple experiments.

REFERENCES

[1]   B. Lakshminarayana, *Fluid Dynamics and Heat Transfer of Turbomachinery*. New York: John Wiley and Sons, 1996.

[2]   M. K. Chyu, "Recent Advances in Turbine Heat Transfer-With a View of Transition to Coal Gas Based Systems," in *14th International Heat Transfer Conference*, Washington D.C., 2010.

[3]   H. J. Gladden and R. J. Simoneau, "Review and Assessment of the Database and Numerical Modeling for Turbine Heat Transfer," in *Toward Improved Durability in Advanced Aircraft Engine Hot Sections*. vol. 2, I. D. E. Sokolowski, Ed., ed, 1989, pp. 39-55.

[4]   S. Eriksson, "The Swedish Development of Turbogenerators with directly water-cooled Rotors," in *2007 IEEE Conference on the History of Electric Power*, Newark, 2007, pp. 109-116.

[5]   A. Bejan, "General criterion for rating heat-exchanger performance," *International Journal of Heat and Mass Transfer,* vol. 21, pp. 655-658, 1978.

[6]   A. Bejan, *Advanced Engineering Thermodynamics*: John Wiley & Sons, 2006.

[7]   N. Kasagi, Y. Hasegawa, K. Fukagata, and K. Iwamoto, "Control of Turbulent Transport: Less Friction and More Heat Transfer," in *14th International Heat Transfer Conference*, Washington, D.C., 2010.

[8]   J.-C. Han, L. R. Glicksman, and W. M. Rohsenow, "An Investigation of Heat Transfer and Friction for Rib-Roughened Surfaces," *Int. J. Heat Mass Transfer,* vol. 21, pp. 1143-1156, 1978.

[9]   J. C. Han, J. S. Park, and C. K. Lei, "Heat Transfer Enhancement in Channels With Turbulence Promoters," *Journal of Engineering for Gas Turbines and Power,* vol. 107, pp. 628-635, 1985.

[10]   J.-C. Han, J. J. Huang, and C. P. Lee, "Augmented Heat Transfer in Square Channels with Wedge-Shaped and Delta-Shaped Turbulence Promoters," *Enhanced Heat Transfer,* vol. 1, pp. 37-52, 1993.

[11] P. R. Chandra, M. E. Niland, and J. C. Han, "Turbulent Flow Heat Transfer and Friction in a Rectangular Channel with Varying Numbers of Ribbed Walls," *Journal of Turbomachinery,* vol. 119, pp. 374-380, April 1997.

[12] M. E. Taslim, T. Li, and S. D. Spring, "Measurements of Heat Transfer Coefficients and Friction Factors in Passages Rib-Roughened on All Walls," *Journal of Turbomachinery,* vol. 120, pp. 564-570, 1998.

[13] L. Casarsa, M. Cakan, and T. Arts, "Characterization of the Velocity and Heat Transfer Fields in an Internal Cooling Channel with High Blockage Ratio," in *Turbo Expo 2002*, Amsterdam, 2002, pp. 1-8.

[14] G. I. Mahmood, P. M. Ligrani, and S. Y. Won, "Spatially-Resolved Heat Transfer and Flow Structure in a Rectangular Channel with 45° Angled Rib Turbulators," in *ASME Turbo Expo 2002*, Amsterdam, 2002.

[15] Z. Wang, P. T. Ireland, S. T. Kohler, and J. W. Chew, "Heat Transfer Measurements to a Gas Turbine Cooling Passage with Inclined Ribs," *Journal of Turbomachinery,* vol. 120, pp. 63-69, 1998.

[16] H. H. Cho, S. Y. Lee, and S. J. Wu, "The Combined Effect of Rib Arrangements and Discrete Ribs on Local Heat/Mass Transfer in a Square Duct," in *ASME 46th Annual International Gas Turbineand Aeorengine Congress and Exhibition*, New Orleans, LA, 2001, pp. 1-11.

[17] R. S. Bunker, T. G. Wetzel, and D. l. Rigby, "Heat Transfer in a Complex Trailing Edge Passage for a High Pressure Turbine Blade – Part 1: Experimental Measurements," in *ASME Turbo Expo 2002*, Amsterdam, 2002, pp. 1-7.

[18] Y. M. Zhang, W. Z. Gu, and J.-C. Han, "Heat Transfer and Friction in Rectangular Channels with Ribbed or Ribbed-grooved walls," *Journal of Heat Transfer,* vol. 116, pp. 58-65, 1994.

[19] E. M. Sparrow and N. Cur, "Turbulent Heat Transfer in a Symmetrically or Assymetrically Heated Flat Rectangular Duct with flow Separation at Inlet," *Journal of Heat Transfer,* vol. 104, pp. 82-89, 1982.

[20] Y.-H. Liu, L. M. Wright, W.-L. Fu, and J.-C. Han, "Rib Spacing Effect on Heat Transfer and Pressure Loss in a Rotating Two-Pass Rectangular Channel (AR=1:2) with 45-Degree Angled Ribs," in *ASME Turbo Expo*, Barcelona, 2006.

[21]   L. M. Wright and A. S. Gohardani, "Effect of Turbulator Width and Spacing on the Thermal Performance of Angled Ribs in a Rectangular Channel (AR=3:1)," in *ASME International Mechanical Engineering Congress and Exposition*, Boston, 2008.

[22]   S. Kunstmann, J. von Wolfersdorf, and U. Ruedel, "Heat Transfer and Pressure Loss in Rectangular One-Side-Ribbed Channels With Different Aspect Ratios," in *ASME Turbo Expo 2009*, Orlando, 2009.

[23]   R. L. Webb, "Performance evaluation criteria for use of enhanced heat transfer surfaces in heat exchanger design," *International Journal of Heat and Mass Transfer,* vol. 24, pp. 715-726, 4// 1981.

[24]   P. Li, J. E. Seem, and Y. Li, "A new explicit equation for accurate friction factor calculation of smooth pipes," *International Journal of Refrigeration,* vol. 34, pp. 1535-1541, 9// 2011.

[25]   William M. Kays, Michael E. Crawford, and B. Weigand, "Convective Heat and Mass Transfer," 4 ed New York, New York: McGraw-Hill, 2005.

[26]   J. Nikuradse, *Laws of flow in rough pipes*, 1933.

[27]   D. F. Dipprey and R. H. Sabersky, "Heat and momentum transfer in smooth and rough tubes at various prandtl numbers," *International Journal of Heat and Mass Transfer,* vol. 6, pp. 329-353, 5// 1963.

[28]   R. L. Webb, E. R. G. Eckert, and R. J. Goldstein, "Heat transfer and friction in tubes with repeated-rib roughness," *International Journal of Heat and Mass Transfer,* vol. 14, pp. 601-617, 4// 1971.

[29]   J. C. Han, "Heat Transfer and Friction in Channels With Two Opposite Rib-Roughened Walls," *Journal of Heat Transfer,* vol. 106, pp. 774-781, 1984.

[30]   P. R. Chandra, C. R. Alexander, and J. C. Han, "Heat Transfer and Friction Behaviors in Rectangular Channels with Varying numbers of Ribbed Walls," *International Journal of Heat and Mass Transfer,* vol. 46, pp. 481-495, 2003.

[31]   J. Carlson, A. Jaffe, and A. Wiles, *The Millenium Prize Problems*. Cambridge, Massachusetts, United States of America: Clay Mathematics Institute, 2000.

[32]   H. Tennekes and J. L. Lumley, *A First Course in Turbulence*. United States of America: The Massachusetts Institute of Technology, 1972.

[33]   T.-H. Shih, W. W. Liou, A. Shabbir, Z. Yang, and J. Zhu, "A New k - ε Eddy-Viscosity Model for High Reynolds Number Turbulent Flows – Model Development and Validation," *Computers Fluids,* vol. 24, pp. 227-238, 1995.

[34]   F. R. Menter, "Two-equation eddy-viscosity turbulence models for engineering applications," *AIAA Journal,* vol. 32, pp. 1598-1605, 1994/08/01 1994.

[35]   W. K. George, "Is there a universal log law for turbulent wall-bounded flows?," *Philosophical Transactions of the Royal Society A: Mathematical, Physical and Engineering Sciences,* vol. 365, pp. 789-806, March 15, 2007 2007.

[36]   M. Hultmark, "A theory for the streamwise turbulent fluctuations in high Reynolds number pipe flow," *Journal of Fluid Mechanics,* vol. 707, pp. 575-584, 2012.

[37]   M. Hultmark, M. Vallikivi, S. C. C. Bailey, and A. J. Smits, "Logarithmic scaling of turbulence in smooth- and rough-wall pipe flow," *Journal of Fluid Mechanics,* vol. 728, pp. 376-395, 2013.

[38]   S. M. Salim and S. C. Cheah, "Wall y+ Strategy for Dealing with Wall-bounded Turbulent Flows," in *International MultiConference of Engineers and Computer Scientists*, Hong Kong, 2009.

[39]   M. Wolfshtein, "The velocity and temperature distribution in one-dimensional flow with turbulence augmentation and pressure gradient," *International Journal of Heat and Mass Transfer,* vol. 12, pp. 301-318, 3// 1969.

[40]   S. V. Patankar, C. H. Liu, and E. M. Sparrow, "Fully Developed Flow and Heat Transfer in Ducts Having Streamwise-Periodic Variations of Cross-Sectional Area," *Journal of Heat Transfer,* vol. 99, pp. 180-186, 1977.

[41]   R. L. Webb, E. R. G. Eckert, and R. J. Goldstein, "Generalized heat transfer and friction correlations for tubes with repeated-rib roughness," *International Journal of Heat and Mass Transfer,* vol. 15, pp. 180-184, 1// 1972.

[42]   "Handbook of Thermochromic Liquid Crystal Technology," Glenview, Illinois, Handbook1991.

[43]   N. Abdullah, A. R. Abu Talib, A. A. Jaafar, M. A. Mohd Salleh, and W. T. Chong, "The basics and issues of Thermochromic Liquid Crystal Calibrations," *Experimental Thermal and Fluid Science,* vol. 34, pp. 1089-1121, 11// 2010.

241

[44]   V. U. Kakade, G. D. Lock, M. Wilson, J. M. Owen, and J. E. Mayhew, "Accurate heat transfer measurements using thermochromic liquid crystal. Part 1: Calibration and characteristics of crystals," *International Journal of Heat and Fluid Flow,* vol. 30, pp. 939-949, 10// 2009.

[45]   P. T. Ireland and T. V. Jones, "Liquid crystal measurements of heat transfer and surface shear stress," *Measurement Science and Technology,* vol. 11, p. 969, 2000.

[46]   A. Bejan, in *Heat Transfer*. vol. 6, ed New York: Wiley, 1993, pp. 148-156.

[47]   H. S. Carslaw and J. C. Jaeger, in *Conduction of Heat in Solids*, 2 ed Oxford, England, U. K.: Oxford University Press, 1959, pp. 70-73.

[48]   F. P. Incropera, D. P. Dewitt, T. L. Bergman, and A. S. Lavine, in *Fundamentals of Heat transfer*, 6 ed New York: Wiley, 2007, pp. 283-290.

[49]   M. K. Chyu, H. Ding, J. P. Downs, and F. O. Soechting, "Determination of local heat transfer coefficient based on bulk mean temperature using a transient liquid crystals technique," *Experimental Thermal and Fluid Science,* vol. 18, pp. 142-149, 10// 1998.

[50]   J. von Wolfersdorf, R. Hoecker, and C. Hirsch, "A Data Reduction Procedure for Transient Heat Transfer Measurements in Long Internal Cooling Channels," *Journal of Heat Transfer,* vol. 120, pp. 314-321, 1998.

[51]   S. C. Jenkins, I. V. Shevchuk, J. von Wolfersdorf, and B. Weigand, "Transient Thermal Field Measurements in a High Aspect Ratio Channel Related to Transient Thermochromic Liquid Crystal Experiments," *Journal of Turbomachinery,* vol. 134, pp. 031002-031002, 2011.

[52]   N. Domaschke, J. von Wolfersdorf, and K. Semmler, "Heat Transfer and Pressure Drop Measurements in a Rib Roughened Leading Edge Cooling Channel," *Journal of Turbomachinery,* vol. 134, pp. 061006-061006, 2012.

[53]   S. P. Chen, P. W. Li, M. K. Chyu, F. J. Cunha, and W. Abdel-Messeh, "Heat Transfer in an Airfoil Trailing Edge Configuration With Shaped Pedestals Mounted Internal Cooling Channel and Pressure Side Cutback," in *ASME Turbo Expo 2006: Power for Land, Sea, and Air*, Barcelona, Spain, 2006, pp. 819-828.

[54]   F. J. Cunha and M. K. Chyu, "Trailing-Edge Cooling for Gas Turbines," *Journal of Propulsion and Power,* vol. 22, pp. 286-300, 2006/03/01 2006.

[55]   M. Maurer, U. Ruedel, M. Gritsch, and J. v. Wolfersdorf, "Experimental Study of Advanced Covnective Cooling Techniques for Combustor Liners," in *ASME Turbo Expo 2008: Power for Land, Sea, and Air*, Berlin, Germany, 2008, pp. 1779-1789.

[56]   S. Kunstmann, J. v. Wolfersdorf, and U. Ruedel, "Heat Transfer and Pressure Loss in Rectangular One-Side-Ribbed Channels With Different Aspect Ratios," in *ASME Turbo Expo 2009: Power for Land, Sea, and Air*, Orlando, Florida, USA, 2009, pp. 251-261.

[57]   T. Lucky, V. Michelle, R. Mark, and J. Kapat, "Effect of Rib Aspect Ratio on Heat Transfer and Friction in Rectangular Channels," in *47th AIAA/ASME/SAE/ASEE Joint Propulsion Conference & Exhibit*, 2011.

[58]   Z. Wang, "The Application of Thermochromic Liquid Crystals to Detailed Turbine Blade Cooling Measurements," PhD PhD Dissertation, Engineering Science, University of Oxford, Oxford, England, U. K., 1991.

[59]   Z. Wang, P. T. Ireland, and T. V. Jones, "A technique for measuring convective heat transfer at rough surfaces," *Transactions of the Institute of Measurement and Control,* vol. 13, pp. 145-154, August 1, 1991 1991.

[60]   C. Son, G. M. Dailey, P. Ireland, and D. Gillespie, "An Investigation of the Application of Roughness Elements to Enhance Heat Transfer in an Impingement Cooling System," in *ASME Turbo Expo 2005: Power for Land, Sea, and Air*, Reno, Nevada, USA, 2005, pp. 465-479.

[61]   C. Son, D. Gillespie, P. T. Ireland, and G. M. Dailey, "Heat Transfer Enhancement Strategy for an Impingement Cooling System," in *Eighth International Symposium on Transport Phenomena and Dynamics of Rotating Machinery*, Honolulu, Hawaii, 2000, pp. 722-730.

[62]   L. V. Tran, J. S. Kapat, A. L. Pham, D. L. Zachary, and P. K. Tran, "Heat Transfer Measurements Using the Hybrid Heat Transfer Technique With Thermally Adiabatic and Participating Ribs," in *ASME Turbo Expo 2013: Turbine Technical Conference and Exposition*, San Antonio, Texas, 2013, p. V03AT12A035.

[63]   G. Wagner, M. Kotulla, P. Ott, B. Weigand, and J. von Wolfersdorf, "The Transient Liquid Crystal Technique: Influence of Surface Curvature and Finite Wall Thickness," *Journal of Turbomachinery,* vol. 127, pp. 175-182, 2005.

[64]   J. Fourier, *The Analytical Theory of Heat*: Cosimo Classics.

[65]   S. Kunstmann, "A Contribution to Gas Turbine Combustor Cooling Using Complex Configurations," Doctor of Engineering Sciences Dissertation, Aerospace Engineering and Geodesy Department, University of Stuttgart, Stuttgart, Germany, 2012.

[66]   J. Weideman, "Computation of the Complex Error Function," *SIAM Journal on Numerical Analysis,* vol. 31, pp. 1497-1518, 1994.

[67]   M. Leutenegger, "Error function of complex numbers," ed, 2008.

[68]   J. K. Ostanek, J. Prausa, A. Van Suetendael, and K. A. Thole, "Establishing a Methodology for Resolving Convective Heat Transfer From Complex Geometries," *Journal of Turbomachinery,* vol. 132, pp. 031014-031014, 2010.

[69]   F. Hoefler, S. Schueren, J. von Wolfersdorf, and S. Naik, "Heat Transfer Characteristics of an Oblique Jet Impingement Configuration in a Passage With Ribbed Surfaces," *Journal of Turbomachinery,* vol. 134, pp. 031022-031022, 2011.

[70]   L. V. Tran and J. S. Kapat, "Coupled Zero-Dimensional/One-Dimensional Model for Hybrid Heat Transfer Measurements," *Journal of Thermophysics and Heat Transfer,* vol. 28, pp. 236-250, 2014/04/01 2014.

[71]   P. J. Roache, in *Fundamentals of Computational Fluid Dynamics*, ed Albuqueque, NM: Hermosa Publishers, 1998, pp. 459-499.

[72]   L. Tran, M. Valentino, M. Ricklick, and J. S. Kapat, "Effect of Rib Aspect Ratio on Heat Transfer and Friction in Rectangular Channels," in *Joint Propulsion Conference*, San Diego, 2011.

[73]   L. V. Tran, "Effect of Rib Aspect Ratio on Heat Transfer and Friction in Rectangular Channels," Mechanical Engineering HIM Thesis, Mechanical, Materials, and Aerospace Engineering, University of Central Florida, Orlando, Florida, 2011.

[74]   Y. Yan and J. M. Owen, "Uncertainties in transient heat transfer measurements with liquid crystal," *International Journal of Heat and Fluid Flow,* vol. 23, pp. 29-35, 2// 2002.

[75]   M. I. Valentino, "Heat Transfer and Friction Augmentation in a Narrow Rectangular Duct with Symmetrical and Non-Symmetrical Wedge Shaped Turbulators," Master of Science M.S. Thesis, Mechanical, Materials, and Aerospace Engineering, University of Central Florida, Orlando, Florida, 2011.

[76] S. J. Kline and F. A. McClintock, "Describing Uncertainties in Single-Sample Experiments," *Mechanical Engineering,* vol. 75, pp. 3-8, 1953.

[77] R. J. Moffat, "Describing the Uncertainties in Experimental Results," *Experimental Thermal and Fluid Science,* vol. 1, pp. 3-17, 1988.

[78] *PTC 19.1 - 2005*. New York: ASME, 2005.

[79] M. J. Barrett and D. K. Hollingsworth, "On the Calculation of Length Scales for Turbulent Heat Transfer Correlation," *Journal of Heat Transfer,* vol. 123, pp. 878-883, 2000.

[80] J. R. Kingsley-Rowe, G. D. Lock, and J. Michael Owen, "Transient heat transfer measurements using thermochromic liquid crystal: lateral-conduction error," *International Journal of Heat and Fluid Flow,* vol. 26, pp. 256-263, 4// 2005.